Investigating the optical properties of gold decorated CdS nanoparticles *via* physical techniques.

By

Sibusiso Nqayi

(B.Sc. Hons.)

The dissertation is submitted in partial fulfilment of the requirements for the degree

MAGISTER SCIENTIAE

In the

Faculty of Natural and Agricultural Sciences

Department of Physics

At the

University of the Free State

Bloemfontein, Republic of South Africa

Promoter: Dr R.A. Harris

Co-Promoter: Prof. H.C. Swart

Co-Promoter: Dr. P.M. Shumbula

April 2019

Declaration

I, Sibusiso Nqayi (2012040552) solemnly confirm that the content of this work is mine and that it has not been previously submitted in any type of degree or qualification of any kind in this or any other university.

Initials…………………. at…………………………………………….

On the ………………… of ……………………………………2019

“When you are inspired by some great purpose, some extraordinary project, all of your thoughts break their bonds: your mind transcends limitations, your consciousness expands in every direction and you find yourself in a new great and wonderful world. Dormant forces, faculties and talents become alive and you discover yourself to be a great person than you ever dreamed yourself to be.”

-Patanjali-

“Sure I am that this day we are masters of our fate, that the task which has been set before us is not above our strength; that pangs and toils are not beyond my endurance. As long as we have faith on our own cause and unconquerable will to win, victory will not be denied to us.”

-Winston Churchill-

Dedication

This dissertation is dedicated to late my grandmother, parents (Nosinothi and Amos Nqayi) and sisters who have been there for me throughout the hardships.

Acknowledgments

I would like to express my appreciation to the following individuals whom have contributed dearly to this journey.

- Firstly, I am very grateful to God for the wisdom, will and ability to carry out this work and get through the challenges that I overcame in the way.
- Thanks to **Dr. Richard Harris** (promoter) for making the study possible while guiding and assisting me throughout the study, it would have not been possible without him.
- I'm grateful to **Prof. Hendrik Swart** (co-promoter) for overseeing this work and for the great input he gave throughout the study.
- I sincerely thank **Dr. Simon Ogugua** for always taking time out to assist me with my work whenever requested.
- **Prof RE Kroon** played an important role with his help and advice with photoluminescence studies
- **Mr. E. Lee** for assistance with FE-SEM measurements, **Dr. M. Duvenhage** for assisting with TOF-SIMS measurements, **Prof. Roos** and **Prof. E. Coetsee-Hugo** for assisting with XPS measurements.
- I'm gratefull to **Mr. Lucas Erasmus** for assistance with PLD deposition and again to Mr. Edward Lee with sputter coating.
- **Ms. Zamaswazi Tshabalala, Ms. Katekani Shingange,** and **Mr. Nadir Saeed** for their great advice.
- Thanks to all the Physics department staff members and fellow students for their invaluable contributions.
- Thanks to the Department of Science and Technology (DST) who have sponsored this work under the MSc Nanoscience Postgraduate programme.

Abstract

Quantum dots are very important in modern technology, which is driven by decreasing machinery size, while enhancing performance. Quantum dots form an integral part of nanoparticles (NPs) with a particle size that varies between 2-10 nm. The preparation of these materials is very important, with structural, optical and morphological studies showing dependence on synthesis conditions. In this work, cadmium sulphide (CdS) NPs were prepared using the chemical precipitation method. To control the particle size, thioglycerol (TG) was used as a capping agent with particle size dependent on the TG concentration. Scanning electron microscope and transmission electron microscope investigations showed that agglomerated particles were formed due to the high surface energies that are associated with very small particles. In order to study the role of the reaction conditions on the stabilizing of the particle surface, the particles were prepared using two different solvents: water and ethanol. X-ray diffraction (XRD) data showed that the use of water solvent resulted in particles consisting of a mixed phases of wurtzite and cubic structures. The quantum confinement effect was first observed in the colour change of the prepared samples. In the absence of TG, the sample had an orange colour, however, by introducing 0.1 mL of TG, the colour of the particles turned yellow while at 0.8 mL of TG the particles had a whitish-lemon colour. This effect was confirmed by the blue shift to lower wavelengths of the absorbance spectra obtained with the ultraviolet-visible (UV-Vis) technique. The blue shift is associated with a decreasing particle size. The increased sulphur content with an increasing TG concentration also increased the photoluminescence (PL) recombination rate. Thus preparation of CdS NPs with the water solvent resulted in luminescence from green, yellow, and red emission. The annealing of the 0.3 mL sample resulted in sintering of the small particles making up bulk particles with a hexagonal structure upon a phase transformation temperature. This change in phase introduced infrared emission in the PL spectra. This emission was obtained in the as-prepared samples in the ethanol solvent. Its source was unreacted cadmium chloride ($CdCl_2$) species. Ethanol solvent could not completely dissolve the starting material in the reaction. This resulted in the appearance of strong $Cd(OH)_2$ peaks in the XRD pattern. Also, the XRD pattern showed a cubic zinc blende structure to be dominant in the formed particles with a size of 6.3 nm, 3.0 nm, 3.0 nm, 2.9 nm, and 2.6 nm for S0 (no TG), S1 (0.1 mL TG), S2 (0.2 mL TG), S3 (0.3 mL TG), and S5 (0.8 mL TG), respectively. These were all in the domain of quantum dots and the introduction of TG in this batch took the NP size to sizes below the exciton Bohr radius of CdS. Thereafter the deposition of gold (Au) co-catalyst on the CdS surface was done using physical methods in the top-down approach. It was observed that Au nanoclusters deposited with pulsed laser deposition (PLD) and sputter coating (SPC) enhanced the absorbance of CdS in the UV-Vis spectra. Nanocomposites prepared with the SPC technique showed the highest absorbance enhancement due to the larger cluster formation which was observed with time-of-flight secondary ion mass spectroscopy as agglomerated clusters. PL spectra showed a decreased luminescence, which showed a decrease in the electron-hole recombination. This is of high importance in the field of photocatalysis for water splitting. This occurred due to the transfer of electrons from the highest occupied states in the CdS semiconductor to the lowest unoccupied states in the Au metal.

Keywords

Nanoparticles, quantum confinement effect, cadmium sulphide, Schottky junction, pulsed laser deposition, sputter coating, gold nanoclusters.

List of Acronyms

EDS:	Energy Dispersive X-ray Spectroscopy
FE-SEM:	Field Emission Scanning Electron Microscopy
FTIR:	Fourier Transform Infrared Spectroscopy
FWHM:	Full Width Half Maximum
NP:	Nanoparticle
NC:	Nanocomposite
UV-Vis:	Ultraviolet-Visible Spectroscopy
TEM:	Transmission Electron Microscope
ToF-SIMS:	Time-of-Flight Secondary Ion Mass Spectroscopy
PL:	Photoluminescence
PLD:	Pulsed Laser Deposition
SPC:	Sputter Coating
XRD:	X-ray Diffraction
XPS:	X-ray Photoemission Spectroscopy

List of Chemical elements and compounds

Cd: Cadmium

S: Sulphur

Cl: Chloride

Na: Sodium

$CdCl_2$: Cadmium chloride

Na_2S: Sodium sulphide

$C_3H_8O_2S$: Thioglycerol (TG)

Table of Contents

CHAPTER 1: Introduction

CHAPTER 2: Literature review

CHAPTER 3: Synthesis of nanomaterials

CHAPTER 4: Characterization techniques

CHAPTER 5: Quantum confinement effect structural and optical properties of CdS nanoparticles prepared with water solvent.

CHAPTER 6: Effect of ethanol solvent on structural and optical properties of cadmium sulfide preparation.

CHAPTER 7: Optical sensitivity of CdS-Au nanocomposites prepared by physical techniques.

CHAPTER 8: Summary, conclusion, and future work.

List of Figures

List of Tables

CHAPTER 1

Introduction

1.1.Overview

CdS particles are attractive photocatalytic materials for solar energy conversion to chemical energy under visible-light irradiation [1]. The band gap of the semiconductor increases with decreasing particle size and so does the crystallinity of the material. This decrease in particle size also increases the surface area to volume ratio making it easier for electrons and holes to reach the surface and reduce the number of electron-hole recombinations, which is an important contributing factor in photocatalytic water splitting. The preparation methods of this material however, play a crucial role in the crystal structure and size is also dependent on the reaction conditions [2]. Increased surface area to volume ratio plays an important role in enhancing the quantum yield of the nanoparticles (NPs). The highest quantum efficiency (93%) to be reported so far has been for CdS semiconductor with a Pt-PdS dual co-catalyst in the presence of sacrificial reagents by Yan *et al*. [3]. Many semiconductor materials are ineffective in giving high evolution rates during the splitting; even in the presence of appropriate sacrificial reagents. This is usually so for two reasons: the quick recombination of the electron/hole before reaching the surface and the surface reaction being too slow to efficiently consume the charges. The most conventional modification of a photo-catalyst to improve water reduction is by loading a co-catalyst. Co-catalysts can provide reduction and oxidation active sites, catalyse the surface reactions by lowering the activation energies, trap the charge carriers, and suppress the recombination of photogenerated charges. However, the optical and electrical properties of the semiconductor/metal heterostructure can be affected by the shape and size of the metal co-catalyst. Employing physical methods during the deposition of the metal on the semiconductor surface enable better control of the size and shape of the metal.

1.2. Problem Statement

The demand for energy has increased dramatically since the beginning of the industrial revolution and so have the global environmental consequences which have (in recent years) led to the pursuit of clean and renewable energy that can be generated in huge quantities with negligible or no negative environmental impact. Over the past three decades, energy consumption has doubled with over 77% of the energy coming from traditional energy generation methods that employ fossil fuels [4]. There has been a slow rise in the use of renewable, clean energy over the past decade but due to low efficiencies, especially in photovoltaic solar cells, this increase has also been met by a drastic increase in the carbon footprint of the world population [5]. Photocatalysis has a variety of applications since the first report on the photocatalytic splitting of water on TiO_2 electrodes was published in 1972 by Honda and Fujishima [1]. However, the research has focused on the splitting of water using ultraviolet irradiation which only makes up 4% of the incoming solar energy. Thus, recently the focus has turned to the abundant visible light which makes up 43 % of incoming solar energy [3]. Hydrogen obtained using this method is the most environmentally-friendly source of energy. The challenge in the conversion of solar energy into chemical energy is the quantum efficiency (QE) of the photocatalysts. This can be improved by increasing the number of carriers collected by the catalyst relative to the number of photons of a given energy incident on the catalyst. In the primary course of natural photosynthesis, the overall QE can be as high as 95% [5][1]. In this study, gold (Au) is used as a co-catalyst to coat cadmium sulfide (CdS) NPs using physical techniques. The Au clusters on the CdS surface drastically reduce recombination by keeping the electron-hole pair separated.

1.3. Research Aims

In an attempt to address the issue of low quantum efficiency in photocatalysts, this work looks at:

- Synthesis of CdS NPs with various particle size using TG as a capping agent.
- Studying the effect of solvent (water and ethanol) during CdS NP synthesis.
- The effect of depositing Au nanoclusters on the CdS surface using two physical techniques (as opposed to the conventional chemical techniques) such as pulsed laser deposition (PLD) and sputter coating (SPC) on the observed optical properties of Au decorated CdS NPs.

1.4.Thesis Layout

This dissertation is organized in the following manner:

Chapter 1 - Introduction: it consists of the dissertation overview, problem statement, objectives, and the thesis layout.

Chapter 2 - Literature review: A general background on nanomaterials is presented and specifically the quantum confinement effect and how it relates to electron-hole splitting and recombination. The effect of increased surface area, photoluminescence, and the creation of Schottky contact between CdS and gold nanoclusters are discussed.

Chapter 3 - Synthesis of nanomaterials: fabrication approaches for the synthesis of nanomaterials are divided into two groups, the bottom-up and top-down approaches. The synthesis of CdS NP with the chemical precipitation method is discussed together with the deposition of gold clusters on the NP surfaces with physical techniques as opposed to the conventional chemical methods.

Chapter 4 - Experimental techniques: The basic physical principals involved in the workings of the experimental tools used to study the synthesized materials are discussed in detail in the chapter.

Chapter 5 – Properties of CdS NPs prepared with water solvent: In this chapter, a detailed report on the structural and optical properties of CdS NPs synthesized with water as a solvent, is given.

Chapter 6 – The preparation of CdS NP in ethanol solvent: The effect of changing the solvent from water to ethanol on structural, morphological and optical properties of CdS NPs are studied in this chapter.

Chapter 7 – Synergy of Au coated/decorated CdS NPs: In this chapter, the effects of using physical methods for Au coating of CdS NPs on optical properties are studied.

Chapter 8 – Summary, conclusion, and future work: In this last chapter, accompanying the summary is a conclusion of the work and a way forward with the study is proposed.

Reference

[1] Q. Li, B. Guo, J. Yu, J. Ran, B. Zhang, H. Yan, and J. R. Gong, “Highly efficient visible-light-driven photocatalytic hydrogen production of CdS-cluster-decorated graphene nanosheets,” *J. Am. Chem. Soc.*, vol. 133, no. 28, pp. 10878–10884, 2011.

[2] V. Singh, P. K. Sharma, and P. Chauhan, “Synthesis of CdS nanoparticles with enhanced optical properties,” *Mater. Charact.*, vol. 62, no. 1, pp. 43–52, 2011.

[3] H. Yan , J. Yang, G. Ma, G. Wua, X. Zong, Z. Lei , J. Shi , C. Li, “Visible-light-driven hydrogen production with extremely high quantum efficiency on Pt-PdS/CdS photocatalyst,” *J. Catal.*, vol. 266, no. 2, pp. 165–168, 2009.

[4] G. P. Beretta, “world energy consumption and resources: an outlook for the rest of the century”, Meccania, Brescia, Italy, 2014.

[5] British Petroleum, “BP Statistical Review of World Energy 2017,” London, UK, 2017.

CHAPTER 2

Background study of CdS NPs with Au cocatalyst.

2.1 Introduction

This is an introductory chapter to nanoscience, nanomaterials, the quantum confinement effect and their application to nanotechnology with a specific focus on CdS NPs. The history of this type of interdisciplinary science together with its importance going to the future is discussed.

2.2. Nanoscience: a brief history.

The word "nano" means very small with a Greek origin translated from the word "dwarf". In terms of units of measure, it represents "one billionth" (10^{-9}). A nanometre (nm) is, therefore, one-billionth of a meter. Figure 2.1 shows the nano-scale relative to material that can be observed with an unaided human eye. A sheet of paper, for instance, is 100 000 nm thick and a human strand of hair is about 80 000 nm in diameter.

Nanoscience has been defined by The Royal Society and The Royal Academy of Engineering as "the study of phenomena and manipulation of materials at atomic, molecular and macromolecular scales, where properties differ significantly from those at a larger scale" [1]. This is an interdisciplinary field of science that involves disciplines that vary from chemistry, physics, and biology, to medicine, engineering, and electronics. To help distinguish developments between the different disciplines, nanoscience has been divided into four diverse categories: nanomaterials, nanometrology, optoelectronics (information and communication technology, electronics), and bio-nanotechnology (and nanomedicine). This helps prevent conceivable overlap in this extensive field of science.

In this work, the category of nanomaterials is studied. One of the reasons for studying nanomaterials is to investigate the effect that a reduction of material size to the nanoscale, known as quantum confinement effect, may have on the material characteristics and properties. The confinement of electrons results in changes in material properties, such as electrical conductivity, luminescent colour, mechanical strength, and even weight change, as reported before. A metal can become a semiconductor or an insulator at the nanoscale level [1]. For instance, bulk silver is non-hazardous, whereas silver NPs can kill viruses upon contact. Another exceptional property of nanomaterials is that they can be fabricated atom-by-atom using a method known as bottom-up which is discussed in detail in chapter 3. Finally, nanomaterials have a large surface area-to-volume ratio relative to bulk materials. This is a critical parameter that is useful in the fields of catalysis and sensor development.

2.2.1 Nanomaterials

The interdisciplinary field of nanomaterials combines expertise from both nanosciences as well as nanotechnology to develop materials that exhibit dimensional characteristics on the nanoscale [2]. The nanoscale is conservatively defined (in terms of the dimensions of a system) as 1 to 100 nm. Thus, materials that have particle sizes in this size-range are typically classified as nanomaterials. The size range generally has a minimum set at 1 nm to evade single atoms or very small groups of atoms being labeled as nano-objects. The upper limit is conventionally classified as 100 nm, but this has often been said to be a ‘fluid’ limit: regularly objects with superior dimensions (even 200 nm) are defined as nanomaterials. One might ask ‘why 100 nm and not 150 nm or even 1 000 nm?’ This is because the range itself focuses on the effect that dimensions have on a specific material (for example, the manifestation of the quantum phenomenon) rather than at what exact dimension this effect arises.

Nanoscience is not just the science of the small, but the science in which materials with small dimension illustrate new physical phenomena collectively called quantum effects, which are size-dependent and dramatically different from the properties of macroscale materials [3]. To further understand the size ‘nano’, Figure 2.1 shows a scale bar ranging from centimetre objects like a tennis ball down to a water molecule. Nano sized objects are smaller than bacteria or cells, however, it is larger than a single atom.

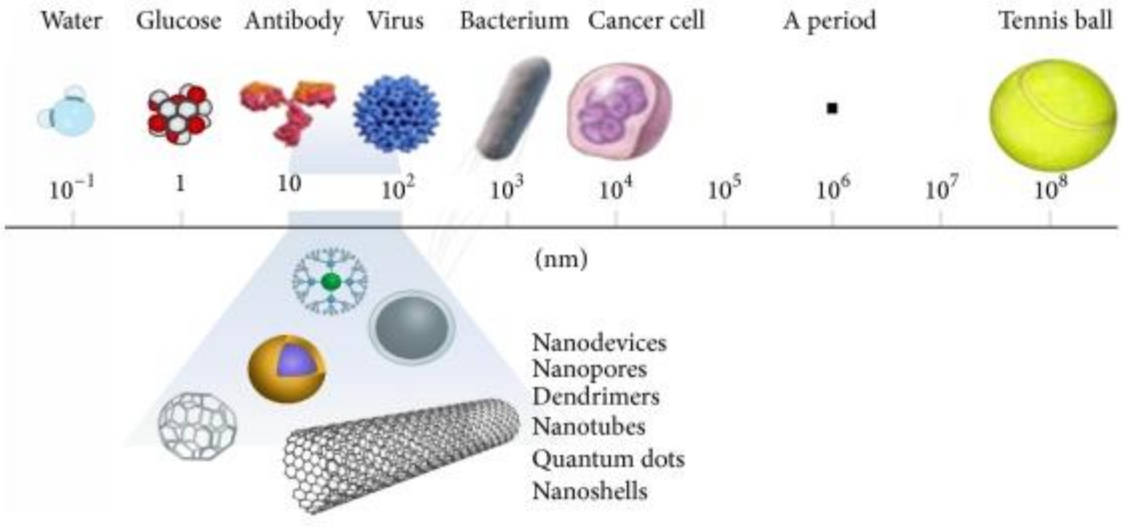

Figure 2.1. Comparison from macro scale to atoms with the intermediate, scale for nanomaterials (1-100 nm) [4]**.**

Nanomaterials can be divided into two categories: Naturally occurring nanomaterials (nanoscience in nature) and the man-made nanomaterials.

2.2.1.1 Naturally occurring nanomaterials

Since Richard Feynman's famous lecture in 1959 titled "There is plenty of room at the bottom" [5], there has been a significant escalation of interest amongst scientists and researchers in nanoscience. However, nanomaterials have been around for millions of years with nature being the ultimate manufacturer of nanomaterials. This recent attention is due to advancements in characterization/synthesis tools and techniques permitting manipulation and control of nanoscale materials. Some of the oldest known nanomaterials include: Halloysite, carbon nanotubes, carbon fullerene, and gecko.

Halloysite is an aluminosilicate clay that forms as volcanic feldspars weather, from a procedure that involves the intercalation of water through the native bed dissolving the sulfur in the volcanic mass formed for a highly acidic environment. The acids dissolve a large part of the mineral content of the native feldspar, eventually leaching out nearly everything except the silica and alumina content [6]. The process also unleashes a greater degree of free space within the initial bed allowing the ore to get closer to becoming a pure aluminosilicate. The clay starts to assemble into a laminar structure of alumina-silica bi-layers seized together by an intercalated water layer. The silica layer is tetrahedrally bound, whereas the alumina layer is octahedrally bound, producing a lattice disparity and subsequent curling force that, given enough room to move, will curl the laminar platelet structure into a tube, much like rolling up a burrito or a newspaper.

The first carbon nanotube together with the first buckyball (carbon fullerene) was created by nature as the end product of a combustion process made of various fossil fuels. Diesel-fuelled cars also produce carbon nanotubes as a side-effect in the form of the scum that forms on the inside of the tailpipe which contains a number of different carbon nanotubes.

Some animals also make use of nanotechnology when they cling against objects (against gravity) on vertical surfaces. Nanoscience allows this to happen, with nano attachments increasing the adhesion forces. The heaviest animal with this ability to climb walls is a gecko, which is the reason scientist have high interest in studying the science behind its abilities.

Solely on a gecko's toes, there is said to be one billion tiny adhesive hairs, about 200 nanometres in both width and length [7]. A gecko makes use of the nano hair to cling to surfaces by employing Van-der-Waals forces between the nano hair and the atoms on the surface to which it clings. This temporary hold can occur between atoms at the molecular scale [8].

Another factor to consider in this adhesion is the shape of the fibres. Spatula-shaped ends on the hairs increase the adhesion forces. When a gecko puts its feet on the surface, its atoms intermingle with atoms in the surface enabling the weak Van-der-Waals forces to take effect. These weak forces are helped by the comparatively huge surface area of hairs, making them very strong to allow a gecko to climb.

2.2.1.2 Man-made nanomaterials

It is hard to say exactly when humans commenced with the preparation of nanomaterials, however, the best guess is when they started making fire, resulting in tiny nano-scale particles of soot in the ashes and smoke. Thus, by the Bronze Age, incidental copper NPs were already being widely used by human civilization. The earliest man-made NPs are often accredited to the ancient Romans, Egyptians, and Chinese. Though they had not fully understood the scientific implications that went with what they had created at the time, they could prepare NP solutions of gold and other metal with reasonable accurate control over particle size and composition. They successfully made flamboyant coloured antiquarian gold NPs which could be impregnated into a glass (as shown in Figure 2.2) to make stained glass and jewellery.

Figure. 2.2. The Lycurgus cup. Gold and silver NPs in the glass resulted in incredible and unique colour effects [9].

These colloidal gold and silver solutions were ingested as health tonics in many cases, specifically to treat high fevers and syphilis. By the 4th century, the Romans had successfully created a dichroic glass, which upon absorbing light showed different colours.

Nanoscience has advanced dramatically over the years with the improvement of both analytical- and synthesis techniques that allow control and ability to create and study nanomaterials. Scientists today are able to do what one would have usually seen a science-fiction movie about 50 years ago. However, since this is an ongoing research field, many factors are still not fully understood, for example, the toxicity of nanomaterials is still under much scrutiny.

2.2.2 The quantum confinement effect

When the size of semiconductor material is reduced to the nanoscale (nanomaterials), an electron and a hole are confined into dimensions approaching the atomic Bohr radius. At this point the density of states of conduction electrons can take only particular discrete values, resulting in what is called the quantum confinement effect. Confinement is the restriction of an electron to occupy only specific, discrete energy levels. Hence upon confining the dimensions of material to nanoscale, discrete energy levels form which widen the bandgap and shifts the optical spectrum to shorter wavelengths [10]. Thus, the ability to control the dimensions and composition of structures enables tailoring nanomaterials' properties for desirable applications.

Upon confinement of nanomaterials, properties such as the melting point, fluorescence, electrical conductivity, and chemical reactivity are all altered as a result of decreasing the dimensions of the particle. The confinement of nanostructures can be divided into different classes which will be discussed next.

2.2.2.1 One-dimensional confinement: two dimensional (2D) quantum structures

Electrons are confined in one dimension, these include thin films with properties dominated by surface and interface effects. The electrons are still free to move in two dimensions as it is the case in quantum wells.

2.2.2.2 Two-dimensional confinement: one dimensional (1D) quantum structures

The motion of electrons is confined in two dimensions, allowing them to move in only one direction. Electron confinement effects could manifest themselves in a transverse direction with the electrons only allowed to move in one dimension, these include quantum wires.

2.2.2.3 Three-dimensional confinement: zero-dimensional (0D) quantum structures

Examples of these types of materials are quantum dots (QDs). The electrons are confined in all three dimensions restricting their movement in all spatial dimensions. Quantum dots (QD) are small, semiconductor ‘dots’ with a size range of 2-10 nm, made up of approximately 100 to 100,000 atoms within the QD volume [11]. However, self-assembled quantum dots are usually 10-50 nm in size [12]. Quantum dots have quantized energy spectra.

Confinement in the dimensions of material results in an increase in the density of electronic states at the edge proximate of the bands (conduction and valence) of a quantum well relative to bulk material. Consequently, this leads to a higher concentration of charge carriers which contribute to the band-edge emission.

The density of states function describes the number of available energy states in a system which is important in calculating the carrier concentration and energy distribution of carriers in a semiconductor [12]. The motion of carriers in a confined semiconductor is determined by the number of free dimensions that electrons can move in.

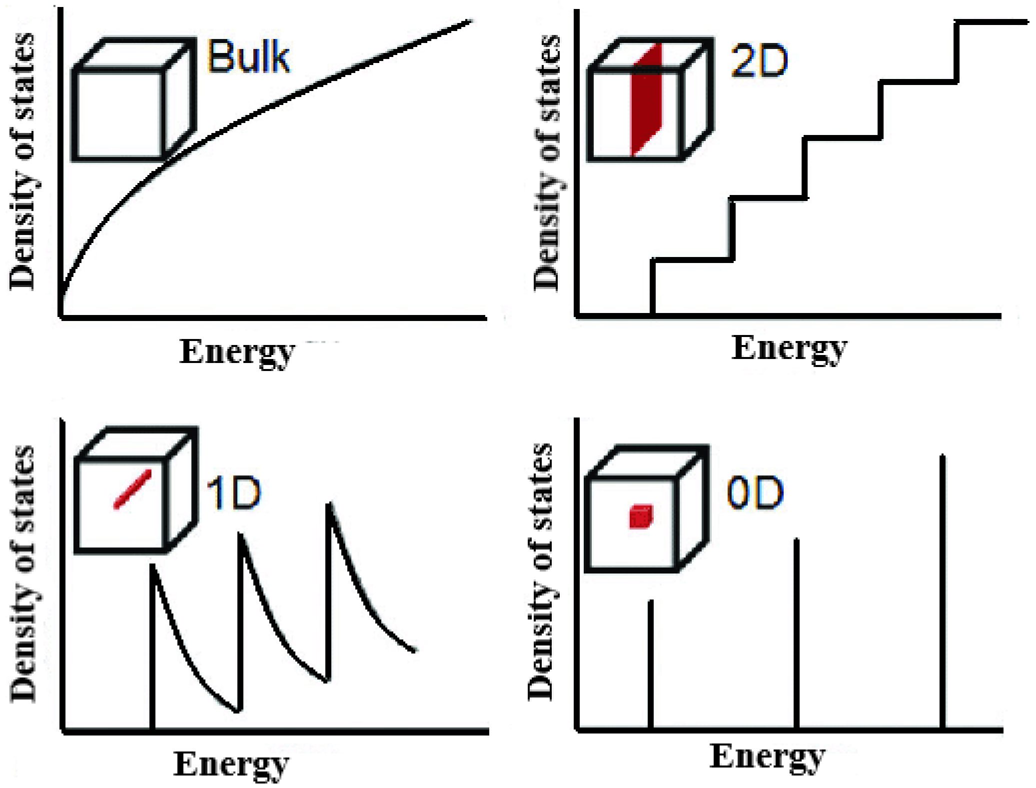

Figure. 2.3. Schematic showing density of electron states of a semiconductor as a function of energy for different confinement dimensions (i.e 2D, 1D, and 0D) [12].

The density of states of bulk, 2D, 1D, and 0D semiconductors are shown in Figure 2.3 with 0D having well defined and discrete energy levels. Quantum confinement effects become more pronounced when a semiconductor's dimensions approach that of the exciton Bohr radius. The semiconductor groups of IV, III-V and II-VI generally have a quantum confinement ranges of 1 to 25 nm [13]. An exciton Bohr radius is defined by:

$$a_B = \varepsilon \frac{m}{m^*} a_0 \tag{2.1}$$

where ε is the dielectric constant of the material, m* is the mass of the particle, m is the rest mass of the electron, and a_o is the Bohr radius of the hydrogen atom [14]. In CdS particles, the quantum confinement effect is usually observed to be strong in particles with sizes that are equal to or less than 5 nm in diameter [15][16]. At this level, the continuous energy bands observed in bulk materials do not apply, and the energy bands have discrete energy levels in quantum dots (Figure 2.4)

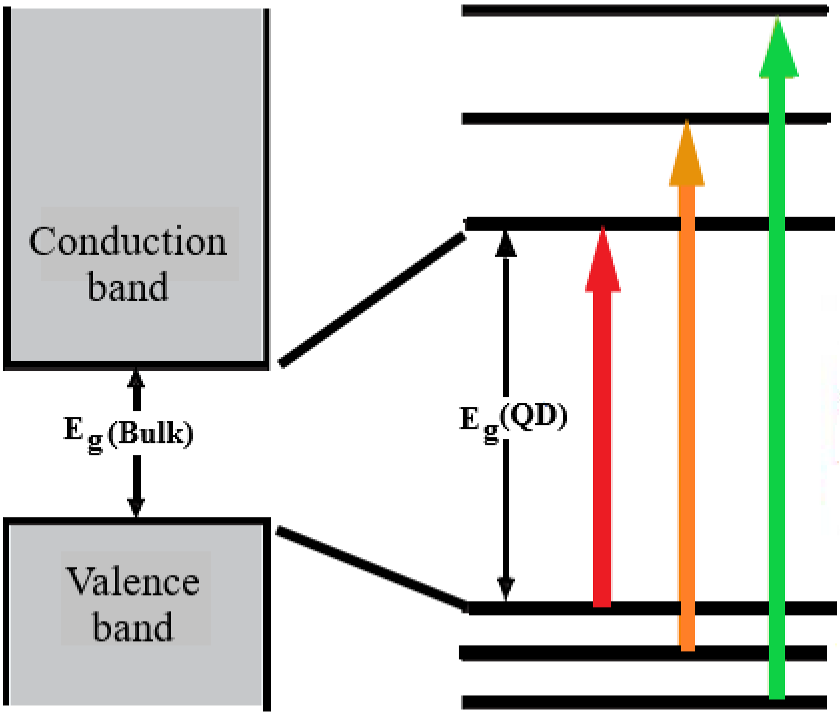

Figure 2.4. Schematic diagram showing continuous energy band semiconductor with that of discrete energy levels in a 0D structure.

There are two factors related to size that differentiate nanomaterials from their bulk counterparts; the actual particle size discussed above, which affect physical and electronic properties of the semiconductor material and the large surface area/volume ratio associated with nanomaterials of sensitive surface structure that determine chemical and physical properties.

2.3 Surface area

The surface area of NPs plays a fundamental role in the characteristic properties and potential applications of these NPs. Properties like reactivity, affinity, and sorption abilities are mostly determined by surface properties of particles. Thus, reducing the size of materials to nanoscale results in almost all the materials' atoms being exposed to the surface. For example: in the case of a 1 cm × 1 cm cube, the number of surface atoms is extremely small, in the order of $\sim 10^{-50}$ with a surface area of 6 cm^2. However, by only dividing the cube into eight other small cubes with half the sides of the original cube, the surface area will be doubled (Figure 2.5). Grassian *et al.* [17] discussed the consequence of decreasing the particle size to 1.2 nm, and have shown that this results in 76% of the particles' atoms being on the surface of the material.

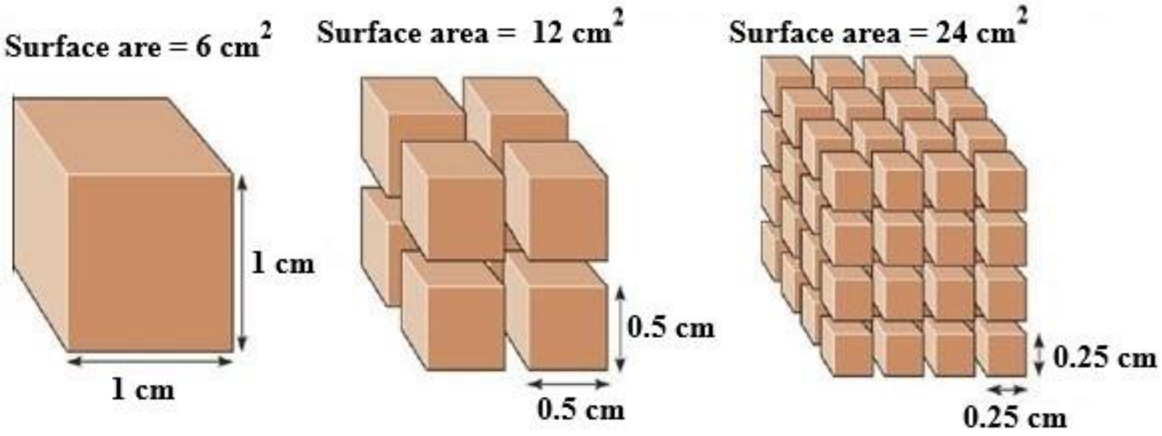

Figure 2.5. Schematic diagram illustrating the effect of reduced structural size on surface area in nanomaterials.

The increase in the number of surface atoms with decreasing volume results in a large surface area-to-volume ratio. Consequently, the overall free energy of NPs is dominated by surface energy.

2.4 Cadmium Sulfide (CdS)

CdS is a group II-VI semiconductor that has a room temperature direct band gap of 2.4 eV with an absorption maximum at 515 nm [18][19][20]. It is an organic compound and dissolves in acids while insoluble in water. It displays an intrinsic n-type conductivity triggered by sulfur vacancies that exist as a consequence of excess cadmium atoms. In nature, CdS occurs in two different crystal structures of hawleyite and the rare minerals greenockite. The more stable hexagonal wurtzite structure occurs in greenockite while hawleyite displays the cubic zinc blende structure [21]. Cadmium and sulfur atoms are four coordinate in a tetrahedral fashion, in the latter forms with the Cd-to-S bonds, as such showing both an ionic and covalent character. However, at high pressures a NaCl rock salt structure forms (Figure 2.6) [22] where each atom is coordinated to six other atoms in an octahedral fashion resulting in every atom having six neighbouring atoms of the opposite kind. The wurtzite form consists of hexagonal close packing (hcp) in which the stacking sequence of the atoms is ABABAB, while the zincblende and rock salt structure have the stacking sequence of the atoms as ABCABC, i.e., called cubic close packing (ccp) [23].

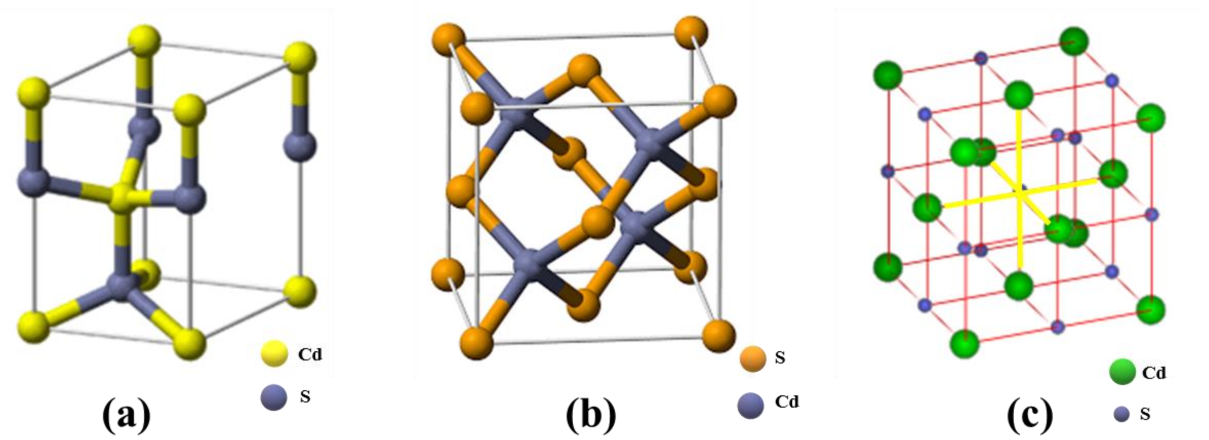

Figure 2.6. Schematic diagram showing the unit cell of the CdS crystal structure with (a) wurtzite (hcp), (b) zinc blend (ccp), and (c) rock salt (ccp) phases [23].

The wurtzite phase has been observed in both the bulk and nanocrystalline CdS with cubic and rock-salt phases only occurring in nanocrystalline CdS [24][25]. Hence, CdS NPs show different chemical, structural, and optical properties from the bulk counterparts. Particle size affects properties such as the melting point, electronic absorption spectra, band gap energy, crystal structure, and others in CdS NPs. Thus, the semiconductor NPs show a colour change of their fluorescence depending on the particle size. This is because the absorption wavelength of CdS NPs is directly affected by the quantum confinement effect. Since these nanostructures have the ability to crystallize in different structures upon size reduction, in different reaction conditions, the electrical properties are also size dependent.

2.5 Applications

Due to its high stability, and excellent structural, physical and chemical properties alongside its ease in availability, preparation and handling, CdS NPs can be used in a number of different fields of science. As a consequence of quantum confinement and surface effects, CdS NPs have unique optical, electronic, chemical, magnetic, and structural properties which are crucial in nanotechnology applications. In semiconductor electrodes, the distribution of atoms on the surface is crucial together with the high size/volume ratio [26].

2.5.1 Semiconductor photocatalyst

The band gap of the semiconductor increases with decreasing particle size and this also decreases the crystallinity of the photocatalytic material. This decrease in particle size also increases the surface area to volume ratio making it easier for the electrons and hole to reach the surface and reduce their recombination. These materials have two properties that are highly sought in water splitting photocatalysts: large surface to volume ratio and small particle sizes, which play a huge role in the elimination of electron-hole recombination [27][28]. Photocatalytic activity is directly related to the energetics of the particles since the band gap is related to particle size (quantum confinement). Thus the balance among band gap and particle size is important to achieve high photocatalytic activity in this system. The large surface area offers more active adsorption sites and photocatalytic reaction centres [29]. High crystallinity decreases the number of defects making it easy for photo-generated charges (i.e. electrons and/or holes) to reach the surface. Whilst small particle sizes help to decrease the electron-hole recombination probability by making the distance travelled by the charges to the surface shorter. But once an electron has migrated to the surface, it may become trapped. Thus the separation of the charges will reduce the recombination probability. As such, the use of cocatalysts on the CdS surface not only enhance the stability of the photocatalyst by preventing photocorrosion but also aids with charge separation [30].

Noble metals are ideal for this as they also provide effective proton reductions sites, facilitating proton reduction reaction. One of the most important things to consider when selecting a cocatalyst is its readiness to trap electrons from the semiconductor. The work function of the noble metal mostly determines their ability to trap electrons since they are greater than those of many semiconductors [31]. Noble metals with a lower Fermi level (larger work function) than the semiconductor could easily trap electrons. The electron trapping metal (noble) and the light harvesting semiconductor are ought to have compatible electronic and lattice structures to allow electron movement in the right direction of a semiconductor and metal junction [32][33]. During photocatalysis, the photoexcited electrons from the photocatalyst are excited from the CB to the noble metal cocatalyst, leaving the photogenerated holes in the VB of the photocatalyst. In this way, there are minimal chances for electron-hole recombination, which results in stronger photocatalytic reactions.

2.5.2 Luminescence applications

Luminescence was first introduced by a physicist and science historian Eilhardt Wiedemann in 1888. Often considered as ‘cold light’, it is defined as the spontaneous emission of radiation from an electronically excited species or from a vibrationally excited species not in thermal equilibrium with its environment [34]. Luminescence has played a key role in understanding the electronic properties of quantum dots. Optical absorption and emission of quantum dots are governed by the size of the dots. Unlike energies of the emission line of rare-earth ions which are energetically almost fixed, quantum dots enable tuneable line emission [35]. Different types of luminescence are often described by the mode of excitation.

- Photoluminescence (PL): Is the emission of light after excitation by electromagnetic radiation/photons.
- Radioluminescence (RL): Light is produced as a result of material bombardment with ionizing radiation such as beta particles, X-rays or gamma rays.
- Cathodoluminescence (CL): It is the emission of light upon excitation by the electron beam.
- Chemiluminescence: Light is emitted as the energy released from a chemical reaction.
- Bioluminescence: Light produced by the certain living organism from chemical reactions (*in vivo* biochemical reaction). This occurs in deep oceans where sunlight cannot reach.
- Triboluminescence: Light is generated by mechanical energy, frictional and electrostatic forces.
- Sonoluminescence (SL): In this phenomenon, excitation by ultrasonic wave is used to produce light.

Each of the above-mentioned luminescence mechanisms has advantages in specific fields. In this work, the focus is on PL that exhibit strong emission in the visible region while also considering the effect of surfactants (to be discussed). As mentioned above PL is the spontaneous emission of photons by de-excitation as a consequence of the possible physical effects of interaction of light with matter. PL involves the irradiation of a crystal with photons of energy larger than the optical band-gap energy of that material. In the case of a crystal scintillator, the incident light creates electron-hole pairs. During the recombination of these electrons and holes, the emissions will partly transform into non-radiative emission and partly into radiative emission.

2.5.2.1 Recombination mechanisms

As the electron returns to its ground state (Figure 2.7), it may do so by releasing a photon in radiative recombination (of the electron-hole pair) or by lattice vibrations (phonons) in non-radiative recombination [36]. A photon is emitted during the recombination of the electron and hole through radiative recombination and the energy of the photon is dependent on the change in energy state of the electron-hole system. In an indirect band gap semiconductor, energy transfer in the form of lattice vibrations is required to assist with photon emission. Hence, both non-radiative and radiative energy emissions occur due to phonon conversion to lattice vibrations that transport energy in form of heat. Thus in efficiently luminescent materials, radiative transitions are dominant relative to non-radiative transitions [37].

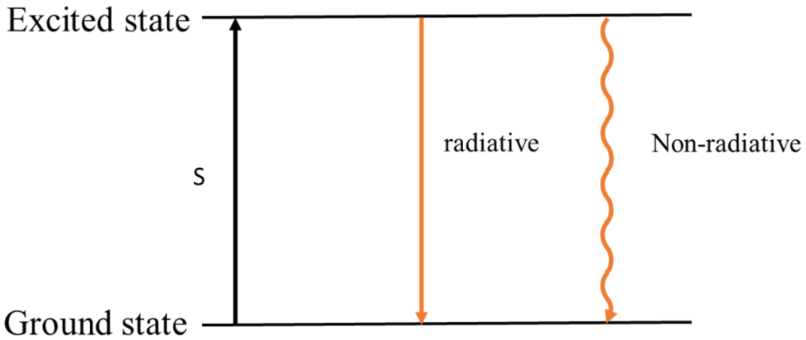

Figure 2.7. Energy level scheme of a photo-excited electron, S showing both the radiative and non-radiative return to the ground state.

Depending on the time it takes for a photon to fall back, luminescence can further be classified as either fluorescence or phosphorescence. Fluorescence has a lifetime less than 10^{-8} seconds and occurs as an exponential decaying afterglow that is independent of the excitation intensity and of temperature, upon removal of excitation. While in phosphorescence there exists another phenomenon of afterglow (decay is more slow with complex kinetics), often dependent on both the intensity of excitation and temperature, with a lifetime of more than 10^{-8} seconds. Metastable states created by the defect centres, activators, impurities, and electron or hole traps present in the lattice may delay the luminescent emission causing this effect since thermal activation of the metastable activator or traps is a pre-requisite to emission. Consequently, PL responsive material has applications in a wide variety of fields such as washing powder as a whitening substance to large-scale displays in plasma screens [37]. Luminescence types with very slow decays that have emission times ranging from minutes to hours may be good examples of phosphorescence. This type of luminescence is called long-lasting or persistent luminescence and it is commonly used in road safety and exit marking. PL is, therefore, a more general term that takes into consideration both fluorescence and phosphorescence [37].

2.6 Photoluminescence properties of (CdS)

The PL efficiency of CdS is determined by both radiative and non-radiative processes. The increased surface area in NPs leads to a number of dominant surface defects, hence non-radiative processes dominate in the excitation decay. The opening of new non-radiative pathways decreases the PL efficiency, while elimination of non-radiative pathways increases the efficiency. At the same time, also the kinetics of the PL can be influenced. Deep hole traps that act as PL centres compete with shallow hole traps for either free or shallow-trapped electrons [38]. If the density of the shallow hole traps is high, their recombination with electrons is preferred, and the PL intensity decreases. Adding S^{2-} ions, on the one hand, covers the surface of the NP with excess S^{2-} ions and therefore creates more sulfur dangling bonds.

A commercial CdS crystal with PL measured at room temperature results in two broad emission bands of PL. A green emission band from free excitons located below the conduction band results in the strongest peak energies of 2.53 eV (490 nm), PL1 (Figure 2.8). A second room temperature peak with the lowest energy is located at 696 nm (1.78 eV), known as the red emission band (PL6). Temperature effects on CdS semiconductor results in four more small green PL peaks at the low energy side of the main FE peak that were reported below 70 K [36].

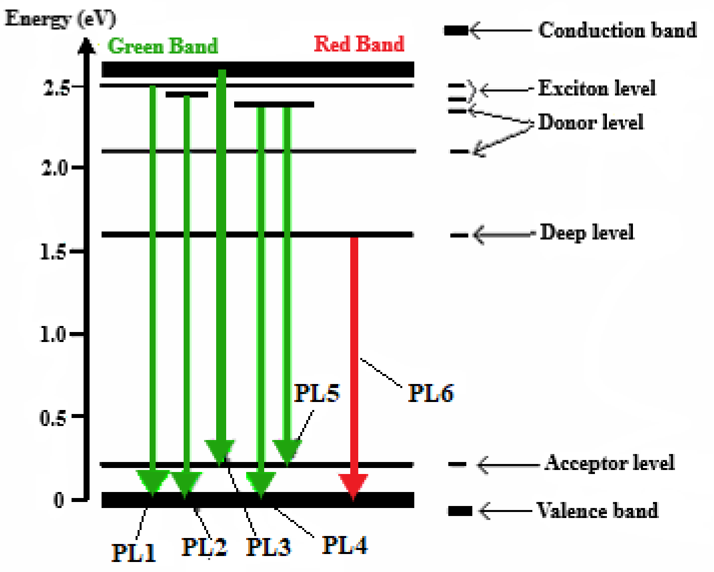

Figure 2.8. Schematic diagram showing optical transitions in the CdS crystal.

At low temperature, the PL spectra regularly show complex structures with a number of emission peaks which are due to transitions comprising of both band edge states and localized states of donor and acceptor centres [39]. At 515 nm (2.41 eV) PL2 is likely to originate from a bound exciton. A second peak (PL3) located at 523 nm (2.37 eV) is assumed to be a transition from the conduction band to the acceptor state and the peak PL4 at 532 (2.33 eV) is a transition from a donor level to the valence band. Another element of the green band, PL5 at 539 (2.30 eV) is likely to result from a donor-acceptor transition as previously discussed in the literature [40]. At the temperature range between 130 K and 20 K, another peak (PL7) located around 449 nm (2.76 eV) (whose energy is larger than the band gap value) becomes visible. The donor levels of CdS are attributed to S vacancies in the CdS crystals [41][42] while the acceptor states are attributed to S interstitials [43].

2.7 Absorption

Upon stimulation of material by photons, several processes such as scattering, reflection, absorbance, and excitation can occur. Having already discussed the emission of photons following absorption in PL, this section discusses the amount of light absorbed as a function of wavelength.

During the absorbance of a photon, its energy gets transferred to an individual electron. The energized electron gets excited to a higher energy level from the ground state (Figure 2.7). The electron transitions to a new eigenstate matching the amount of transferred energy. There is however only certain energy states that the electron can occupy during absorbance, and those are for wavelengths with energies corresponding to the energy difference between two different eigenstates of the molecule. The absorbance process ends in a very fast radiative process, on the order of 10^{-15} seconds [37][44]. Bulk CdS has an absorption edge at 515 nm (2.4 eV) which shows dependence on the particle size of the material. Blue shift in the absorption maximum of CdS with decreasing particle radius has been reported in literature [45][46][46].

2.8 Surface passivation

NP optical and electrical properties are very sensitive to surface modifications. They are usually very unstable due to high surface energies created by the reduced particle size. Organic and inorganic capping agents are thus employed to stabilize and passivate NPs surfaces. The different nature of capping agents is of high importance in the size distribution of NPs. Hence, an extensive number of different types of capping agents used to stabilize NP surfaces has been reported in the literature [47][24][48]. Organically capped CdS samples show that sulfur from the surfactants can effectively passivate CdS, leading to the quantum confinement effect and sharp excitonic peaks. During the preparation of CdS NPs, capping agents and/or surfactants are used to inhibit uncontrolled growth and agglomeration of the NPs [49]. However, quenching of the PL intensity caused by surfactants is prevalent, due to surfactants' propensities to act as Lewis acid [50]. The surfactants introduce surface defects that act as exciton traps which, in turn, alter the luminescence properties of the NP relative to crystals grown without capping agents. During the nucleation of NPs, the addition of the capping agent stops the growth process by making a compact, organic layer over the surface of the growing particles thus creating particles with smaller sizes. How fast the capping agent stops inhibits or stops the growth process ultimately determines the final particle size and it is therefore directly related to the concentration of the capping agent (i.e. the number of surfactants adsorbed onto the NP surface). High concentrations result in short growth periods which produce very small NPs with large free surface energy.

2.9 Semiconductor-metal junction

Semiconductor devices are largely a combination of dissimilar materials (semiconductors, metals, insulators). The interface between these materials is known as a junction and becomes crucial in electrical (transport) properties of the devices. When the semiconductor-metal contact forms, two different types of junctions may be formed depending on the semiconductor work function ($\emptyset$) and its relation with the metal:

- Schottky junction: $\emptyset_{\mathrm{m}} > \emptyset_{\mathrm{Semi}}$
- Ohmic junction: $\emptyset_{\mathrm{m}} < \emptyset_{\mathrm{Semi}}$

When a semiconductor has a lower work function than the metal, thus a higher Fermi level than the metal, a Schottky junction is formed. While an Ohmic junction is formed as a result of higher semiconductor work function than the metal. CdS ($\emptyset_{Semi} = 4.28\, eV$) is an n-type semiconductor with a lower work function than gold ($\emptyset_{\mathrm{m}} = 5.47$ eV) [51] [32][33].

2.9.1 Schottky junction

The junction is formed as a consequence of a lower semiconductor work function relative to that of a metal. This happens when a contact forms between an n-type semiconductor and a metal (Figure 2.9 (a)). In such a case, the semiconductor's Fermi level is higher (lower work function) than the metal Fermi level and thus allowing electron transfer from the conduction band level of the semiconductor to empty energy states above the metal Fermi level.

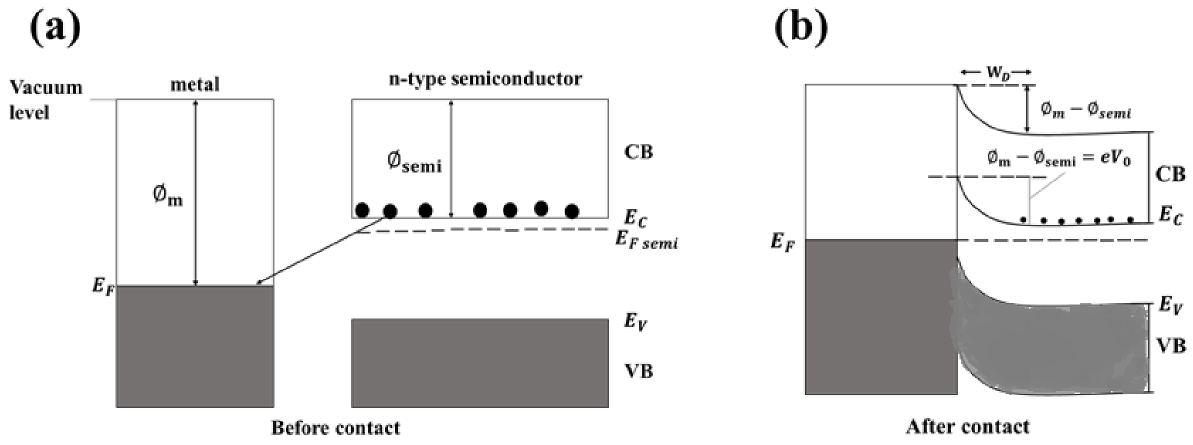

Figure 2.9. The Schottky junction between a metal and an n-type semiconductor (a) before contact, and (b) the band bending on the semiconductor side after contact.

Excess electrons result in a negative charge on the metals side, while positive charge builds up on the semiconductor side, leading to a contact potential. Upon formation of the contact between two metals, the charges reside on the surface. This is caused by high electron density found in metals (typically 1022 cm^{-3}). However, in the case of a metal and semiconductor, the contact leads to electron removal below the semiconductor surface up to certain depth. This is due to the low charge density on the semiconductor side (typically 1017 cm^{-3}) leading to the creation of a depletion region within the semiconductor [52].

During the creation of the Schottky junction between the metal and semiconductor, the two Fermi energy levels align and a positive potential is formed on the semiconductor side. A certain region in the semiconductor where the bands bend as the Fermi levels are aligned is called a depletion region (denoted W_o in Figure 2.9). Since the depletion region extends within the semiconductor (a certain depth) there is bending of the energy bands on the semiconductor side [53]. Bands bend up in the direction of the electric field (field goes from positive charge to negative charge, opposite of the potential direction). This means the energy bands bend up going from an n-type semiconductor to the metal (Figure 2. 9 (b)). Thus it is expected that quantum widening of the band gap of the CdS, with size reduction, would alter the Fermi level (thus work function) of the n-type semiconductor. Also, this will lead to electron trapping on the semiconductor NP surface (in the Au metal clusters) which, in turn, will prevent electron-hole pair recombination. It is expected that this will be evident in the optical properties and thus (upon successful formation of a Schottky junction) the materials' photoluminescent intensity should reduce since less electron-hole pairs will recombine. Thus, electrons on the surface of the NP will be available to interact with water molecules (as an example) for water-splitting.

2.10 Photoluminescence quenching

PL quenching refers to a process in which there is a decrease in the PL intensity of a given substance. This is often caused by a number of processes, such as excited state reactions, energy transfer, complex-formation, and collisional quenching. The quenching of CdS NP PL with the addition of Au has been reported in a study by Ibraham *et al* [54]. The decrease in intensity was reported to occur as a result of the effective segregation of photogenerated electrons and holes. As a consequence of the lower Fermi energy level, the photogenerated electrons in CdS are easily captured by Au. Thus there is a decrease in the radiative recombination.

In this work we investigate the formation of the Schottky junction on CdS-Au nanocomposites by depositing Au metal on the CdS semiconductor. The deposition is done using two different physical techniques (pulsed laser deposition and sputter coating). It is expected that the successful creation of the Schottky junction will manifest itself by decreasing the electron-hole recombination (PL quenching). Upon trapping of electron on the Au metal (CdS surface) *via* the Schottky junction, the electrons should be ready to interact with water molecules in the case of photocatalytic water-splitting application.

References

[1] A. Dowling, R. Clift, N. Grobert, D. Hutton, R. Oliver, O. O'neill, J. Pethica, N. Pidgeon, J. Porritt, J. Ryan, "Nanoscience and nanotechnologies : opportunities and uncertainties," *London R. Soc. R. Acad. Eng. Rep.*, vol. 46, no. July, pp. 618–618, 2004.

[2] "Is the Study of Phenomena and Manipulation of Materials At Atomic, Molecular and Macromolecular Scales, Where Properties Differ Significantly From Those At a Large Scale.," 2004. [Online]. Available: http://www.lei.lt/_img/_up/File/atvir/renginiai/Nanomaterials.pdf [Accessed: 01-Sep-2018]

[3] L. Filipponi, and D. Sutherland, *Nanotechnologies: Principles, Applications, Implications and Hands-on Activities*. Luxembourg, European Union, 2012.

[4] M. T. Amin, A.A Alazba, and U. Manzoor, "A review on removal of pollutants from water / wastewater using different types of nanomaterials," vol. 2014, 2014.

[5] K. Nordlund, "Introduction to Nanoscience," pp. 1–20, 2005.

[6] S. Cooper, "Naturally Occurring Nanomaterials," *Nat. Inc.*

[7] M. Berger, "Gecko nanotechnology," *Nanowerk*, 2006. [Online]. Available: https://www.nanowerk.com/spotlight/spotid=1182.php. [Accessed: 02-Sep-2018].

[8] U. States and R. Fearing, "Nanotechnology in Nature : Mimicking the properties of the Gecko Foot Materials :"

[9] S. Lohse, "Nanoparticles Are All Around Us," *Center for Sustainable Nanotechnology*. 2013.

[10] U. Jia, "Quantum confinement in nanoparticles," *nanoawesomeworld*, 2012. [Online]. Available: http://nanoawesomeworld.blogspot.com/2012/09/quantum-confinement-in-nanoparticles.html. [Accessed: 06-Sep-2018].

[11] "Quantum dot," *science daily*. [Online]. Available: https://www.sciencedaily.com/terms/quantum_dot.htm. [Accessed: 13-Sep-2018].

[12] T. Chakraborty, F. Peeters, and U. Sivan, Eds., *Nano-Physics & Bio-Electronics: A*

New Odyssey, 1st ed. Amsterdam-London-New York-Oxford-Paris-Shannon-Tokyo: Elsevier B.V, 2002.

[13] L. Prepared, C. R. King, and T. Ece, "Density of States : 2D, 1D and 0D," *Slides*, 2005.

[14] "Quantuam Confinement," *Chapter 1*, no. Yoffe 1993, pp. 1–19, 2004.

[15] N. Moloto, "Synthesis, properties and applications of Mn, Co, Ni and Cu chalcogenide nanoparticles," pp. 1–206, 2009.

[16] P. E. Lippens and M. Lannoo, "Calculation of the band gap for small CdS and ZnS crystallites," *Phys. Rev. B*, vol. 39, no. 15, pp. 10935–10942, May 1989.

[17] Y. Wang and N. Herron, "Quantum size effects on the exciton energy of CdS clusters," *Phys. Rev. B*, vol. 42, no. 11, pp. 7253–7255, Oct. 1990.

[18] I. A. Mudunkotuwa and V. H. Grassian, "The devil is in the details (or the surface): Impact of surface structure and surface energetics on understanding the behavior of nanomaterials in the environment," *J. Environ. Monit.*, vol. 13, no. 5, pp. 1135–1144, 2011.

[19] S. Jindal, "on optical and structural properties of Tb doped CdS," no. July, 2015.

[20] A. Dumbrava, C. Badea, G. Prodan, and V. Ciupina, "Synthesis and characterization of cadmium sulfide obtained at room temperature," *Chalcogenide Lett.*, vol. 7, no. 2, pp. 111–118, 2010.

[21] R. Bhattacharya and S. Saha, "Growth of CdS nanoparticles by chemical method and its characterization," *Indian Acad. Sci.*, vol. 71, no. 1, pp. 187–192, 2008.

[22] N.Wiberg, Egon, and A. F Holleman, *Inorganic Chemistry*, 101st ed. 2001.

[23] W. A.F, *Structural Inorganic Chemistry*, 5th ed. Oxford Science, 1984.

[24] K. P. Acharya, "Photocurrent Spectroscopy of CdS/Plastic, CdS/Glass, and ZnTe/GaAs Hetero-pairs Formed with Pulsed-laser Deposition." 2009.

[25] V. Singh, P. K. Sharma, and P. Chauhan, "Synthesis of CdS nanoparticles with enhanced optical properties," *Mater. Charact.*, vol. 62, no. 1, pp. 43–52, 2011.

[26] M.D. Knudson, Y.M. Gupta, A.B. Kunz, “Picosecond Electronic Spectroscopy to Determine the Transformation Mechanism for the Pressure-Induced Phase Transition in Shocked CdS,” 1999.

[27] P. P. Favero, M. de Souza-Parise, J. L. R. Fernandez, R. Miotto, and A. C. Ferraz, “Surface properties of CdS nanoparticles,” *Brazilian J. Phys.*, vol. 36, no. 3b, pp. 1032–1034, Sep. 2006.

[28] B. Girginer, G. Galli, E. Chiellini, and N. Bicak, “Preparation of stable CdS nanoparticles in aqueous medium and their hydrogen generation efficiencies in photolysis of water,” *Int. J. Hydrogen Energy*, vol. 34, no. 3, pp. 1176–1184, 2009.

[29] S. Shen, L. Guo, X. Chen, F. Ren, and S. S. Mao, “Effect of Ag2S on solar-driven photocatalytic hydrogen evolution of nanostructured CdS,” *Int. J. Hydrogen Energy*, vol. 35, no. 13, pp. 7110–7115, 2010.

[30] A. Kudo and Y. Miseki, “Heterogeneous photocatalyst materials for water splitting,” *Chem. Soc. Rev.*, vol. 38, no. 1, pp. 253–278, 2009.

[31] H. Yan, J. Yang, G. Ma, G Wua, X Zong, Z Lei , J. Shi, C. Li, “Visible-light-driven hydrogen production with extremely high quantum efficiency on Pt-PdS/CdS photocatalyst,” *J. Catal.*, vol. 266, no. 2, pp. 165–168, 2009.

[32] J. Yang, D. Wang, H. Han, and C. Li, “Roles of Cocatalysts in Photocatalysis and Photoelectrocatalysis,” *Acc. Chem. Res.*, vol. 46, no. 8, pp. 1900–1909, 2012.

[33] J. Hölzl and F. K. Schulte, “Work function of metals BT - Solid Surface Physics,” J. Hölzl, F. K. Schulte, and H. Wagner, Eds. Berlin, Heidelberg: Springer Berlin Heidelberg, 1979, pp. 1–150.

[34] J. Soc, “Analysis of Work Functions of Noble Metals in Ambient Atmosphere in Commemoration of Journal Award,” vol. 78, no. 1, pp. 16–22, 2015.

[35] B. Valeur and M. N. M. N. Berberan-Santos, “Molecular fluorescence: principles and applications,” *Mol. Fluoresc. Princ. Appl.*, pp. 1–30, 2012.

[36] C. Ronda and A. Srivastava, “Luminescence Science and Display Materials,” *Electrochem. Soc. Interface*, vol. 15, p. 55, 2006.

[37] A. Seyhan, “Photoluminesence Spectroscopy of CdS and GaSe,” no. September, 2003.

[38] K. V. R. Murthy and H. S. Virk, “Luminescence Phenomena: An Introduction,” *Defect Diffus. Forum*, vol. 347, no. June 2015, pp. 1–34, 2013.

[39] X. C. Wu, a M. Bittner, and K. Kern, “Synthesis , Photoluminescence , and Adsorption of CdS / Dendrimer Nanocomposites,” *J. Phys. Chem. B*, vol. 109, pp. 230–239, 2005.

[40] D. G. Thomas and J. J. Hopfield, “Optical Properties of Bound Exciton Complexes in Cadmium Sulfide,” *Phys. Rev.*, vol. 128, no. 5, pp. 2135–2148, Dec. 1962.

[41] C. H. Henry, R. A. Faulkner, and K. Nassau, “Donor-Acceptor Pair Lines in Cadmium Sulfide,” *Phys. Rev.*, vol. 183, no. 3, pp. 798–806, Jul. 1969.

[42] N. Susa, H. Watanabe, and M. Wada, “Effects of Annealing in Cd or S Vapor on Photoelectric Properties of CdS Single Crystals,” *Jpn. J. Appl. Phys.*, vol. 15, no. 12, pp. 2365–2370, Dec. 1976.

[43] B. A. Kulp, “Displacement of the Cadmium Atom in Single Crystal CdS by Electron Bombardment,” *Phys. Rev.*, vol. 125, no. 6, pp. 1865–1869, Mar. 1962.

[44] A. P. Bogdanyuk, N. S.; Davidyuk, G. E.; Shavarova, “Red-luminescence centers in CdS and CdS:Cu single crystals and their transformation by electron bombardment,” *Semiconductors*, vol. 29, no. 2, pp. 181–182, 1995.

[45] Skoog, “Fundamentals of analytic chemistry,” *Brooks/Cole*, p. 1088, 2014.

[46] R. Banerjee, R. Jayakrishnan, and P. Ayyub, “Effect of the size-induced structural transformation on the band gap in CdS nanoparticles . J Phys Cond Matt,” *J. Phys. Condens. Matter*, vol. 12, no. September 2015, pp. 10647–10654, 2000.

[47] V. Singh and P. Chauhan, “Synthesis and structural properties of wurtzite type cds nanoparticles,” *Chalcogenide Lett.*, vol. 6, no. 9, pp. 421–426, 2009.

[48] N. V. Hullavarad and S. S. Hullavarad, “Optical properties of organic and inorganic capped CdS nanoparticles and the effects of x-ray irradiation on organic capped CdS

nanoparticles," *J. Vac. Sci. Technol. A Vacuum, Surfaces, Film.*, vol. 26, no. 4, pp. 1050–1057, 2008.

[49] N. Ben Brahim, M. Poggi, N.B.H Mohamed, R.B Chaâbane, M. Haouari, M. Negrerie, H.B Ouada, "Synthesis, characterization and spectral temperature-dependence of thioglycerol-CdSe nanocrystals," *J. Lumin.*, vol. 177, pp. 402–408, 2016.

[50] S. F. Shayesteh, "Synthesis, optical and structural characterization of CdS nanoparticles," *Int. J. Nanosci. Nanotechnol.*, pp. 53–62, 2007.

[51] S. K. Mehta, S. Kumar, S. Chaudhary, and K. K. Bhasin, "Nucleation and growth of surfactant-passivated CdS and HgS nanoparticles: Time-dependent absorption and luminescence profiles.," *Nanoscale*, vol. 2, no. 1, pp. 145–52, 2010.

[52] S. Gupta, D. Patidar, N. S. Saxena, and K. Sharma, "Electrical study of thin film Al/n-CdS schottky junction," *Chalcogenide Lett.*, vol. 6, no. 12, pp. 705–713, 2009.

[53] "Lecture 9 : Metal-semiconductor junctions." [Online]. Available: https://nptel.ac.in/courses/113106062/Lec9.pdf.

[54] B. Van Zeghbroeck, "Principles of Semiconductor Devices," *Analysis*, 2011. [Online]. Available: https://ecee.colorado.edu/~bart/book/book/chapter3/ch3_3.htm. [Accessed: 20-Sep-2018].

[55] I. Ibrahim, H. N. Lim, O. K. Abou-Zied, N. M. Huang, P. Estrela, and A. Pandikumar, "Cadmium sulfide nanoparticles decorated with Au quantum dots as ultrasensitive photoelectrochemical sensor for selective detection of copper(II) ions," *J. Phys. Chem. C*, vol. 120, no. 39, pp. 22202–22214, 2016.

CHAPTER 3

Synthesis of nanomaterials

3.1 Introduction

Fabrication approaches for the synthesis of nanomaterials can be subdivided into two groups, namely, top-down and bottom-up approaches: the top-down approach entails the ‘*chopping’* down of bulk material to small pieces of nanomaterial. This approach mainly uses techniques to selectively remove micro-scale structures from the bulk material. However, this approach has some challenges in creating uniform NPs and it introduces internal stress and defects with contamination, making this approach unsuitable for the synthesis of very small materials with uniform shape [1]. The bottom-up approach, on the other hand, refers to the build-up of material from a single atom or molecular precursors to large nanostructures of certain shape or size using physical or chemical forces [2]. In nanostructures, electron movement gets confined in certain directions when an electron-hole pair is squeezed together as dimensions approach the atomic Bohr radius. Quantum confinement effects are therefore of high importance in tailoring new properties of nanomaterials that are different from the bulk material. NPs’ growth mechanism determines factors such as the size distribution function of NPs. The physical and chemical properties of the NPs have also been reported to be influenced by the reaction medium [3]. Nucleation and growth mechanisms are also dependant on various other external conditions, such as the synthesis temperature, concentration of the precursor and stabilizing surfactants and pH. These conditions can differ according to the synthesis method. Popular methods to synthesize CdS NPs include chemical precipitation [4], solvothermal [5], laser ablation [6], hydrothermal [7], photochemical [8], one-pot synthesis [9] as well as the mesoporous copolymer template method [10]. Figure 3.1 shows a summary of the bottom-up approach. In this work, the method is used for the preparation of CdS NPs and co-loading of gold clusters on the surface.

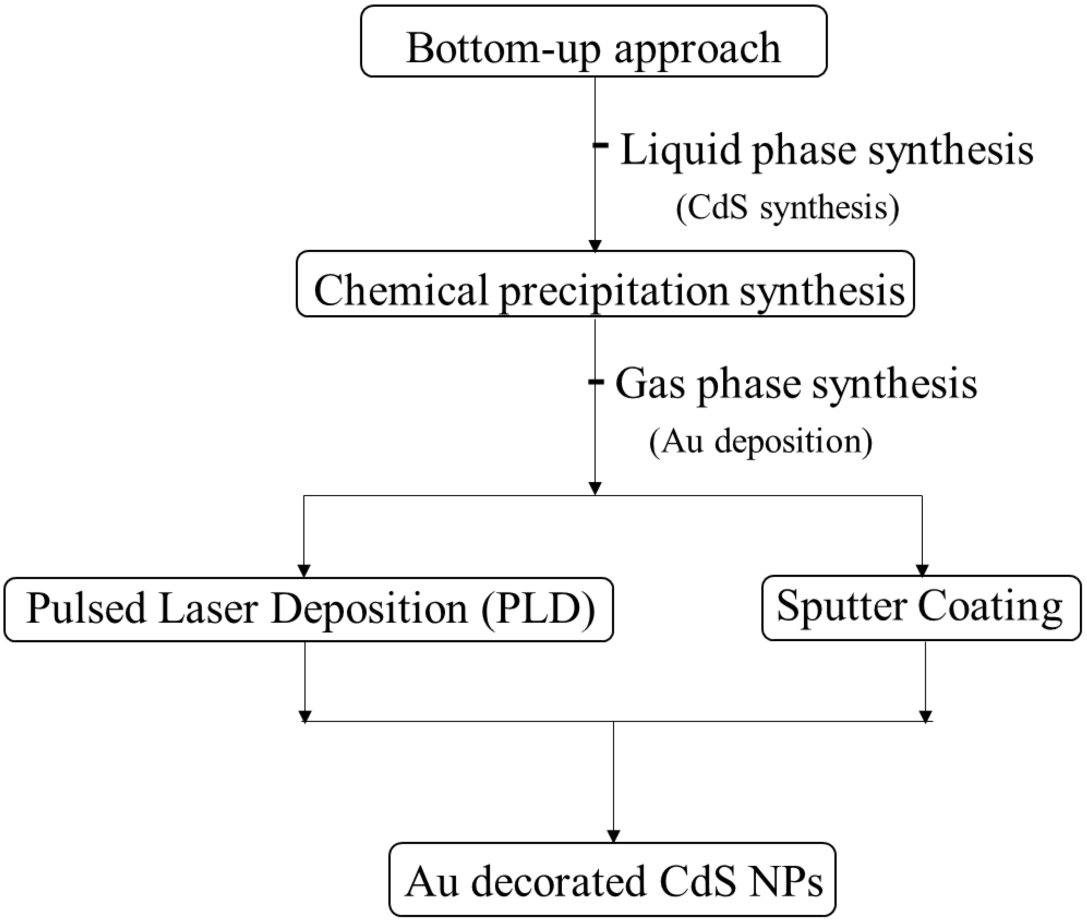

Figure 3.1. The layout of the synthesis approach used to prepare CdS NPs with Au coating.

3.2 Bottom-up approach

In this approach, atoms or molecules are arranged into larger nanostructures (Figure 3.2) using chemical or physical methods. This method generally has an advantage in the preparation of most nanoscale structures with the ability to generate a uniform size, shape, and particle size-distribution [11]. Synthesis of nanoclusters in this approach can either be by gas-phase or liquid-phase methods. The gas-phase method is mostly used in thin film synthesis and entails the carrying of metal vapour by a gas medium or vacuum onto some substrate. Some gas-phase techniques include: atomic layer deposition (ALD), chemical vapour deposition (CVD), and physical vapour deposition (PVD). The ability to build-up atomic layers from scratch allows for tuning of nanomaterials of certain sizes, structure, shape, and composition [12]. Liquid phase processes, make use of surface forces to construct nanoscale particles and structures. The processes involved in this phase include chemical precipitation, sol-gel methods, and methods relying on self-assembly.

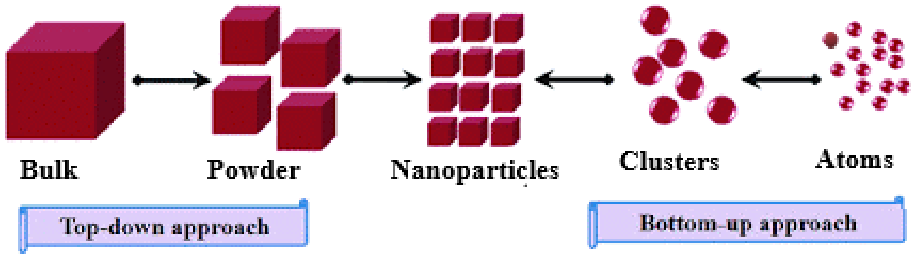

Figure 3.2. Schematic illustration of fabrication approaches in nanomaterial synthesis.

3.3 Liquid phase synthesis

Liquid phase synthesis (also is known as wet chemical method) is a NP synthesis approach mostly used in industry. Usually, the liquid phase preparation method entails the mixing of a solution of dissimilar ions with distinct quantities and exposing it to controlled heat, temperature and pressure conditions to stimulate the formation of insoluble NPs, as a precipitate. High temperatures, expensive energy sources or high pressures are not required in this process, making its use more attractive. This phase synthesis also allows more careful control of the stoichiometric composition of the end products and the NPs synthesized by this process can be stabilized or functionalized through the use of various surfactants [12]. Some of the techniques involved in this process are (i) chemical precipitation, (ii) hydrothermal method, and (iii) the sol-gel method.

3.3.1 Chemical precipitation

The chemical precipitation method is one of the various wet chemical synthesis techniques that are mostly adopted as a result of their simplicity, versatility, cost-effectiveness and the fact that this method allows for easy synthesis process on large scales for the rapid commercialization in industry. This technique can be carried out at low temperatures, resulting in bottom-up growth of NPs with varying size distribution controlled with capping agents. Bottom-up manufacturing involves building up of a NP from its atomic or molecular constituents. However, the chemical precipitation method includes not only the precipitation of the desired target ions but also the precipitation of any other existing ions in the solution [13]. During the precipitation process from the liquid phase, capping agents are added. These are used to interfere with the nucleating and growth process for particles and thus inhibiting agglomeration and control size [14]. Capping agents may play an active role during luminescence by enhancing photoluminescence through charge transfer. In some cases the efficiency is hindered by surfactant molecules that are covalently bonded with the surface atoms of the NPs, causing photoluminescence quenching [15][16]. Surfactants may cause hindrance in charge transfer of organic photovoltaic hybrid solar application.

3.3.2 Preparation of CdS NPs

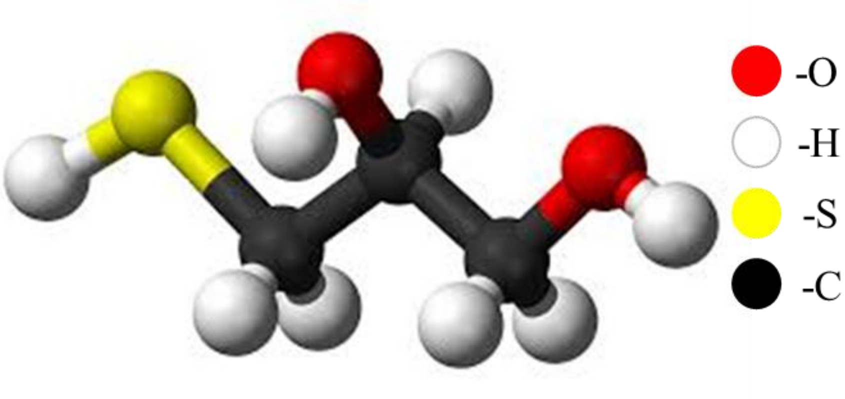

Figure 3.3. Schematic diagram of thioglycerol (TG) capping agent with the relevant atoms.

A number of different sized CdS NPs sets were synthesized using the wet chemical synthesis technique of chemical precipitation with TG ($C_3H_8O_2S$) as a capping agent to control the particle size. The TG molecular structure is shown in Figure 3.3 above. All the reactions were carried out at room temperature and standard atmospheric pressure. Cadmium chloride ($CdCl_2$) and sodium sulfide (Na_2S) were used as starting materials, acting as a source of Cd^{2+} and S^{2-} ions respectively. In a separate batch, double distilled water was added as a solvent with varying TG concentrations to control the growth. Initially, 0.1 mole (M) $CdCl_2$ and 0.1 M Na_2S were added in 50 mL of double distilled water separately with vigorous magnetic stirring [17]. The required amount of TG (as indicated in table 3.1) was then added to the Na_2S solution while stirring. The samples were stirred until the powder completely dissolved in the solvent. The Na_2S-TG solution was then added dropwise to the solution of $CdCl_2$ while constantly stirring using a magnetic stirrer. As particle growth started with the formation of precipitates, the colour of the solution changed from colourless to: orange in the absence TG (S0), yellow for 0.1 mL TG (S1), lemon-yellow for 0.2 mL TG (S2), lemon for 0.3 mL TG (S3), and whitish-lemon for 0.8 mL TG (S5). The five CdS precipitates with varying particle sizes were washed with ethanol five times to remove impurities and unreacted reactants. The precipitate was then collected by centrifuge for 5 minutes at 5000 rpm and then dried in an air oven for 10 hrs at 50 ℃. After 10 hrs in the oven, the quantity of the powder decreased. This is attributed to the evaporation and removal of impurities as well as excess water. The S3 sample was further annealed (In a ceramic tube furnace) to observe the effects of temperature on the NP crystallinity. Annealing was carried in an argon-rich atmosphere for 2 hrs at 200 ℃, 350 ℃, 500 ℃, and 700 ℃.

A second batch of CdS NPs were prepared under similar conditions with ethanol as a solvent in an attempt to reduce agglomeration. To completely dissolve the starting material, 0.1 mole (M) $CdCl_2$ and 0.1 M Na_2S were added in 50 mL of ethanol solvent separately with vigorous magnetic stirring for 1 hour. Following the same procedure as before, the resultant precipitate was then collected by centrifuge for 15 minutes at 6000 rpm.

Table 3.1. Summary of experimental variables used in the synthesis of CdS NPs at room temperature.

Sample	Starting material	Solvent	TG (mL)
S0	$CdCl_2$, Na_2S	Water	0.0
S1	$CdCl_2$, Na_2S	Water	0.1
S2	$CdCl_2$, Na_2S	Water	0.2
S3	$CdCl_2$, Na_2S	Water	0.3
S5	$CdCl_2$, Na_2S	Water	0.8
S0(eth)	$CdCl_2$, Na_2S	Ethanol	0.0
S1(eth)	$CdCl_2$, Na_2S	Ethanol	0.1
S2(eth)	$CdCl_2$, Na_2S	Ethanol	0.2
S3(eth)	$CdCl_2$, Na_2S	Ethanol	0.3
S5(eth)	$CdCl_2$, Na_2S	Ethanol	0.8

3.4 Gas phase method

In general, the gas phase method uses a gas, which is normally inert, at pressures high enough to stimulate particle formation, but low enough to permit the fabrication of spherical particles [18]. High temperatures elements are used to heat a metal and swiftly melt it. The heating is done such that the metal temperature exceeds the melting point but is still below the boiling point to achieve suitable vapour pressure. Throughout the heating process, the gas flow is constantly moving the evaporated metal away from the hot element, this is done by introducing the gas into the chamber and removing it again by pumps. As the gas cools the metal vapour, nano sized particles crystallize. The formed particles are still in liquid phase at this point since they are too hot to be solid. The liquid particles migrate, coalesce and amalgamate in a controlled environment and eventually crystallize into particles with spherical and smooth surfaces. When the liquid particles are further cooled in a controlled environment, they no longer grow and form solid particles.

3.4.1 Pulsed laser deposition

3.4.1.1 Introduction

Pulsed laser deposition (PLD) is a physical vapour technique that utilizes a focused high power pulsed laser beam to evaporate a solid target [19]. A pulsed laser beam is focused onto the desired target material inside a vacuum chamber in the presence of a background gas. A plasma plume is formed and the metal vapour is deposited on a substrate surface. As a materials processing technique, laser ablation was utilized for the first time in the 1960s, after the invention of a ruby laser [20]. The discovery of high-temperature superconductors in late 1986 reinvented the PLD technique. Lasers with a higher repetition rate than the early ruby laser made thin film growth possible, and since then PLD has evolved into a broadly applicable technique in the field of research leading to rapid development. This technique boasts of versatility and simplicity in implementation as advantages [21].

3.4.1.2 PLD Mechanism

The basic PLD technique setup for this is shown in Figure 3.4. A pulsed laser is focused onto a dense and homogeneous Au target material to be deposited on a substrate with stoichiometry intact. For an adequately high laser energy density (31.7 mJ), each laser pulse evaporates small volumes of the material forming a plasma plume. The vaporized material is emitted from the target as a forward-directed plume. The ablation plume is deposited on a pressed CdS NPs 4.5 cm away allowing material flux for particulates' growth.

The whole laser deposition process happens in a vacuum chamber with the laser situated outside the chamber, allowing for an extensive degree of freedom in the ablation geometry. The vapour consists of a collection of atoms, molecules, ions, and electrons, with the exact ratio and kinetic energy depending on the laser parameters (intensity, wavelength, pulse width) and to some degree on the target sample.

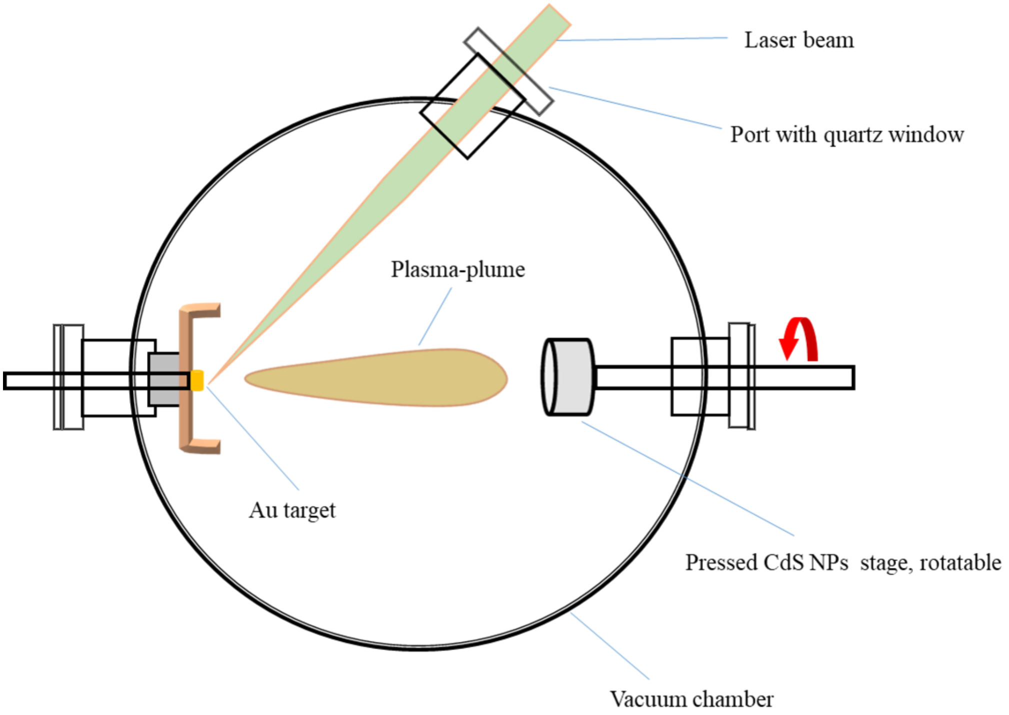

Figure 3.4. Schematic diagram of a basic PLD setup.

A number of parameters play a role in the quality of the resultant particulates. Important parameters include the thickness, and temperature of the substrate together and the absolute and relative kinetic energies and/or arrival constituents within the plume.

The PLD technique can generally be divided into four stages;

(i) The laser interaction with the target material.

(ii) Formation of the plasma plume from ablation of target materials.

(iii) Deposition of the plasma plume onto the substrate.

(iv) Nucleation and growth of a thin film on the substrate surface.

3.4.1.3 The laser interaction with the Au target material

A laser beam (Nd:YAG) with a power of 31.7 mJ is located outside the vacuum chamber (pumped to a vacuum pressure of 4.5×10^{-6} mbar) and is focused through a quartz glass onto the surface of an Au target material at an angle of 45° as shown in Figure 3.4. The laser beam gets focused on the Au target for a period of 1.5 min inside the high vacuum. The laser-to-target incident angle is chosen as such to avoid further interaction of the laser with the formed, outgoing plume. Upon interaction of a photon with the matter, the photon energy is coupled to the lattice through electronic processes. The absorption of the photon by material occurs in general over an optical depth of several nanometres upon which the energy in metals is transferred to the electrons directly and in non-metallic systems typically to the lattice. An oscillation field occurs as a result of a collision cascade created between atoms in the material due to the absorbed energy. An atom (or ion) can be removed from a target material if its total energy exceeds the binding energy [22]. Consequently electron excitations occur due to the oscillation of electrons leading to electron-lattice energy transfer. The absorbed energy per unit area by the target material depends on the fluence of the laser. The timescale for the electron energy transfer to the lattice in metals is typically in the order 1.5 picoseconds (ps) and strongly dependent on the thermal conductivity, specific heat, and electron-phonon coupling [23]. For non-metallic systems, the relaxation time is between 10^{-12} and 10^{-3} s. The vaporization process can be described by the heat flow theory where the surface temperature of the target at the end of the laser pulse is determined by the light absorption and thermal diffusivity [24].

3.4.1.4 Formation of the plasma plume from ablation of materials

In many PLD applications, the ability to predict and control the cluster composition of the ablation plume is critical. In particular, the presence of nanoclusters or particulates in the ablation plume can have an adverse effect on the quality of homogeneous particulates grown in PLD [25]. The material ablation mechanism and the total amount of emitted flux can change radically with a sufficient increase in fluence to induce explosive boiling of the target material. This process termed *phase explosion*, [26] is an explosive relaxation of the laser-induced melt into a co-existent mixture of liquid droplets and vapour. Such hydrodynamic ejection of droplet-like particulates is one illustration of macroscopic sputtering [21]. Another parameter that plays a critical role in a laser-induced plasma plume formation is the pulse length.

3.4.1.5 Deposition of the plasma-vapour onto the pressed CdS NPs.

Deposition of the ablated plasma onto a substrate can be described as follows: the particles from the plasma plume arrive at the substrate surface and are adsorbed, after which they may diffuse some distance before they react with each other and the surface atoms and start to nucleate. The manner in which the particles start to nucleate may determine the structure or morphology of the growing film or particulates. In this investigation, the substrate temperature, T_S was kept at room temperature during deposition. Along with supersaturation, S these are the major parameters in PLD. The two parameters are related by

$$S = k_B T_s ln(R/Re) \tag{3.1}$$

With k_B being the Boltzmann constant, R the rate of deposition and Re the equilibrium deposition value at temperature T_s [27]. Thus, supersaturation is directly related to the substrate temperature. Consequently, a small increase in the substrate temperature leads to large nuclei resulting in the creation of dispersed islands of the growing film. Another factor related to the temperature is the sticking coefficient. In this work (at room temperature) this takes on the value of unity as heating the substrate dramatically decreases the value of the sticking coefficient [28]. The (relatively) high sticking coefficient value causes the atom to stick properly to the substrate. Another significant factor in keeping the substrate temperature at room temperature is to ensure that the Au nuclei remains (relatively small) leading to Au cluster formation.

3.4.1.6 Nucleation and growth of particulates on the CdS surface

The deposition of the evaporated plume on to the substrate can be described as a sequence of events: the evaporated particles in the plume arrive on the substrate surface and are adsorbed. After this, the particles diffuse a short distance before they react with each other and the surface atoms and then start to nucleate. The manner in which the particles nucleate will determine the structure and morphology of the growing film. Under certain circumstances, like high substrate temperature, diffusional interactions within the film/particulate and with the substrate, underneath the growing film/particulate surface, may consequently modify film composition and film properties [21]. In general, the process of nucleation and growth is separated into three modes as shown in Figure 3.5:

1. Volmer-Weber growth mode
2. Frank-van der Merwe growth mode
3. Stranski-Krastinov growth mode

Volmer-Weber nucleation growth mode

In this mode, the atoms are strongly bound together in the thin film/particulate more than they are to the substrate resulting in nanoclusters. The intermolecular forces of attractions between the atoms attaching to the substrate surface are much stronger than the forces they form with the substrate material. As soon as a nucleation site of the first layer forms, another layer follows on top of it resulting in the growth of islands [29].

Frank-van der Merwe growth mode

This mode is also known as layer-by-layer growth, the interface energy is relatively low and layers form readily from nearly any size nuclei [29]. The bonds to the substrate are stronger than the intermolecular forces of attractions between the atoms and molecules attaching to the substrate surface. The nucleation sites in this mode are similar to the above mode with just every new material that arrives being stacked into the top layer exclusively. The nucleation and growth of islands that are only a monolayer thick are involved in full monolayer growth. These monolayers grow to fundamentally complete amalgamation and thus laying the foundation for the next film layer [30].

Stranski-Krastinov growth mode

Also known as the three-dimensional island growth mode follows a two-step process: Firstly films of the adsorbed material grow layer-by-layer up to several monolayers on a crystal substrate. Depending on the strain and chemical potential of the achieved films critical layer thickness can be reached, and beyond this growth with nucleation and amalgamation of adsorbate, island continues [31][32][33].

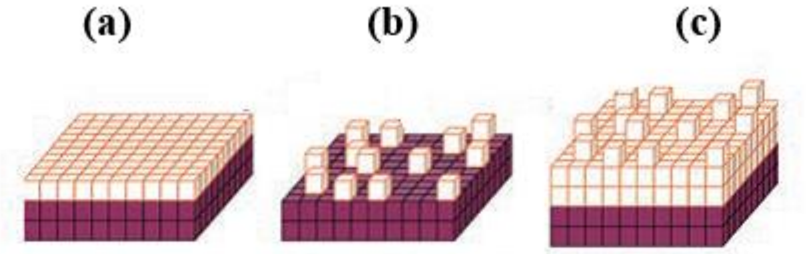

Figure 3.5. Thin film growth modes (a) Stranski-Krastinov, (b) Volmer-Weber, and (c) Frank-van der Merwe mode.

The selection of the growth mode in a substrate-film system depends on (a) the thermodynamics that relates the surface energies of the film and substrate and (b) the film substrate interface energy. It is expected that the Volmer-Weber mode to be the dominant method consistent with this work. This is because the time for the deposition is very short and thus the atoms are more likely to form more strong bonds with the CdS thin film. After successful deposition, the Au decorated CdS thin film is then crushed for homogeneously distributed CdS-Au nanocomposites.

3.4.2 Sputter coating

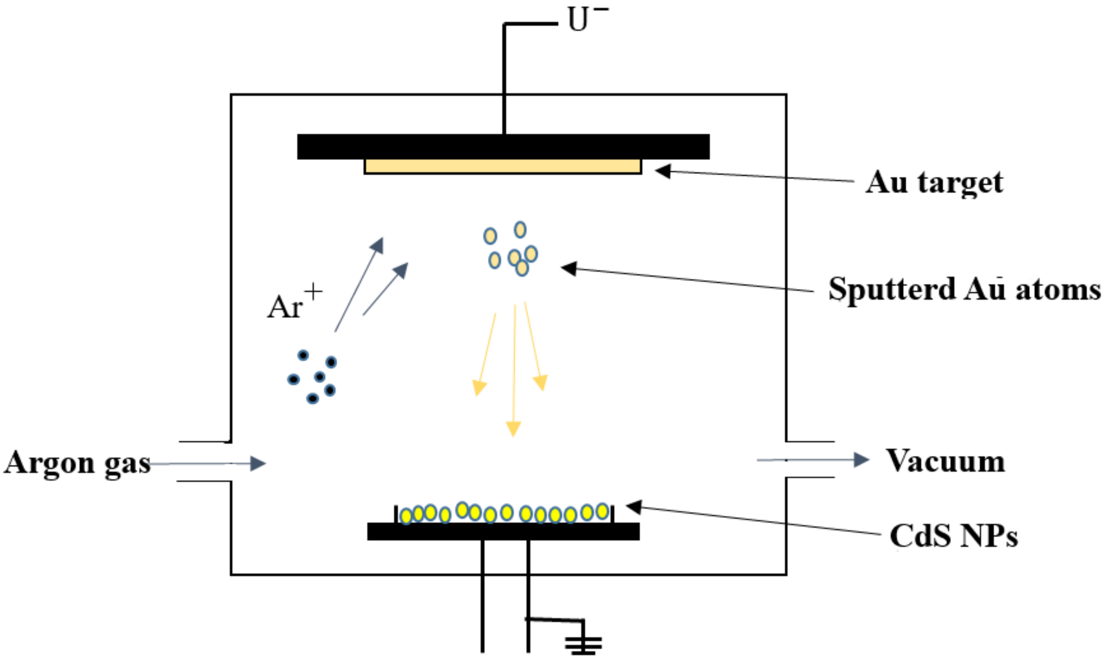

Figure 3.6. Schematic diagram showing the sputter coating setup for the CdS NPs with Au.

Sputtering is the expulsion of atoms by showering a solid target with energetic ions. It is a consequence of collisions amongst the incident energetic ionic-particles that result in recoil atoms from the target surface [34]. Upon reaching a low-vacuum pressure of 6×10^{-2} mbar, argon gas is pumped into the vacuum chamber as illustrated in Figure 3.6. A high voltage applied to an Au target ionizes nearby Argon. Once ionized, the Ar^+ ions accelerate toward the Au target and sputter Au atoms. Sputter coating is a widely used technique to coat electron microscope samples with metals (mostly Au). A conductive layer of Au is created to prevent charging, reduce thermal damage and improve imaging [35]. In this work ejected Au atoms by ionized argon plasma were deposited onto the CdS NPs' surface placed in the path of the resulting plume in a process that lasted for 1 min. Consequently, this technique is classified as a physical vapour deposition technique. Some of the modern, low voltage sputter coaters enable metal deposition at deposition rates of up to 1 nm/s in a low vacuum environment [36]. A ratio between the number of the atoms ejected from the target and the number of incident ions is known as the sputter yield, Y and measures the removal rate of surface atoms.

The theory of Sigmund [34] gives the sputter yield close to threshold (at low ion energy) as:

$$\mathrm{Y} = \frac{3}{4\pi^2}\alpha\frac{4\mathrm{M}_1\mathrm{M}_2}{(\mathrm{M}_1+\mathrm{M}_2)^2}\frac{\mathrm{E}}{\mathrm{U_s}} \qquad (3.2)$$

Where E is the ion energy, with M_1 and M_2 masses of the ion and the target atom (atomic mass units (amu)). The surface binding energy of the target atom is U_s and α a dimensionless parameter depending on the mass ratio and the ion energy. For low energy, and mass ratios M_2/M_1 lower than 1, α is of the order of 0.2. The equation can be understood as follows. The incoming ion imparts its momentum to the target atoms as could be understood by the term $\frac{4M_1M_2}{(M_1+M_2)^2}$ with a maximum when $M_1 = M_2$. Momentum transfer happens from induced ion collisions and must overcome the surface barrier (given by the surface binding energy U_s) for sputtering of a target atom to occur. Hence, the yield and surface binding energy have an inversely proportional relationship.

References

[1] S. Shibata, K. Aoki, T. Yano and M. Yamane, Journal of sol- gel science and Technology, 11, 279, (1998).

[2] L. Filipponi and D. Sutherland, *Nanotechnologies: Principles, Applications, Implications and Hands-on Activities*. 2012.

[3] H. R. Ghorbani, "A review of methods for synthesis of Al nanoparticles," *Orient. J. Chem.*, vol. 30, no. 4, pp. 1941–1949, 2014.

[4] V. Singh and P. Chauhan, "Structural and optical characterization of CdS nanoparticles prepared by chemical precipitation method," *J. Phys. Chem. Solids*, vol. 70, no. 7, pp. 1074–1079, 2009.

[5] A. Phuruangrat, T. Thongtem, and S. Thongtem, "Characterisation of one-dimensional CdS nanorods synthesised by solvothermal method," *J. Exp. Nanosci.*, vol. 4, no. 1, pp. 47–54, Mar. 2009.

[6] A. A. Lalayan, "Formation of colloidal GaAs and CdS quantum dots by laser ablation in liquid media," *Appl. Surf. Sci.*, vol. 248, no. 1–4, pp. 209–212, 2005.

[7] J. Zang, G. Zhao, and G. Han, "Preparation of CdS nanoparticles by hydrothermal method in microemulsion," *Front. Chem. China*, vol. 2, no. 1, pp. 98–101, 2007.

[8] M. Marandi, N. Taghavinia, A. I. zad, and S. M. Mahdavi, "A photochemical method for controlling the size of CdS nanoparticles," *Nanotechnology*, vol. 16, no. 2, pp. 334–338, Feb. 2005.

[9] H. Tong and Y.-J. Zhu, "Synthesis of CdS nanocrystals based on low-temperature thermolysis of one single-source organometallic precursor," *Nanotechnology*, vol. 17, no. 3, pp. 845–851, Feb. 2006.

[10] A. F. G. Monte, N. O. Dantas, P. C. Morais, and D. Rabelo, "Synthesis and characterisation of CdS nanoparticles in mesoporous copolymer template," *Brazilian J. Phys.*, vol. 36, no. 2a, pp. 427–429, Jun. 2006.

[11] D. Brabazon, E. Pellicer, F. Zivic, J. Sort, M.D Baró, N. Grujovic, K. Choy, “Commercialization of nanotechnologies-A case study approach,” *Commer. Nanotechnologies-A Case Study Approach*, pp. 1–315, 2017.

[12] S. S. Su and I. Chang, “Review of Production Routes of Nanomaterials.” Birmingham, UK, 2018

[13] R. Chauhan, A. Kumar, R. P. Chaudhary, and T. Education, “Synthesis and characterization of silver doped ZnO nanoparticles,” vol. 2, no. 5, pp. 378–385, 2010.

[14] H. Schmidt, “Nanoparticles by chemical synthesis , processing to materials and innovative,” pp. 331–343, 2001.

[15] S. K. Mehta, S. Kumar, S. Chaudhary, and K. K. Bhasin, “Nucleation and growth of surfactant-passivated CdS and HgS nanoparticles: Time-dependent absorption and luminescence profiles.,” *Nanoscale*, vol. 2, no. 1, pp. 145–52, 2010.

[16] M. Qasim, Z. Akram, S. Riaz, and S. Naseem, “Synthesis and Characterization of CdS Ink Comprised of Nanoparticles,” no. Lu 2011, pp. 1–10, 2012.

[17] V. Singh, P. K. Sharma, and P. Chauhan, “Synthesis of CdS nanoparticles with enhanced optical properties,” *Mater. Charact.*, vol. 62, no. 1, pp. 43–52, 2011.

[18] W. Luther, “Bottom - up Methods for Making Nanotechnology Products What Processes are used for Bottom - up,” *AZoNano*, pp. 1–6, 2004.

[19] U. Eason, Robert (Optoelectronics Research Centre University of Southampton, “Pulsed Laser Deposition of Thin Films: Applications-Led Growth of Functional Materials,” p. 707, 2007.

[20] D. Geohegan and G. k. Hubler, “Pulsed Laser Deposition of Thin Films,” *Pulsed Laser Depos. Thin Film.*, pp. 162–264, 1994.

[21] N. Popovici, “Pulsed Laser Deposition of Oxides,” *Pulsed Laser Depos. Oxides*, pp. 29–48, 2009.

[22] R. Eason, *Pulsed Laser Deposition of Thin Films*, no. 1. 2007.

[23] X. Y. Wang, D. M. Riffe, Y.-S. Lee, and M. C. Downer, "Time-resolved electron-temperature measurement in a highly excited gold target using femtosecond thermionic emission," *Phys. Rev. B*, vol. 50, no. 11, pp. 8016–8019, Sep. 1994.

[24] A. Zawadzka and P. Plociennik, "Laser ablation and thin film deposition," *… (ICTON), 2011 13th …*, pp. 89–112, 2011.

[25] G. K. H. D.B. Chrisey, Ed., *Pulsed Laser Deposition of Thin Films*. New York: Wiley-Interscience, 1994.

[26] A. Miotello and R. Kelly, "Laser-induced phase explosion: New physical problems when a condensed phase approaches the thermodynamic critical temperature," *Appl. Phys. A Mater. Sci. Process.*, vol. 69, no. 7, pp. 67–73, 1999.

[27] S. Soltan, *Interaction of Superconductivity and Ferromagnetism in YBCO-LCMO Heterostructures*. Cuvillier Verlag, 2005.

[28] X. Croizé, "' General view and off axis deposition technique study ,'" 1995.

[29] S. L. Brantley, A. F. White, and J. D. Kubicki, *Kinetics of water-rock interaction*, no. June 2014. 2008.

[30] R. Kumar, G. Kumar, and A. Umar, "Pulse Laser Deposited Nanostructured ZnO Thin Films: A Review," *J. Nanosci. Nanotechnol.*, vol. 14, no. 2, pp. 1911–1930, 2014.

[31] J. Venables, *Introduction to surface and thin film processes*. Cambridge University Press, 2000.

[32] J. V. Pimpinelli, Alberto, "Physics of crystal growth," vol. 19, 1998.

[33] D. J. Eaglesham, M. Cerullo., "Dislocation-free stranski-krastanow growth of Ge on Si (100)," *Phys. Rev. Lett.*, vol. 64, no. 16, p. 1943, 1990.

[34] D. Depla, S. Mahieu, and J. Greene, "Sputter deposition processes," *Handb. Depos. Technol. Film. coatings*, vol. 281, pp. 253–296, 1991.

[35] A. E.- Vladár, "Strategies for scanning electron microscopy sample preparation and characterization of multiwall carbon nanotube polymer composites," no. April, p. 2, 2015.

[36] “Plasma Sputter Coating.” [Online]. Available: http://www.mtixtl.com/machine-manual/Plasma Sputter Coating.pdf. [Accessed: 20-Oct-2018].

CHAPTER 4

Characterization techniques

4.1 Introduction

In this chapter, an overview of the principles of various characterization techniques used to study the structure, morphology, composition, topography and optical properties of cadmium sulfide (CdS) NPs are discussed in detail. To study the crystallinity and structural properties of the synthesized material X-ray diffraction (XRD) was employed. Generated X-rays are diffracted in crystal planes during interaction with CdS samples resulting in constructive interference defined by the Bragg equation. To study the topography, morphology, and composition the samples were scanned with a scanning electron microscope (SEM) which uses a focused electron beam to generate images from resulting secondary electrons. Energy dispersive X-ray spectroscopy (EDS) that is complementary to this technique detects the generated X-rays and gives information about the composition of materials. With transmission electron microscopy (TEM) electrons are transmitted through the sample to study the above-mentioned properties of nanoscale materials. This allows for below the surface composition analysis, which is an advantage TEM has over SEM. To further study the surface effects the Fourier transform infrared spectroscopy (FTIR) uses the vibration of atoms to identify molecules present on the surface. However, to look at the oxidation states of surface elements, X-ray photoelectron spectroscopy (XPS) is used. XPS also affords the opportunity to study, among other things, the work functions. Photoluminescence (PL) and ultraviolet-visible spectroscopy (UV-Vis) are used to study the luminescence properties and absorbance properties respectively. With PL, the presence of related defects is indirectly detected as well. ToF-SIMS is used to study molecular composition and stoichiometry, this technique allows the identification of the smallest nanoclusters. It employs pulsed ion Beam (Bi^{3+}) to remove molecules from the sample surface.

4.2 X-ray Diffraction (XRD)

XRD is a technique used to study the crystal lattice's structural properties for various crystalline materials. This technique can be used to determine the degree of crystallinity, phase identification, lattice parameters, and grain size in crystalline materials.

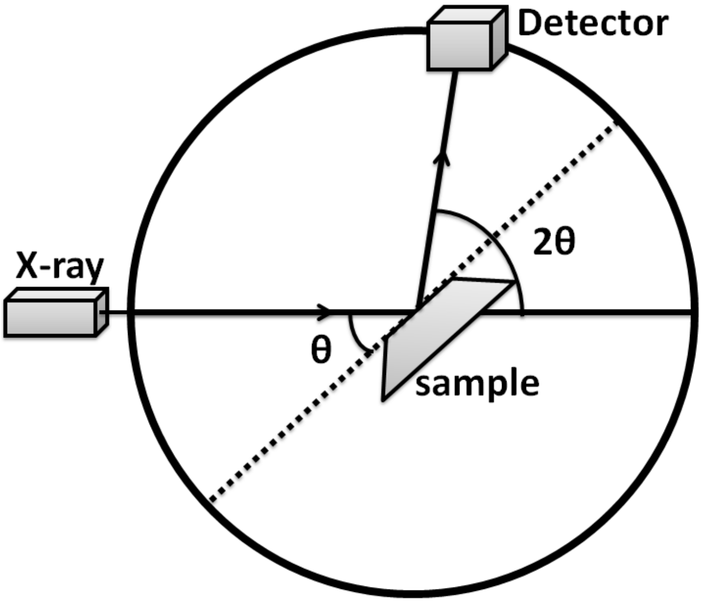

Figure 4.1. Schematic diagram showing X-ray diffractometer setup.

The discovery of X-rays in 1895 by Wilhelm Röntgen [1], and X-ray diffraction in materials (noting that X-rays have a wavelength similar to the interatomic distances in crystals) by Laue in 1912 [2] marked the beginning of this widely used technique. Figure. 4.1 shows an X-ray diffractometer consisting of three basic components in its most primitive form: an X-ray tube, a sample holder, and an X-ray detector [3].

The X-ray tube consists of a cathode (high negative potential) and an anode (ground potential) with a potential difference between them. The cathode made of a tungsten filament is heated to give electrons with just about enough energy to escape its surface. The high potential difference then accelerates the electrons from the filament to the anode and this electron beam strikes the anode with energy identical to the X-ray tube voltage (40 kV, 40 mA). These electrons are shaped in such a way that they strike the anode along a thin line of 0.4 by 12 mm [4]. Upon hitting the anode, these energetic electrons hit and remove electrons from the inner shells of the metal atoms. The electrons from the outer shells then fall to fill the unoccupied inner shells and in the process they lose their energy in the form of X-ray photons with characteristic energy and wavelength. In a copper (Cu) anode, the energetic electrons knock out the K-shell electrons. Outer shell electrons then fall to fill the K-shell vacancies, in the process emitting K_β and K_α (combined $K_{\alpha 1}$ and $K_{\alpha 2}$) X-rays. These X-rays have characteristic wavelengths of 0.1393 nm and 0.1542 nm respectively. When these X-ray photons exit the tube, they both reach the specimen. To produce a monochromatic X-ray source, a nickel (Ni) filter is often used.

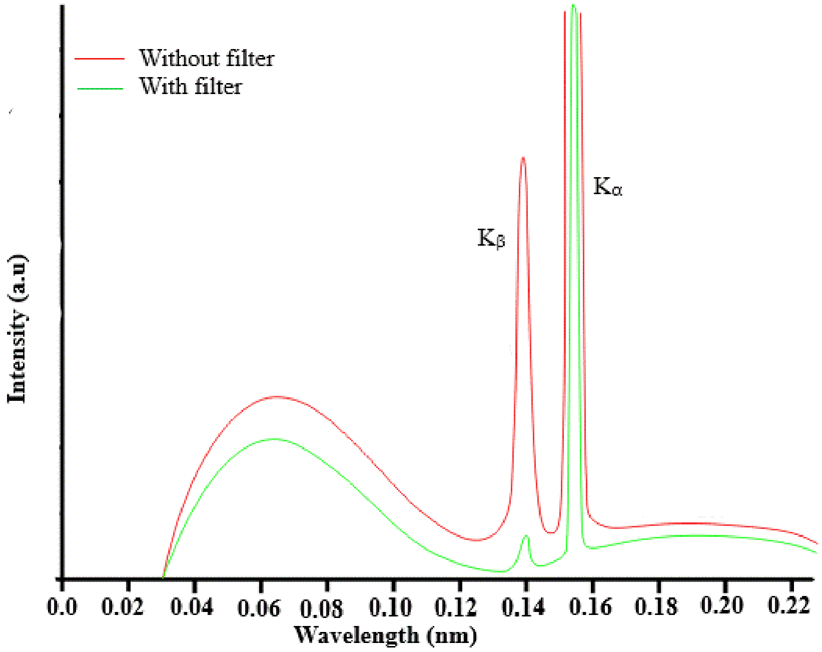

Figure 4.2. Characteristic X-ray emission for a Cu-source with and without a filter (Ni).

The Cu and Ni metals have a K excitation energy difference between the K_α and K_β peaks. As a result, the higher energy Cu K_β X-rays have about enough energy to excite the Ni metal. These X-rays are then strongly absorbed by the metal, while the Cu K_α X-rays do not have enough energy and are weakly absorbed [5]. Consequently, the Cu K_β X-rays don't go through the filter as their intensity is almost completely eliminated (Figure 4.2). The K_α X-rays intensity, on the other hand, is slightly reduced. The presence of the Ni filter thus results in a simpler diffraction pattern since it produces monochromatic X-rays.

The generated K_α X-rays pass through the filter and are directed into the specimen, where upon photon-matter interaction are diffracted in the crystal planes. Diffraction of monochromatic X-rays can be defined mathematically by Bragg's law, given by equation 4.1. When the diffraction conditions meet the requirements of this law, constructive interference is achieved.

$$n\lambda = 2d \sin \theta \tag{4.1}$$

The law relates the lattice spacing in a crystalline specimen with the X-ray wavelength and its diffraction angle. It is named after Sir W.H. Bragg and his son Sir W.L. Bragg who formulated it in 1913 [6].

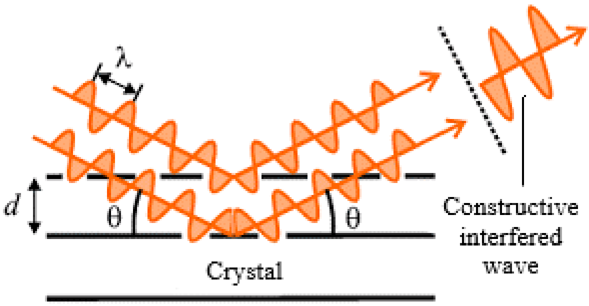

Figure 4.3. Schematic depiction of X-ray diffraction from lattice planes in a single crystal.

In equation 4.1, λ is the radiation wavelength of the X-rays, *d* is the lattice inter-planar spacing and *θ* is the angle between the diffracted X-ray and a lattice plane. The integer, *n* is the diffraction order, often unity. However, it is not really the planes in the crystal that scatter the X-rays (since planes are abstract mathematical constructs) but rather the atoms with their electronic clouds [7][8]. The diffracted X-rays (Figure 4.3) are then directed to a detector which is strategically placed in the path with the highest number of these X-rays. Since the scanned material is randomly orientated, the X-rays are moved through a diffraction angle range 2θ, to ensure that all the possible diffraction planes are obtained.

4.3 Electron microscope

This type of microscope makes use of an accelerated beam of electrons as its radiant source. Since the electron have a shorter de Broglie wavelength, up to a 100 000 times shorter than that of visible light photons [9]. It has a higher resolving power relative to other light microscopes, enabling it to reveal finer details in the smallest structures. The electrons are used in two ways to obtain information about a specimen; (i) the beam interacts with the specimen resulting in elastic and inelastic scattering, and (ii) the beam is passed through the specimen generating an image by interacting with the specimen on its way.

4.3.1 Scanning electron microscope (SEM) and energy dispersive spectroscopy (EDS)

In SEM a focused electron beam is rastered over the specimen surface to produce images. Upon interaction of the electron beam with the specimen, different types of information can be acquired from the specimen, depending on the type of interaction [10]. This technique can give information about the topography (surface features of material) as well as morphology (shape and size of the NPs making the material) [11].

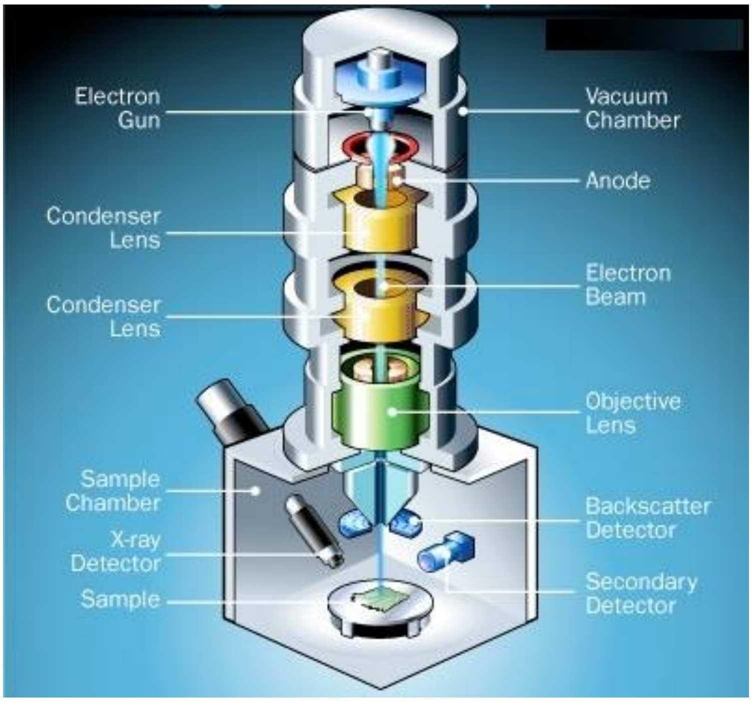
[redacted]

Figure 4.4. SEM setup illustration [12].

Components of the SEM are shown in Figure 4.4. A stable beam of electrons with adjustable energy is generated in the electron gun. The field emission gun (FEG) consists of a cathode, with a sharp metal tip. The metal tip is usually made of tungsten with a radius of less than 100 nm. An electric field occurs as a result of a potential difference applied between the first anode and the metal tip. This field is largely concentrated on the metal tip facilitating electron emission (emission current). The accelerating voltage of the gun is determined by the potential difference that occurs between the tip and the second grounded anode. Electrons travel faster at high accelerating voltages. The faster these electron travel down the column, the more power they have to penetrate the specimen. The system requires ultra-high vacuum conditions to keep the tip free of contaminants and oxidation.

The system uses stationery electromagnetic (EM) lenses to control (the diameter) and focus the generated electron beam down the column. There are two lenses used for this; (i) a condenser lens, to control the diameter of the beam. (ii) An objective lens is used to focus the beam onto the specimen. The field strength of the EM lenses can be varied by altering the current flux. When the electron beam interacts with the specimen (Figure 4.5), elastic and inelastic scattering events occur as a result.

During interaction of the electron beam with the electric field of the nucleus of the specimen atom, a direction change of the beam occurs.

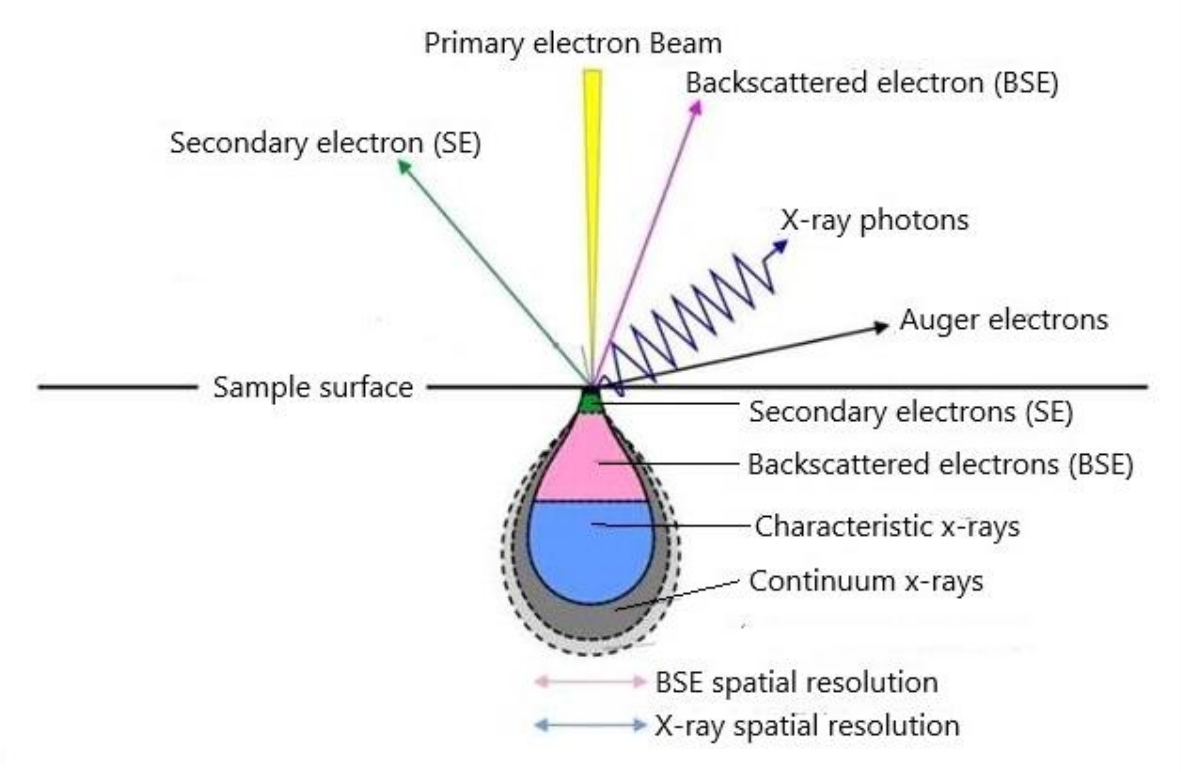

Figure 4.5. Sketch showing the events that occur as a result of the interaction of the electron beam with the specimen surface, along with the depth of the characteristic signals.

This change in direction is without a significant energy loss (less than 1 eV) in the electron beam. These are known as the elastic scattering events. In these events, if an electron is repelled back out of the specimen it is called the backscattered electron (BSE). BSE images obtained with this technique show compositional contrast that occurs due to different atomic number components and their distribution. However, in other events, during the interaction between the electron beam and the electric field of the specimen atom, the electron imparts its energy to the specimen atom. These are the inelastic events and often results in the expulsion of a secondary electron (SE). SEs usually have energy in the order of less than 50 eV [13].

The lost energy in the inelastic interaction of the electron beam with the specimen will produce two types of X-rays: firstly, characteristic X-rays occur when the beam ejects core-shell (inner) electrons from the specimen atoms. This results in an outer shell electron to fall to the lower energy state, into the remaining core hole. This electron emits its energy as a characteristic X-ray photon. The produced X-rays are characteristic of elements (related by atomic number), and thus allows one to identify the elements and their relative proportion. This requires a separate system (EDS) to measure these X-rays. The system is comprised of three basic components: (i) An X-ray detector which detects and converts X-rays into electronic signals, (ii) a pulse processor which measures the electronic signals to determine the energy of each X-ray detected; and (iii) a multiple channel analyser which displays and interprets the X-ray data [15].

Another type of X-rays that are produced is the continuum (Bremsstrahlung) X-rays. These are produced when the beam electrons interact with the Coulomb field of the nucleus of the specimen atom [14]. During the interaction, the beam loses energy that can be given off as continuum X-rays. Consequently, this energy loss has a continuous distribution of energy that is not characteristic of the atomic number; i.e. independent of the material used to generate X-rays.

4.3.2 Transmission electron microscope (TEM)

This technique is an improvement of the conventional optical microscopes as it enables higher magnification, allowing a much more detailed analysis. It can be used to study defects, crystallographic structure, particle size, morphology and composition of the specimen. High energy electrons (few hundred keV) are accelerated and focused towards an ultra-thin material. The electron beam interacts with the specimen as it passes through, enabling the formation of an image from the transmitted electrons. The formed image gets focused and magnified onto an imaging device.

TEM takes advantage of the quantum mechanical behaviour of the electron. The interaction of the electron with the material prevails due to the inherent nature of electrons which are quantum mechanical objects. Electrons have both a wave and particle nature, with their de Broglie wavelength significantly smaller than that of light and so they have a higher resolution capability. This allows the examination of finer details such as a single column of atoms, which is tens of thousands of times smaller than the smallest resolvable object in a light microscope [16].

The technique can be described using three basic components (Figure 4.6): (1) an electron gun, (2) the image-producing system, and (3) an image recording-system. The electron gun is used to produce a beam of electrons that is focused on a condenser system on to the specimen. The image-producing system has in it, the objective lens and retractable specimen stage, and intermediate and projector lenses through which the electron is passed to form a real, and highly magnified image.

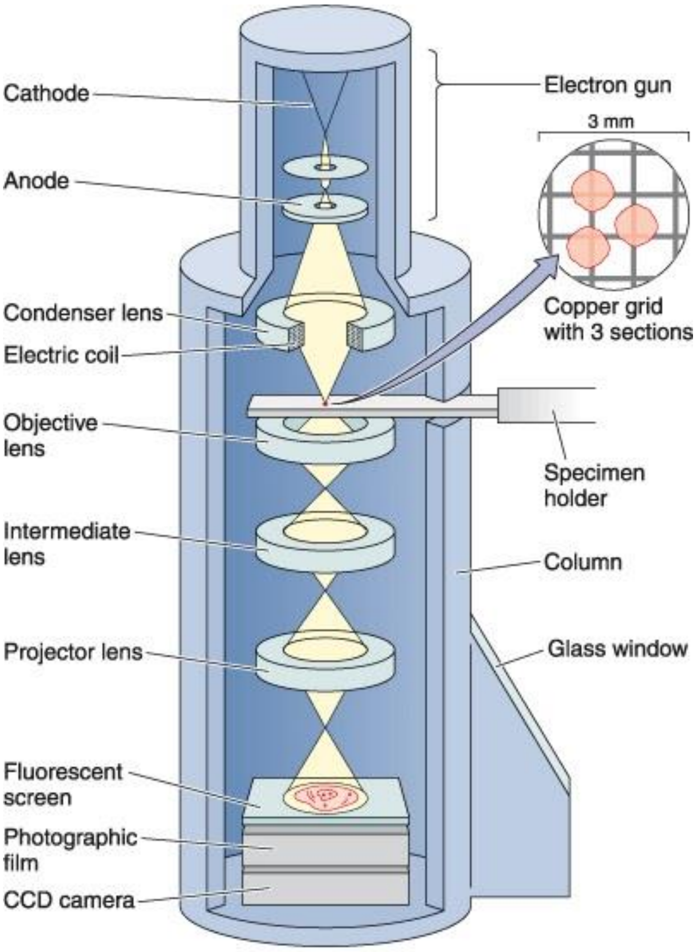

Figure 4.6. Schematic diagram showing TEM setup [18].

The formed image is however still not seen with a human eye and thus the electron image needs to be converted. The recording system consists of a fluorescent screen that displays and focuses the image, with a digital camera for permanent images. In addition, a vacuum system, consisting of pumps and their associated gauges and valves, and power supplies are required [17].

Electrons are generated by heating the cathode made of either a tungsten filament or, in high-performance instruments, lanthanum hexaboride (LaB_6). In between the cathode and anode, a voltage is applied to accelerate the electron. Only after the high voltage electrons stabilize, can they pass through a central aperture. This is done at constant energy to ensure a reasonable operation as the control and alignment of the electron gun are crucial to obtaining good images.

The condenser lens system between the electron gun and the specimen is used to control the beam intensity and angular aperture. A double lens is often used to converge the beam onto the specimen.

The specimen is loaded onto a very thin copper grid with a retractable specimen stage, this allows the electron beam to pass through the specimen. The beam reaches an objective lens with a short focal length (1-5 mm) below the stage. At this point, there is a real, intermediate image that will be further magnified by the projector lens or lenses. A single projector lens may provide a range of magnification of 5:1, and by the use of interchangeable pole pieces in the projector, a wider range of magnifications may be obtained. To allow a greater range of magnification and give an even better overall magnification without an equal increase in the physical length of the column of the microscope, modern instruments often use two projector lenses. The monochromatic electron image will only be visible to a human eye by either allowing the electrons to fall on a fluorescent screen fitted at the base of the microscope column or by capturing the image digitally for display on a computer monitor.

4.4 Ultraviolet-visible spectroscopy (UV-Vis)

The technique relies on the interaction of light with matter, giving information about the band structure of the sample. Absorption in the ultraviolet-visible region of the electromagnetic spectrum gives molecules in a low-energy atomic orbital enough energy to make electronic transitions to higher-energy orbitals. However, to make the transition, the molecules/ atoms must have exactly the same energy as the energy difference between the two energy orbitals [19]. A photon of light with energy ($h\nu$) is used to promote the molecules/ atoms. The initial intensity (I_0) of the light that is passed through the sample (shown in Figure 4.7) is compared to the final intensity of the light after it has passed through the sample to look at how much light was absorbed.

The amount of light transmitted through the sample is defined by transmittance (T) as the ratio I/I_0 and often conveyed as a percentage ($\%T$). The transmitted light is related to absorbance (A) by the following equation:

$$A = -\log\left(\frac{\%T}{100}\right) \tag{4.2}$$

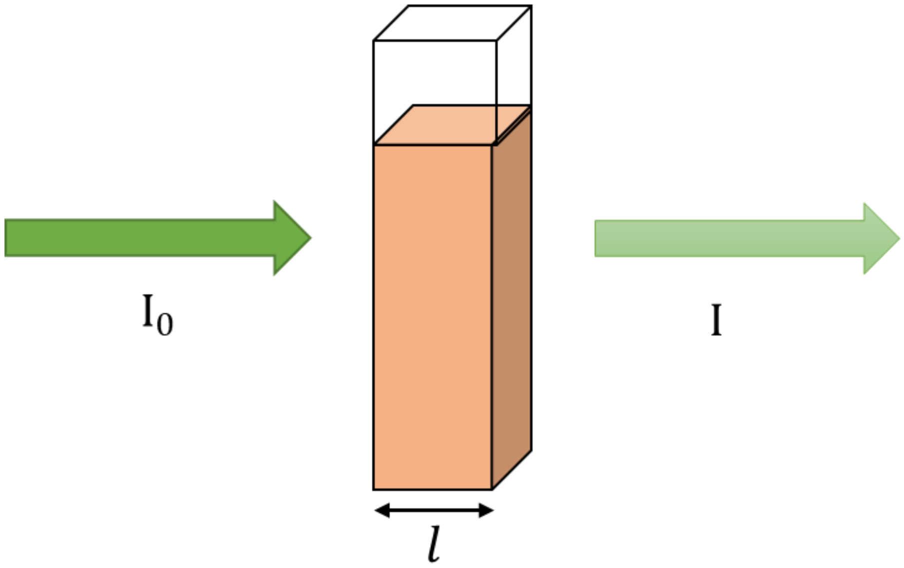

Figure 4.7. Schematic diagram showing electromagnetic radiation being transmitted through the transparent material.

A typical UV-Vis spectrophotometer has two light sources to cover the ultraviolet (190-400 nm) and visible (300-2500 nm) spectral regions, with deuterium (D2) and tungsten (W) lamps respectively.

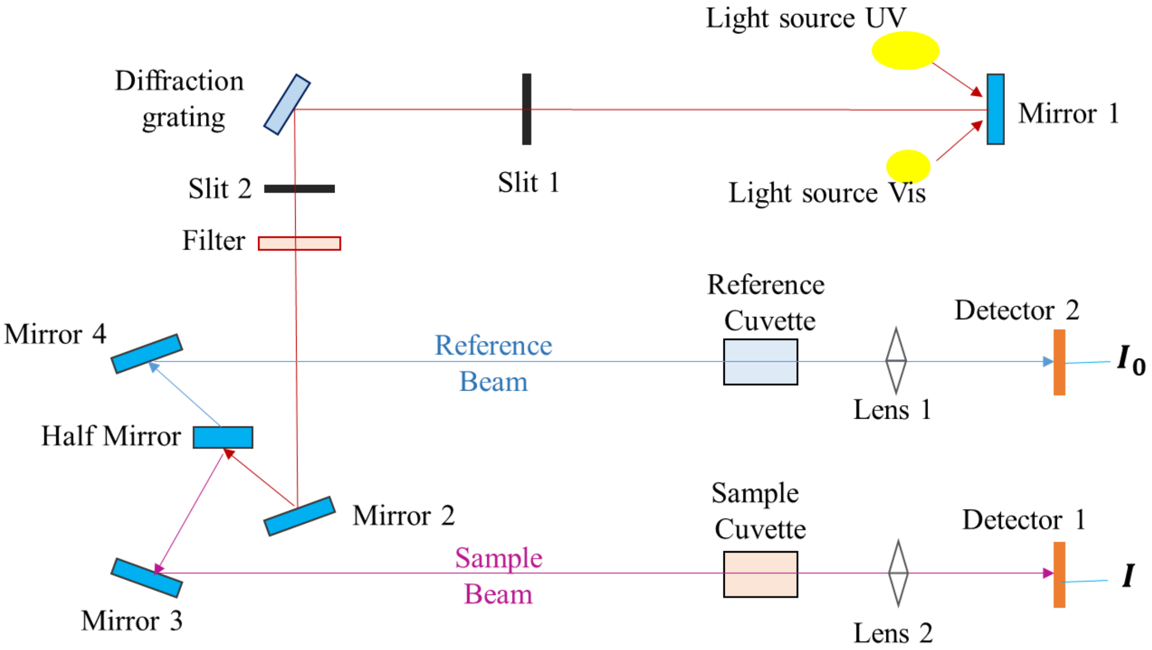

Figure 4.8. Schematic diagram showing components of the dual-beam of the UV-Vis spectroscopy system.

Figure. 4.8 shows components of a dual-beam UV-Vis spectroscope. A diffraction grating (prism) is used to first separate a beam of light from, either one of the sources or both, into its component wavelengths. The half mirror further splits every single wavelength (monochromatic) beam into two equal intensities (beams). One of these beams will be passed through the reference cuvette containing a transparent solvent. The other beam will go through the sample cuvette, which contains the sample to be studied. The sample is dissolved in a transparent solvent identical to that in the reference cuvette. Electronic detectors labelled 1 and 2 then measure the intensities of the light beams from the reference cuvette and the sample cuvette respectively, and then compare them. The reference beam has intensity defined by I_0, and is expected to have little or no light absorbed as it passed through the solvent [20]. Some of the sample beam intensity is expected to be absorbed, with the measured intensity defined as I. The spectrometer normally scans through both the ultraviolet (UV) and the visible (Vis) portions of the spectrum very quickly.

4.5 Photoluminescence (PL)

PL is a non-destructive technique that uses photons of light to probe the electronic structure of materials. The photons aimed at the specimen are absorbed and give away their energy to the material. This process is known as photo-excitation, and the energy imparted onto the material can be given out through the emission of light (luminescence) again. In such a case where a photo-excited specimen emits light, it is referred to as photoluminescence.

The photo-excitation process is responsible for promoting electrons within the material to a higher energy state (S_0 to S_2) as shown in Figure 4.9. However, after some time (as will be discussed later) the electrons return to the lower equilibrium states, giving out the excess energy in the process. The energy is dissipated through the emission of light in a radiative process. This energy can also be dissipated through vibrations, in a non-radiative process. On its way to the equilibrium state, the electrons pass through other energy states in between in this process. The energy of the emitted light relates to the energy difference between S_0 (equilibrium states) and S_2 (excited states). Consequently, the input of the radiative process is related to the intensity of the emitted light [21].

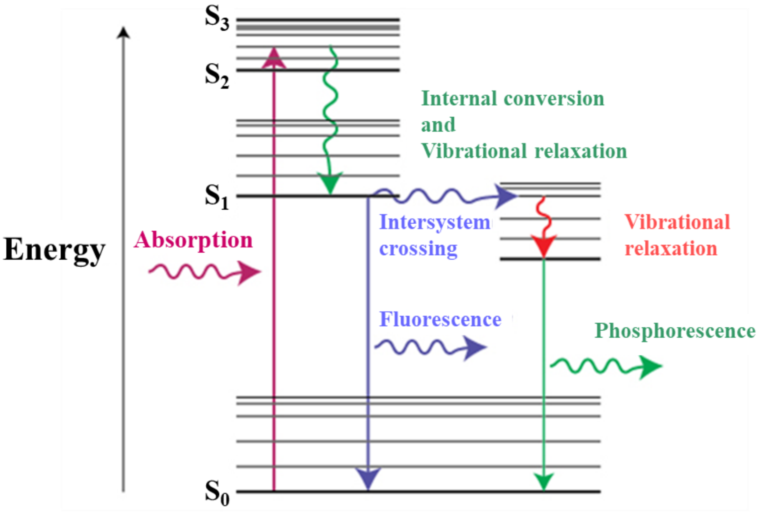

Figure 4.9. The principle of PL spectroscopy [22].

Some of the emitted photons have lower energy than the absorbed energy. There are two common types of phenomenons that cause this: fluorescence and phosphorescence. Fluorescence have a short life time of 10^{-8}-10^{-4} s. In phosphorescence, the energetic electrons undergo intersystem crossing into a state with different spin multiplicity. This phenomenon undergoes a radiational transition with a lifetime from 10^{-4}-10^{-2} s, which is much longer than fluorescence.

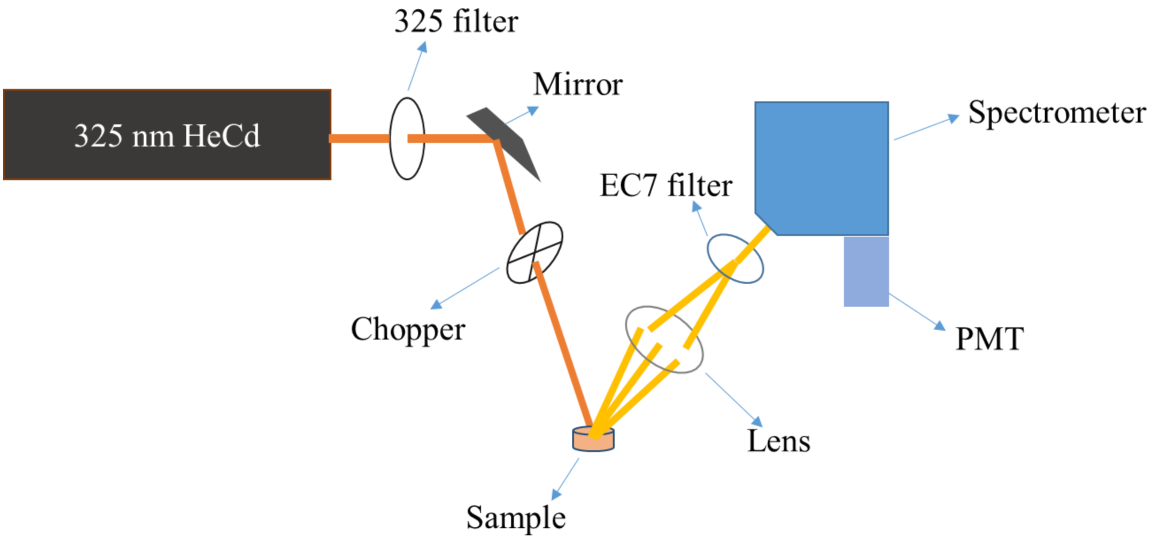

Figure 4.10. Sketch showing a setup of the 325 nm HeCd laser PL system.

In Figure 4.10, a HeCd laser (orange) passes through a filter that permits only 325 nm wavelength to pass, making sure it's of a single wavelength. The 325 nm laser is reflected off a mirror that transmits 10% of the incoming laser, reflecting 90%. On its way to the sample, the laser light goes through a chopper that varies its frequency depending on the chopper speed.

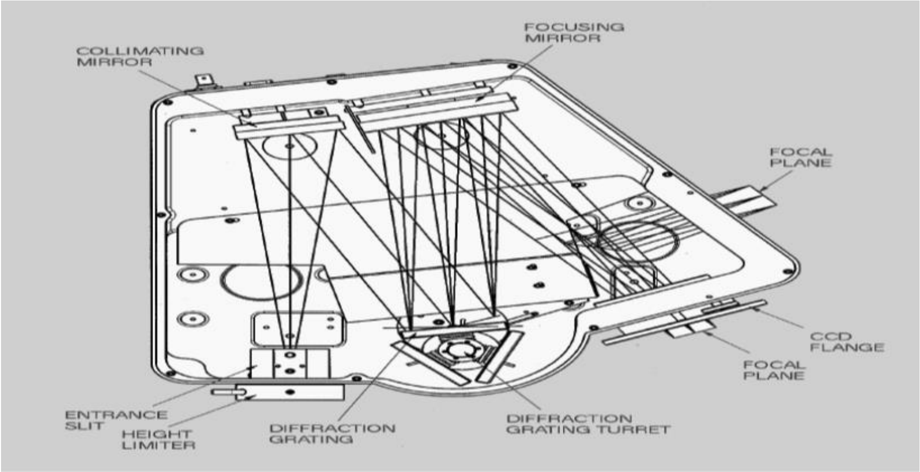

Figure 4.11. Internal workings of a spectrometer showing the diffraction of light.

Once the laser hits and excites the sample, photons of light (yellow) are emitted in various direction. The emitted light is focused with a UV-transparent lens to the EC7 filter. This filter is located in front of the spectrometer entrance and blocks the 325 nm wavelength, allowing higher wavelengths in. When light enters the spectrometer (Figure 4.11) through the entrance slit, it is collected by the collimating mirror and reflected into a grating, where it is dispersed into individual wavelengths. The diffracted light is then reflected the focusing mirror, to the detector. Each wavelength leaves the grating at a different angle thus each has a different horizontal position when the light reaches the detector. This enables the detector to measure the intensity of each individual wavelength. Once the individual wavelengths reach the photomultiplier tube (PMT), it produces an electron that is accelerated and the number of electrons multiplied. This detector produces large signals, large active areas, and fast rise times but the problem is that it requires high voltages and gains instability due to a temperature which causes background radiation.

4.6 X-ray photoelectron spectroscopy (XPS)

XPS is a surface characterization technique developed by Seigbahn in 1960. The technique is used to study surface elements present in the material, together with the nature of chemical bonds that hold these elements together. XPS can successfully detect any element in the periodic table excluding hydrogen and helium [23]. This technique has three basics components that are used to carry out a photoemission experiment (shown in Figure 4.12): (i) an X-ray source with fixed radiation energy, (ii) an electron analyser, this should be able to measure a flux of emitted photoelectrons with specific energies.

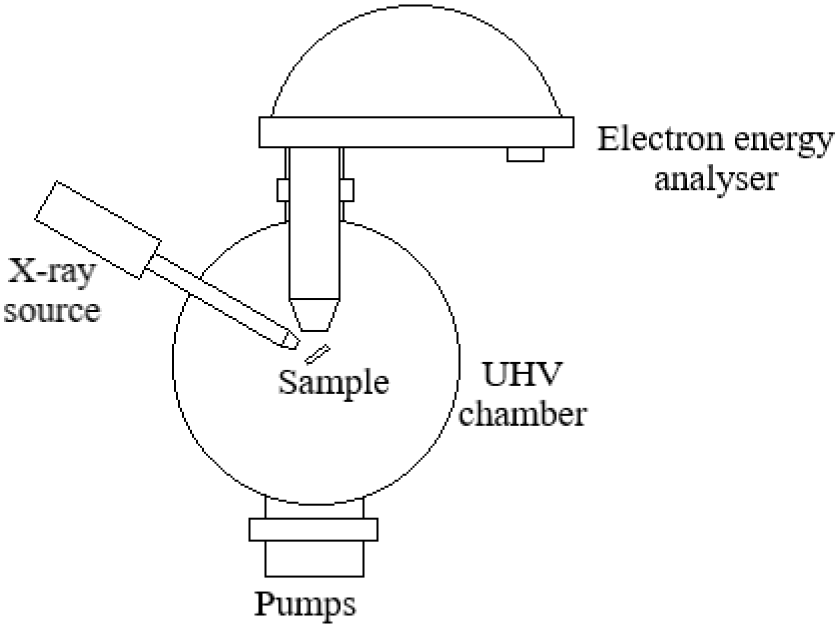

Figure 4.12. Schematic representation of a basic setup in an XPS.

The analyser sorts out the emitted photoelectrons according to their specific kinetic energies. There are many different designs of an electron energy analyser but the preferred option for photoemission experiments is a concentric hemispherical analyser (CHA) which uses an electric field between two hemispherical surfaces to disperse the electrons according to their kinetic energy [24]. (iii) A high vacuum chamber is used to avoid collision of the photoelectrons with gas molecules in the atmosphere. To generate X-rays with fixed radiation energy, a source that gives rise to Mg K_α ($hv =$ 1253.6 eV) and Al K_α ($hv = 1486.6\ eV$) radiations are often used. In Figure 4.13, the sample is bombarded with Al X-rays. The X-rays interact with core shell electrons of different atoms in the sample. Once these electrons around the nucleus have enough energy they escape as photoelectrons with a well-defined kinetic, E_k, given by:

$$E_k = hv - E_b - \Phi \tag{4.5}$$

where hv is the X-ray photon energy, E_b is the electron binding energy, and Φ the work function that is the energy needed for the electron to free itself from the surface. It depends on the spectrometer and the substrate [25]. Photoelectrons coming from dissimilar types of orbitals and atoms or even similar ones in different binding states have binding energies that differ. Equation 4.5 relates the kinetic energy of these photoelectrons with their binding energy.

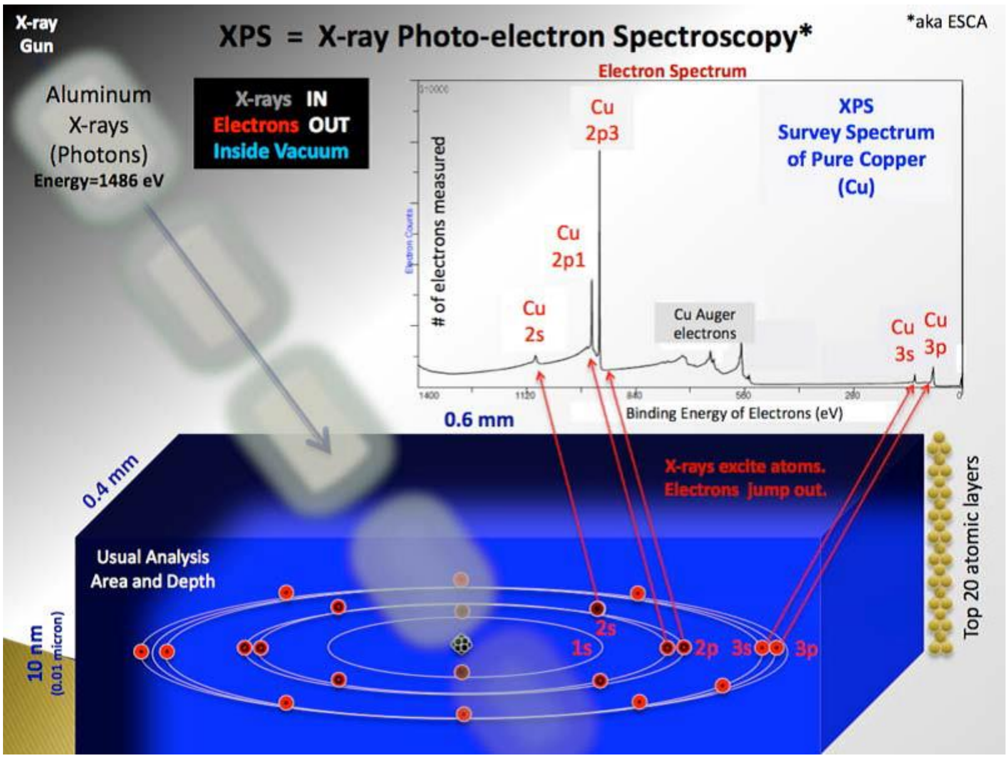

Figure 4.13. Schematic depicting ionization of electron as it pertains to XPS [26].

A typical XPS spectrum is a plot of the number of electrons detected (sometimes per unit time) as a function of the binding energy of the electrons detected. Each element produces a characteristic set of peaks at characteristic binding energy values that directly identify each element that exists in or on the surface of the material being analysed. These characteristic spectral peaks correspond to the electron orbital configuration of the electrons within the atoms, e.g., 1s, 2s, 2p, 3s, etc. The number of detected electrons in each of the characteristic peaks is directly related to the amount of element within the XPS sampling volume.

4.7 Fourier transform infrared spectroscopy (FTIR)

A Fourier-transform infrared (FTIR) spectroscopy uses the interference of radiation between two beams to create an interferogram. The interferogram is a signal that occurs as a result of a difference in the path length between the two beams. There are two parameters, distance, and frequency, that are interconvertible by the mathematical method of Fourier-transformation [27]. The spectrometer was designed to overcome limitations of dispersive instruments, which mainly have a slow scanning process. Thus, a new method was required to measure all the infrared frequencies at the same time, rather than individually. A solution that used a very simple optical device called an interferometer was developed. The interferometer has a unique type of a signal it produces which contains all the infrared frequencies “encoded” into it.

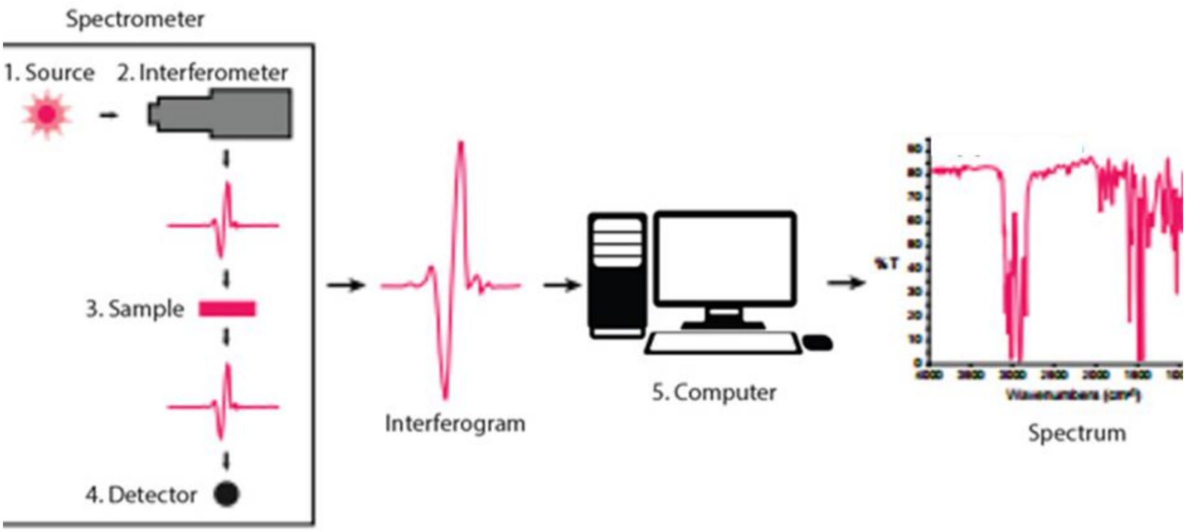

Figure 4.14. Schematic diagram showing a basic setup of FTIR spectroscopy.

The signal can be quickly measured in an order of one second or so. Thus, the time element per sample can be drastically reduced to a few seconds instead of several minutes [28]. In most interferometers, a beam splitter is used to divide the incoming infrared beam into two optical beams. A flat mirror that is fixed in one position reflects one beam, and the other beam is reflected by another flat mirror which has a mechanism that allows it to move a very short distance (typically of few millimetres) away from the beam splitter. These two beams reflect off their respective mirrors and recombine back at the beam splitter.

Since the path length of one mirror is fixed while the other is constantly changing, with the movement of the mirror, the signal which reaches the interferometer is a result of the two beams ‘interfering’ with each other. This results in a signal known as an interferogram. This is a signal that has information about every infrared frequency which comes from the source. This means that by measuring the interferogram one measures all the frequencies simultaneously. Fast measurements are thus ultimately obtained with the use of interferometer. However, it is still impossible to interpret the measured interferometer signal as an analyst would still need a frequency spectrum (a plot of the intensity at each individual frequency) in order to make an identification. Decoding the individual frequencies is accomplished with a well-known mathematical technique called the Fourier transformation. This transformation is performed by the computer which then presents the user with the desired spectral information for analysis.

The normal instrumental process in Figure. 4.14 is a five-step process: (1) the source; with a glowing black-body source that emits infrared radiation. The beam goes through an aperture which controls the amount of energy presented to the sample (and, ultimately, to the detector). (2) The interferometer; ‘spectral encoding’ takes place here as the beam enters the interferometer, bring about an interferogram signal. (3) The sample; depending on the analysis type required, the signal entering the sample compartment is transmitted through or reflected off the surface of the sample. In this compartment, specific frequencies of energy, which are uniquely characteristic of the sample, are absorbed. (4) The detector; the signal goes through the detector that is specially made to measure an interferogram signal for final measurement. (5) The computer; the measured signal is digitized and sent to the computer where the Fourier transformation takes place. The final infrared spectrum is then presented to the user for interpretation and any further manipulation.

The FTIR instrument sends infrared radiation of about 10,000 to 100 cm^{-1} through a sample, with some radiation absorbed and some passed through. The absorbed radiation is converted into rotational and/or vibrational energy by the sample molecules. The resulting signal at the detector presents as a spectrum, typically from 4000 cm^{-1} to 400cm^{-1}, representing a molecular fingerprint of the sample. Each molecule or chemical structure will produce a unique spectral fingerprint, making FTIR analysis a great tool for chemical identification.

4.8 Time-of-Flight Secondary Ion Mass Spectroscopy (ToF-SIMS)

ToF-SIMS is an analytical technique that uses a focused, pulsed particle beam to provide detailed elemental and molecular information about the surface of a sample. ToF mass spectrometry is based on the fact that ions with the same energy but different masses travel with different velocities. SIMS is a very sensitive surface technique because the emitted particles originate from the uppermost one or two atomic layers of a sample. The subsequent time-of-flight mass analysis of the emitted ions provides detailed information on the elemental and molecular composition of the surface.

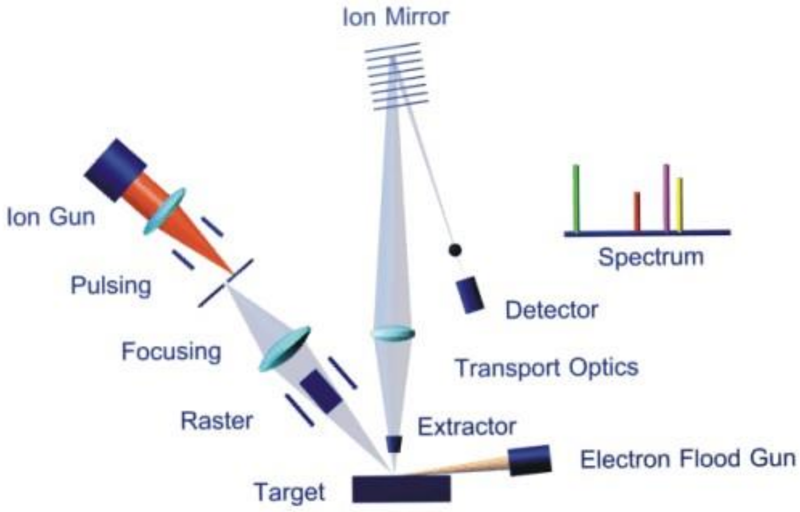

Figure 4.15. Schematic representation of ToF-SIMS instrument [30].

ToF-SIMS instruments typically include these components (Figure 4.15): an ultrahigh vacuum system, which is needed to increase the mean free path of ions liberated in the flight path; a particle gun, that typically uses a Bi^+ source; the flight path, which is either circular in design, using electrostatic analysers to direct the particle beam, or linear using a reflecting mirror; and the mass detector system. A solid surface is bombarded by primary ions of some keV energy. The primary ion energy is then transferred to target atoms *via* atomic collisions and a collision cascade is generated. Part of the energy is transported back to the surface allowing surface atoms and molecular compounds to overcome the surface binding energy. The interaction of the collision cascade with surface molecules is soft enough to allow even large and non-volatile molecules with masses up to 10,000 u to escape without or with little fragmentation [29]. The emitted particles consist of mostly neutrally charged particles, with a small proportion of negatively or positively charged ions. The charged ions are accelerated by an electrostatic field to similar energy. These accelerated ions then reflect off a reflection stage with a single electric field region that reflects the ions to the detector (Figure. 4.16). Ions with lighter mass travel with a higher velocity and reach the detector before heavier ions do. Measuring the flight time for each ion allows the determination of its mass. The pulsed primary ion beam can be fixed to a small spot (microprobe mode) and rastered to determine the lateral distribution of elements and molecules. In this mode of operation lateral resolution of down to 50 nm can be achieved.

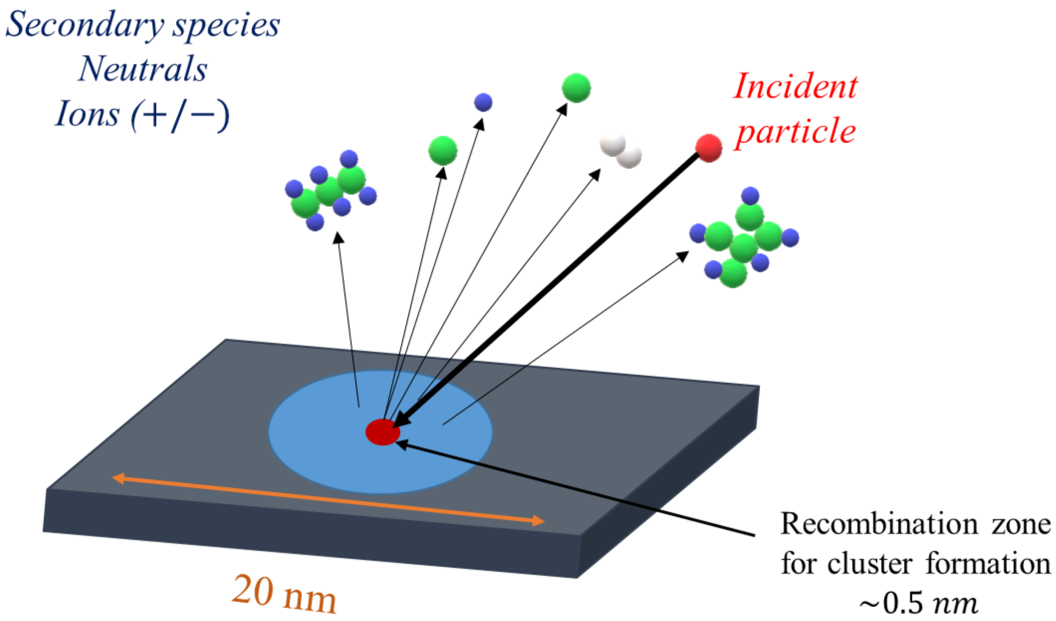

Figure 4.16. Schematic diagram showing secondary ion species [31].

Data obtained from ToF-SIMS is displayed in three modes; mass spectra (showing the number of counted ions of a given mass); ion images (showing where any selected element or isotope is present in the imaged area); depth profiles (showing the count rate for any isotope as a function of time at increasing sputtering depth).

References

[1] E. Willinger, “Fundamentals of X-ray diffraction.” [Online]. Available: http://www.fhiberlin.mpg.de/acnew/department/pages/teaching/pages/teaching__wintersemester__2014_2015/elena_willinger__fundamental_of_x-ray_diffraction__141107.pdf. [Accessed: 06-Jul-2018].

[2] M. T. Felix, W. Friedrich, and P. Knipping, “History of XRD - 2,” 1960.

[3] B. L. Dutrow and C. M. Clark, “X-ray Powder Diffraction (XRD),” *Carleton College*, 2017. [Online]. Available: https://serc.carleton.edu/research_education/geochemsheets/techniques/XRD.html. [Accessed: 11-Jun-2018].

[4] H. Georgia State University, “X-Ray Tube.” [Online]. Available: http://hyperphysics.phy-astr.gsu.edu/hbase/quantum/xtube.html. [Accessed: 11-Jun-2018].

[5] Pd.chem.ucl.ac.uk, “X-ray Filters,” 2014. [Online]. Available: http://pd.chem.ucl.ac.uk/pdnn/inst1/filters.htm. [Accessed: 11-Jun-2018].

[6] M. Within, “B.D. Cullity, Elements of X-ray Diffraction, 2nd ed., AddisonWesley, London, 1978.”

[7] “Bragg’s Law.” [Online]. Available: http://pd.chem.ucl.ac.uk/pdnn/powintro/braggs.htm. [Accessed: 12-Jun-2018].

[8] W. L. Bragg, S. William, and H. Bragg, “Bragg’s law,” 1913. [Online]. Available: http://pd.chem.ucl.ac.uk/pdnn/powintro/braggs.htm. [Accessed: 12-Jun-2018].

[9] R. Erni, M. D. Rossell, C. Kisielowski, and U. Dahmen, “Atomic-Resolution Imaging with a Sub-50-pm Electron Probe,” *Phys. Rev. Lett.*, vol. 102, no. 9, p. 096101, Mar. 2009.

[10] NanoScience Instruments, “How does Scanning Electron Microscopy work?,” 2016. [Online]. Available: http://www.nanoscience.com/technology/sem-technology/.

[11] D. S. Su, “Scanning electron microscopy (SEM),” pp. 1–46, 2010.

[12] Hapic, “Global Scanning Electron Microscope (SEM) Market Professional Survey Report 2017 - Haptic,” 2018. [Online]. Available: https://www.haptic.ro/product/global-scanning-electron-microscope-sem-market-professional-survey-report-2017/. [Accessed: 20-Jun-2018].

[13] T. B. Picture, “Scanning Electron Microscopy Primer,” *Cities*, pp. 1–29, 2007.

[14] University of Glasgow, “University of Glasgow - Schools - School of Geographical and Earth Sciences - Research and Impact - Research Facilities - ISAAC : Imaging Spectroscopy and Analysis Centre - Services - Scanning Electron Microsco py.” [Online]. Available: https://www.gla.ac.uk/schools/ges/researchandimpact/researchfacilities/isaac/services/scanningelectronmicroscopy/. [Accessed: 20-Jun-2018].

[15] B. Hafner, “Energy dispersive spectroscopy on the SEM: a primer.” Characterization Facility, University of Minnesota, pp. 1–26, 2006.

[16] D. S. D. Bobji, M.S., Nitin Kumar, Uttiya Mukherjee, “MATERIAL CHARACTERISATION ‘ TRANSMISSION ELECTRON MICROSCOPE ,’” no. 09266.

[17] S. Bradbury, D. C. Joy, and B. J. Ford, “Transmission electron microscope.” [Online]. Available: https://www.britannica.com/technology/transmission-electron-microscope. [Accessed: 16-Jul-2018].

[18] De Histology, “Electron Microscopy,” 2011. [Online]. Available: http://dehistology.blogspot.com/2011/06/electron-microscopy.html. [Accessed: 16-Jul-2018].

[19] “Structural Tools in Nanochemistry,” no. 2, p. 1997, 1997.

[20] “UV-Visible Spectroscopy,” *MSU Chemistry*, 2015. [Online]. Available: https://www2.chemistry.msu.edu/faculty/reusch/virttxtjml/spectrpy/uv-vis/uvspec.htm. [Accessed: 09-Jul-2018].

[21] A. R. Barron, “Photoluminescence Spectroscopy and its Applications,” *Connexions Modul.*, pp. 1–11, 2011.

[22] Renishaw, “Photoluminescence explained,” *Renishaw*, 2017. [Online]. Available: http://www.renishaw.com/media/img/en/50e033cc197a416db28909dc584e38a1.jpg%0Ahttp://www.renishaw.com/en/photoluminescence-explained--25809. [Accessed: 14-Jul-2018].

[23] “The Actinide Research Quarterly: Winter 1996.” [Online]. Available: http://www.lanl.gov/orgs/nmt/nmtdo/AQarchive/96winter/HGMS.html. [Accessed: 10-Jul-2018].

[24] “Photoelectron Spectroscopy.” [Online]. Available: http://www.chem.qmul.ac.uk/surfaces/scc/scat5_3.htm. [Accessed: 11-Jul-2018].

[25] P. M. Claesson, A. van der Wal, and A. Fogden, “New Techniques for Optimization of Particulate Cleaning,” *Handb. Cleaning/Decontamination Surfaces*, pp. 885–927, Jan. 2007.

[26] Bvcrist, “File_XPS PHYSICS,” 2010. [Online]. Available: https://commons.wikimedia.org/wiki/File:XPS_PHYSICS.png. [Accessed: 11-Jul-2018].

[27] B. H. Stuart, *Infrared Spectroscopy: Fundamentals and Applications*, vol. 8. 2004.

[28] M. A. Ganzoury, N. K. Allam, T. Nicolet, and C. All, “Introduction to Fourier Transform Infrared Spectrometry,” *Renew. Sustain. Energy Rev.*, vol. 50, pp. 1–8, 2015.

[29] “TOF-SIMS (Time of flight secondary ion mass spectrometry) technique for surface analysis.” [Online]. Available: https://www.iontof.com/tof-sims-secondary-ion-mass-spectrometry.html. [Accessed: 22-Jul-2018].

[30] “How_does_TOF_SIMS_work.” [Online]. Available: http://www2.fkf.mpg.de/ga/machines/sims/How_does_TOF_SIMS_work.html. [Accessed: 22-Jul-2018].

[31] David W. Mogk, “Time-of-Flight Secondary Ion Mass Spectrometry (TOF-SIMS),” *Geochemical Instrumentation and Analysis*. [Online]. Available: http://www.eag.com/time-of-flight-secondary-ion-mass-spectrometry-tof-sims/.

[Accessed: 23-Jul-2018].

CHAPTER 5

Quantum confinement effect: structural and optical properties of CdS NPs prepared with water as solvent.

5.1 Introduction

Cadmium sulfide (CdS) is a water-insoluble group II-VI semiconductor, which can be dissolved with dilute mineral acids, like sulfuric acid, hydrochloric acid, and nitric acid. It is known to crystallize in three crystal phases: wurtzite, zinc blende, and high-pressure rock salt. The wurtzite phase has the highest stability amongst the three structures. This phase has been observed and reported in both bulk and nanocrystalline CdS, whilst its cubic and rock-salt counterparts were only observed in nanocrystalline CdS [1][2]. During size reduction of bulk CdS particles to the nanoscale, there are deviations from its usual chemical, structural and physical properties. The quantum confinement effect also affects other properties of CdS NPs such as the melting point, electronic absorption spectra, crystal structure, and band gap energy to name a few [3][4]. The large CdS band gap energy of 2.42 eV (bulk) at room temperature allows for applications in optoelectronics, photonics, photovoltaics, and photocatalysis. The nanocrystalline structure of nanomaterials plays a critical role in determining their electronic properties. It has been reported that the reaction conditions during the preparation of this material can be influential in the resultant crystal structure upon size reduction, [5][6]. In this work CdS NPs have been synthesized using a chemical precipitation method. Crystal size growth is controlled by varying the number of TG molecules (i.e concentration) during the nucleation process.

5.2 Experimental

Sample preparation

CdS NPs were synthesized with a wet chemical synthesis technique of chemical precipitation using TG ($C_3H_8O_2S$) as a capping agent to control the particle size. All the reactions were carried out at room temperature and standard atmospheric pressure. Cadmium chloride ($CdCl_2$) and sodium sulfide (Na_2S) were used as starting materials, acting as a source of Cd^{2+} and S^{2-} ions respectively. Double distilled water was added as a solvent with varying TG concentrations to control the growth. Initially, 0.1 mole (M) $CdCl_2$ and 0.1 M Na_2S were added in 50 mL of double distilled water separately with vigorous magnetic stirring [7]. The required amount (discussed below) of TG was added to the Na_2S solution while stirring. The samples were stirred until the powder completely dissolved into the solvent. The Na_2S-TG solution was then added dropwise to the $CdCl_2$ while constantly stirring using a magnetic stirrer. As particle growth started with the formation of precipitates, the colour of the solution changed from colourless to orange for the 0.0 mL TG (S0) sample, yellow for the 0.1 mL TG (S1) sample, lemon-yellow for the 0.2 mL TG (S2) sample, lemon for the 0.3 mL TG (S3) sample, and whitish-lemon for the 0.8 mL TG (S5) sample. The five CdS precipitates with varying TG concentrations were washed with ethanol several times to remove impurities and unreacted reactants. The precipitate was then collected by centrifugation for 5 minutes at 5000 rpm and then dried in an air oven for 10 hrs at 50 ℃. After 10 hrs in the oven, the quantity of the powder decreased significantly suggesting the removal of impurities and large quantities of water through evaporation. The S3 sample was further annealed to observe and study the effects of change in temperature on crystallinity. Annealing was carried in an argon-rich atmosphere for 2 hrs at 200℃ (A200), 350℃ (A350), 500℃ (A500) and 700 ℃ (A700) respectively.

Characterization

Structural properties of the CdS NPs were recorded and analysed using a Bruker D8 Advanced X-ray diffractometer (XRD) over the range of $20° < 2\theta < 60°$ equipped with monochromatic $CuK\alpha$ radiation of $\lambda = 1.54056$ Å. To study the morphology, a Jeol JSM-7800F field emission scanning electron microscope (FE-SEM) fitted with Oxford Aztec 350 X-Max80 energy dispersive X-ray spectroscopy (EDS) were employed. While the photoluminescence (PL) spectra were measured using a PL laser system equipped with a 325 nm HeCd gas laser to excite the material at room temperature, with a spectrometer, a photomultiplier tube (PMT) detector, and a lock-in amplifier. For UV-Vis absorption, the dried powders were dispersed in dimethyl sulphoxide before collection of data with Lambda 950 UV-Vis spectrometer in the wavelength range of 250-700 nm. The molecular structure of the samples were analysed with a Nicolet 6700 Fourier transform infrared (FTIR) spectroscopy. The chemical states were studied with a PHY 5400 X-ray photoelectron spectroscopy (XPS).

5.3 Results and Discussions

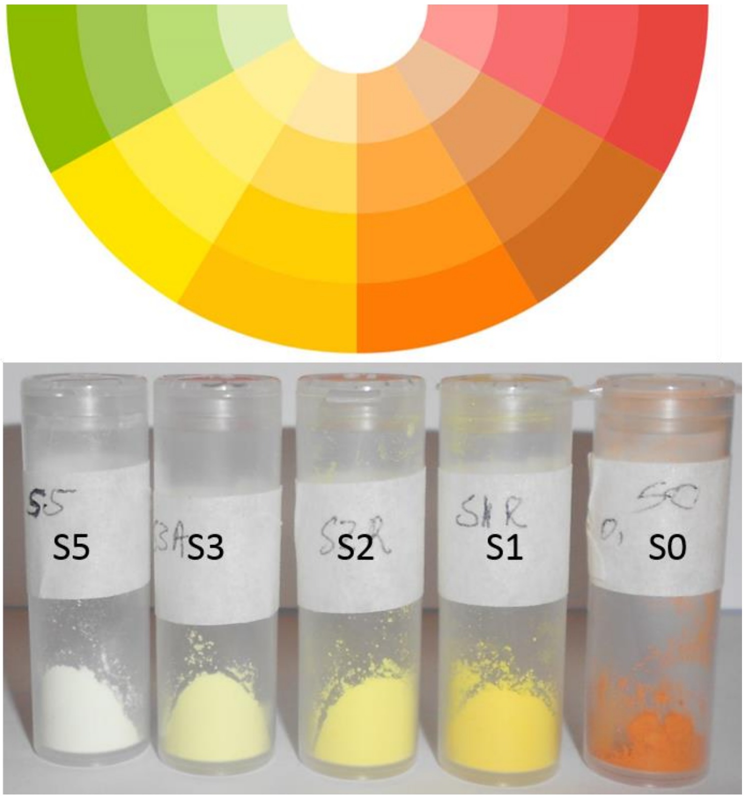

Figure 5.1. CdS NPs with different capping agent concentrations resulting in varying colours: S0 (no TG), S1 (0.1 mL), S2 (0.2 mL), S3 (0.3 mL) and S5 (0.8 mL). A colour wheel is added as a guide to the eye.

The NPs synthesized *via* the precipitation method [1] displayed an observable colour change, which was indicative of the formation of CdS NPs. The colour of the precipitate varied with the concentration of the capping agent (TG) which was used to control the NP size. The sample labelled S0 has no capping agent added and it displayed an orange colour (S0) as shown in Figure 5.1. The addition of 0.1 mL of TG in the experiment caused colour change from transparent to yellow (S1). Since these NPs absorb and emit photons at different wavelengths depending on their size, it was observed that the colour of the prepared CdS samples changed as more TG was introduced into the solution. The smallest NPs that was formed (and will be discussed later) was for sample S5 with a TG concentration of 0.8 mL and the resultant powder displayed a whitish-lemon colour. This served as a preliminary, visual confirmation of the shift in absorption edge as a result of the quantum confinement/size effect caused by reducing particle size [8].

Structure and morphology analysis

5.3.1 XRD

5.3.1.1 Crystal phases

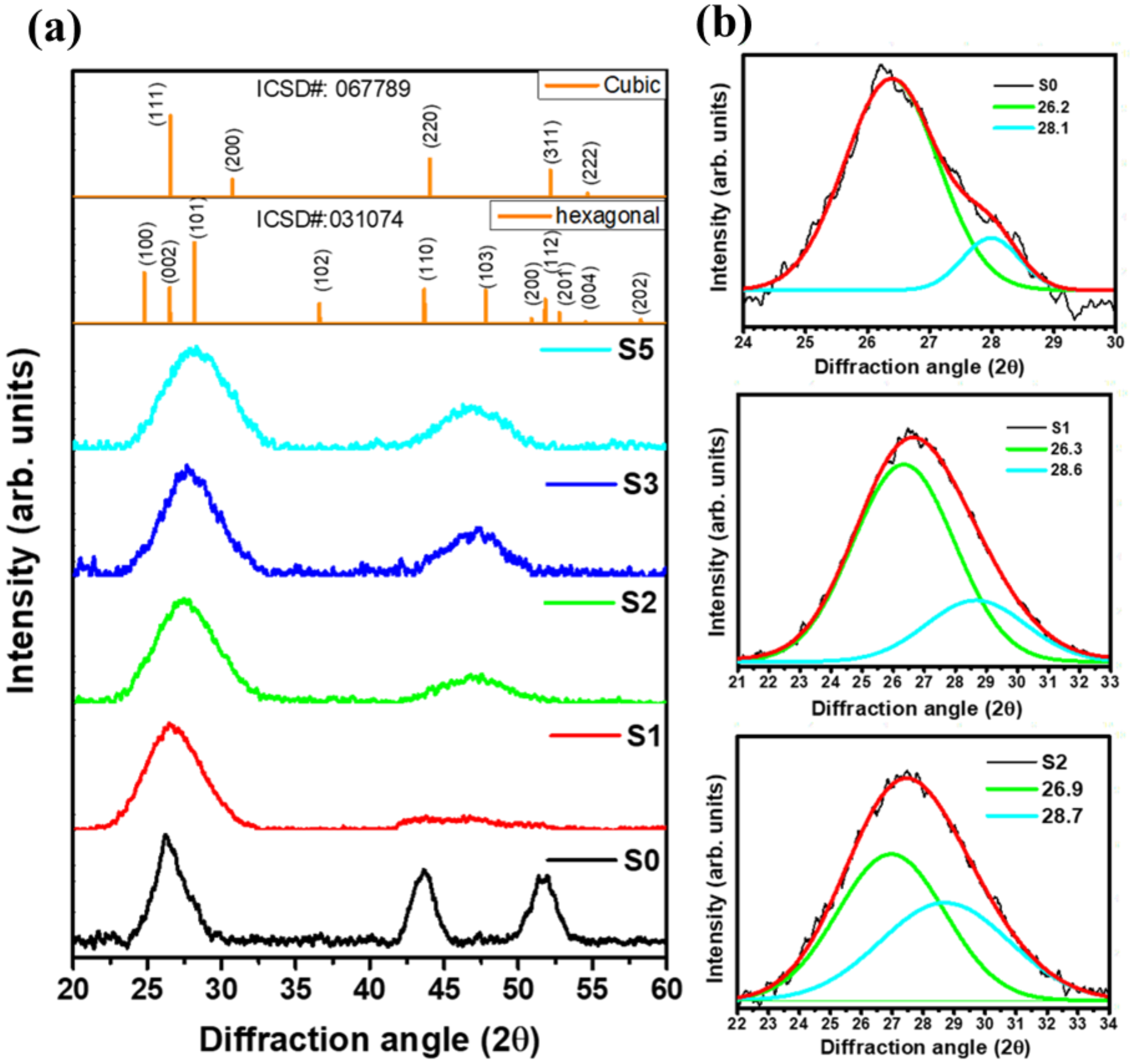

Figure 5.2. (a) The XRD patterns of the as-prepared CdS NPs with different sizes: S0, S1, S2, S3, and S5. **(b)** And the resolution of the 28° peak.

XRD is an effective technique for determining the crystallinity and the crystalline size of materials. In this section the as-prepared CdS NPs: S0, S1, S2, S3, and S5 were further investigated with XRD. S3 was also annealed to investigate the effects that annealing temperatures may have on the crystalline structure of the sample. Figure 5.2 (a) shows the X-ray diffraction pattern of the as-prepared CdS NPs. The observed scattering angle (2θ) values of the XRD peaks for the first three samples (S0, S1, and S2) are 26.3°, 43.7°, and 51.7°, corresponding to diffraction from planes (111), (220), and (311) [ICSD#: 067789] respectively. Bandaranayake *et al* [5] reported that this is indicative of a cubic zinc blend CdS rather than of amorphous CdS NPs, which only have a single very broad neighbour peak near the (111) line. However, after resolving the broad peaks into their constituent components, overlapping peaks showed shoulders around 28° (i.e Figure 5.2 (b)) and 47° corresponding to the hexagonal wurtzite phase (101) and (103) planes respectively. Thus the as-prepared CdS samples exhibit a mixed-phase of both zinc blende cubic and wurtzite hexagonal phase [10].

When compared to the standard [ICSD#: 031074] [11][12], the XRD patterns of samples S3 and S5 have a hexagonal CdS structure which is indicated by the presence of the (100), (002), and (101) peaks between 20° and 30°. However, the assignment of CdS phases has proven to be quite challenging since for the hexagonal phase preferred orientation, the (002) and the cubic (111) lines coincide within a difference of only 1% [13]. Thus, the existence of the cubical zinc blende phase cannot be ruled out as there are also weak overlapping peaks around 27° (111) and 44° (220) present in the XRD pattern.

5.3.1.2 Crystallite size and surface stress

The structural stability of CdS can also be qualitatively deduced from the XRD patterns. It is observed that the peak centered around 27° broadens when adding more of the TG capping agent, i.e. from sample S0 to sample S5. This increase in the peak's full-width half maximum (FWHM) is a result of a decrease in particle size (which will be shown later) since the TG concentration increases and it is known that increasing NP surfactant concentration decreases particle size. As such, Debye Scherer-broadening is observed for this peak. In single-crystallite samples, crystal size relates to the particle size whereas, in polycrystalline samples, particles are larger than their crystalline constituents [14]. In single crystal samples, the crystallite size is calculated using the Debye Scherer formula,

$$D = 0.9\lambda/\beta cos\theta \tag{5.1}$$

D is the crystallite size, λ is the X-rays' wavelength of the $CuK_{\propto}$ line (1.54 A°), θ is the diffraction angle, and β is the full-width at half-maximum (FWHM) of the diffraction peak in radians [15]. The particle sizes for S3 and S5 are 3.0 and 2.95 nm respectively. The approximation of the mean crystallite size was not possible for S0, S1, and S2 due to the peak overlap as well as the presence of a mixture of cubic and hexagonal phases as discussed earlier.

From Figure 5.2 it is observed that the particle size decreases with increasing TG concentration. This is apparent in the increasing broadness of the peak centred between 25° and 30° from S0 to S5 confirming that the crystallites are indeed nano-sized. There is also an observed shift in the peak position to higher angles from S0 to S5. This is attributed to the strain effect that is associated with the quantum confinement effect [16]. Surface stress is directly related to the surface energy [17] which is known to increase with decreasing particle size.

5.3.1.3 Influence of annealing temperature on the crystal phase.

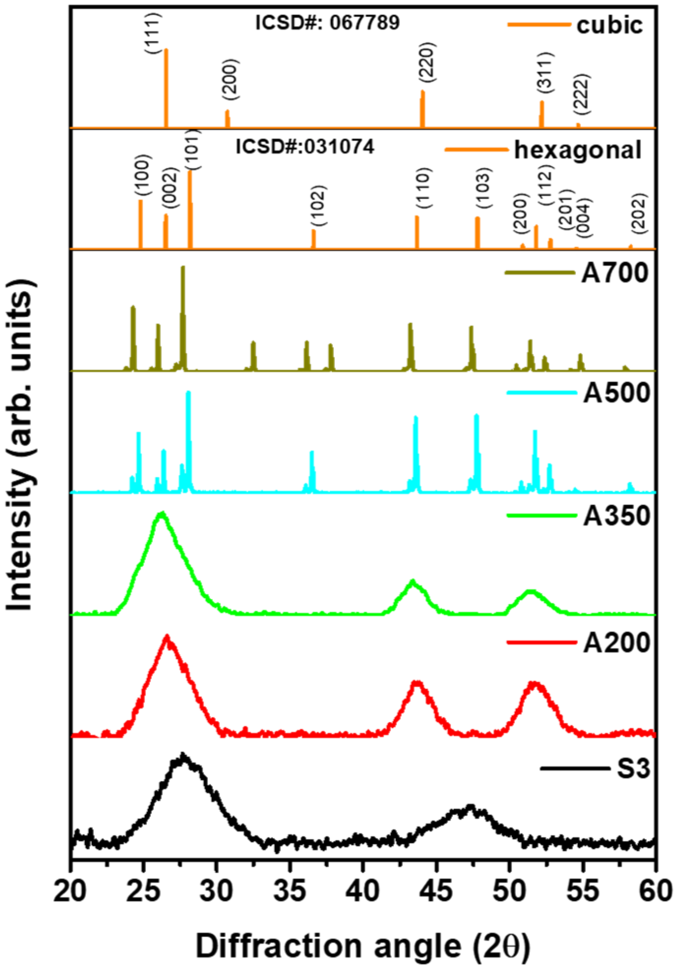

Figure 5.3. XRD patterns of the S3 sample after annealing at a different temperature: A200, A350, A500, and A700.

Annealing temperature effects on the S3 structure are shown in the XRD pattern of Figure 5.3. The effects discussed here for sample *S3* are expected to be the same for all the other CdS samples. It was observed that as the annealing temperature increases, a shift in the peak position to lower diffraction angles occurred, which indicates a reversal of the quantum confinement effect.

The main broad peak centred on 26° splits into three peaks at 500 ℃ attesting to improved crystallinity. The reduced peak FWHM indicates an increase in particle size. Since an increase in particle size is known to reduce the surface energy [18] this will have the effect of countering the above mentioned-shift to lower angles in this case. Annealing at 350 ℃ and temperatures below this show a cubical zinc blende phase compared to the as-prepared S3 NPs. This is met by a phase transformation at temperatures above 350 ℃ to the preferable wurtzite hexagonal phase [19]. Thus the particle size of CdS NPs can be controlled with either a capping agent, the annealing temperature, or the combination of both. With the latter two having the advantage of enhanced crystallinity of the particles. Reducing the NP size with TG leads to enhanced surface energy as a consequence of quantum confinement effect. However, this decrease can be countered by annealing at temperatures above 350 ℃, countering the quantum confinement effect and enhancing the crystallinity of material through sintering.

5.3.2 SEM

The scanning electron microscope images in Figure 5.4 show micrographs of CdS NPs of different sizes taken with similar magnifications (10 000). The images show highly agglomerated NPs. This is similar to what is observed in the literature for as-prepared CdS NPs [20][21]. Particle agglomeration is influenced by a number of factors, including properties of the medium that the particles are suspended in [22]. Large concentrations of the capping agent slow down the reaction and precipitation process by making a compact shell/layer over the surface of the as-grown sample, which results in the formation of smaller NPs on increasing the capping agent concentration [1]. The high surface area to volume ratio resulting from the small NPs provides very high surface energy. To reduce and minimize the surface energy, the NPs agglomerate. Uncontrolled agglomeration of NPs may occur due to Van der Waals weak forces between particles [18]. By annealing the NPs at relatively high temperatures, the TG molecules start desorbing from the CdS surface. This is also shown in FTIR spectra (Figure 5.15) by the decrease in the intensity of the organic molecules at temperatures approaching 350 ℃ and their complete disappearance above this temperature. The removal of these molecules leaves dangling bonds on the NP surface which are highly reactive and lead to particle growth through sintering. Sintering [23][24][25][26] is understood in terms of the Gibbs Thompson relation.

Due to the large chemical potential, small particles grow to become larger particles with lower chemical potential. The driving force is the reduction of the total surface energy of the system [27]. This is observed in the SEM images of Figure 5.5 which show the growth in particles from much agglomerated small particles (on the nanoscale) in Figure 5.5(a) to very large particles in Figure 5.5(d) with apparently smooth surfaces. Thus, there is a relatively large change in the particle’s morphologies as the annealing temperature increases (Figures 5.5(b) to (c)) and it is in this regime where phase transformation takes place.

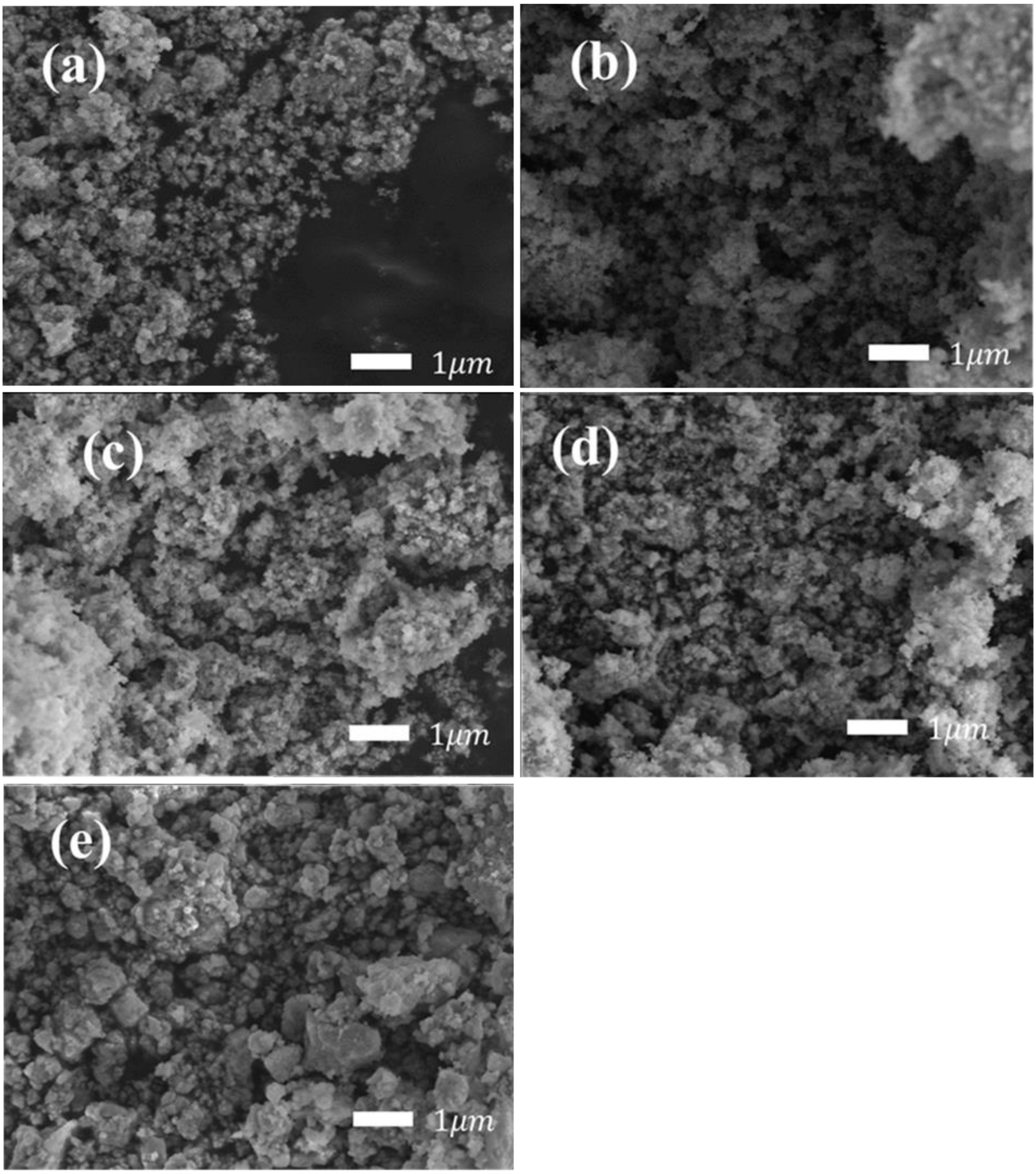

Figure 5.4. SEM images of as-prepared CdS NPs varying according TG concentration (a) S0, (b) S1, (c) S2, (d) S3, and (e) S5.

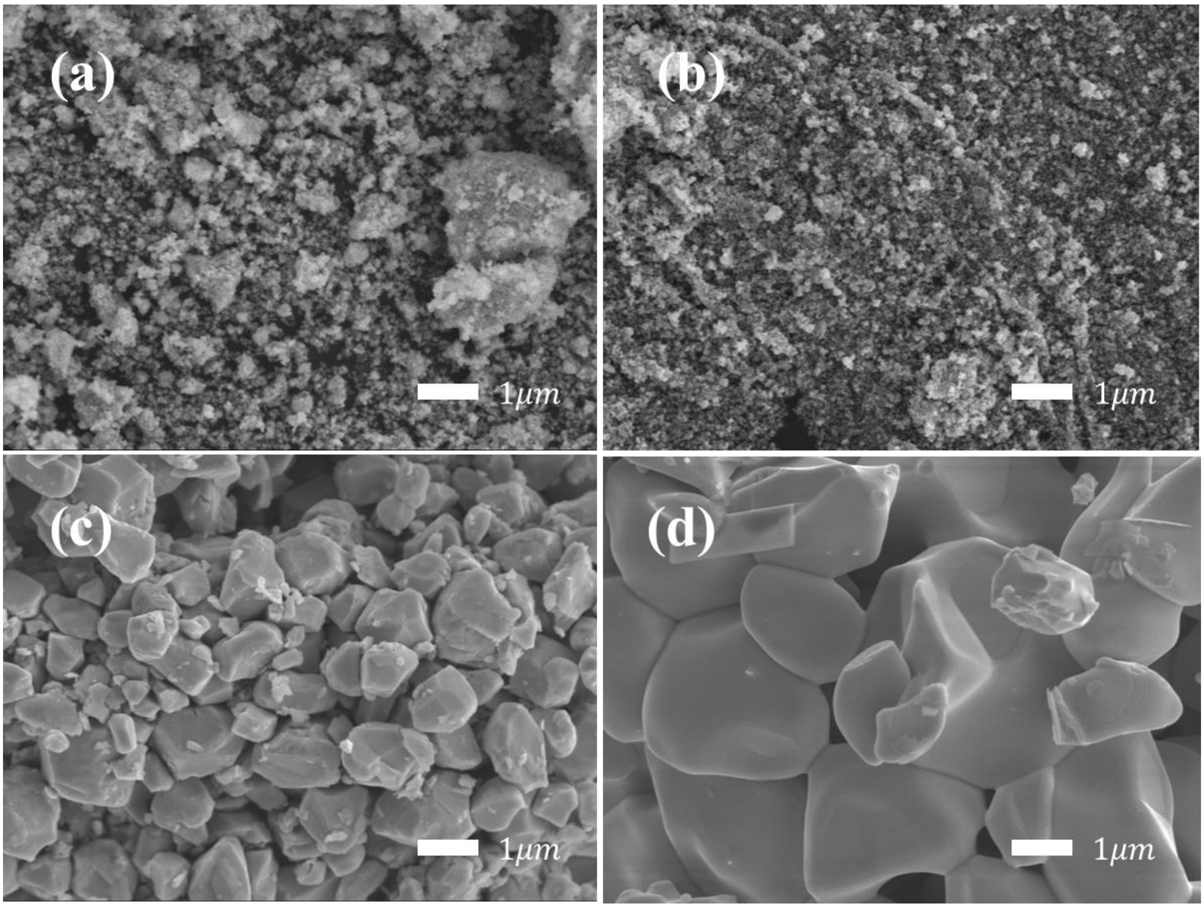

Figure 5.5. SEM images of annealed CdS samples at (a) A200, (b) A350, (c) A500 and (d) A700.

5.3.3 EDS

Energy dispersive X-ray spectroscopy was employed to investigate the elemental composition (%) of all elements contained in the as-prepared CdS samples and the effect of varying the annealing temperatures was studied. Figure 5.6 shows the elemental composition of the as-prepared samples, and the annealing effect is shown in Figure 5.7. Present constituents consist of Cd, S, O, C, and Cl in all samples. The Cl is from the unreacted $CdCl_2$ starting material, while O and C are from both TG ($C_3H_8O_2S$) and the atmosphere. On the other hand, the presence of S originates from both the sulfur source (Na_2S) and the capping agent ($C_3H_8O_2S$), these are differentiated later in the XPS results. The elemental composition (%) ratio of sulfur to cadmium (S/Cd) showed an increasing trend of 0.24, 0.24, 0.27, 0.28, and 0.31 for S0, S1, S2, S3, and S5 respectively indicating an increase in the atomic composition (%) of S relative to Cd, as expected since this also corresponds to the increasing TG concentration associated with these samples, respectively.

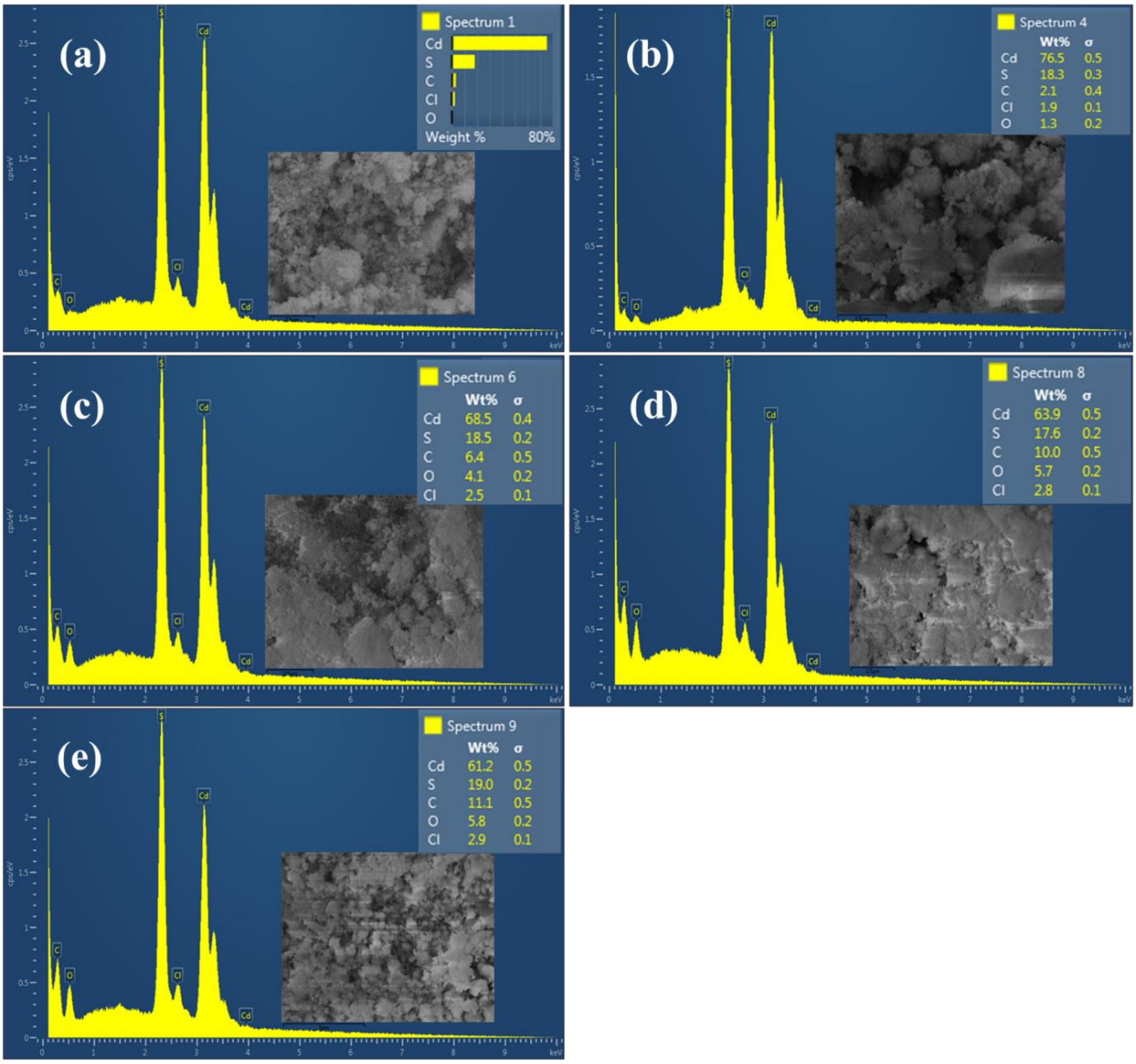

Spectrum 4

	Wt%	σ
Cd	76.5	0.5
S	18.3	0.3
C	2.1	0.4
Cl	1.9	0.1
O	1.3	0.2

Spectrum 6

	Wt%	σ
Cd	68.5	0.4
S	18.5	0.2
C	6.4	0.5
O	4.1	0.2
Cl	2.5	0.1

Spectrum 8

	Wt%	σ
Cd	63.9	0.5
S	17.6	0.2
C	10.0	0.5
O	5.7	0.2
Cl	2.8	0.1

Spectrum 9

	Wt%	σ
Cd	61.2	0.5
S	19.0	0.2
C	11.1	0.5
O	5.8	0.2
Cl	2.9	0.1

Figure 5.6. EDS spectra of the as-prepared CdS NPs of varying size with TG concentration (a) S0, (b) S1, (c) S2, (d) S3, and (e) S5. The S, C, and O peaks all increase with increasing TG concentration.

Annealing of the S3 sample resulted in a decrease in this elemental composition (%) of S as follows: 0.28, 0.26, and 0.25 for S3, A200, and A700 respectively. The EDS results showed an increase in S concentration with increasing TG concentration while annealing temperature decrease S content. This is so since, some of the surface capping TG molecules are easily removed with increasing temperature.

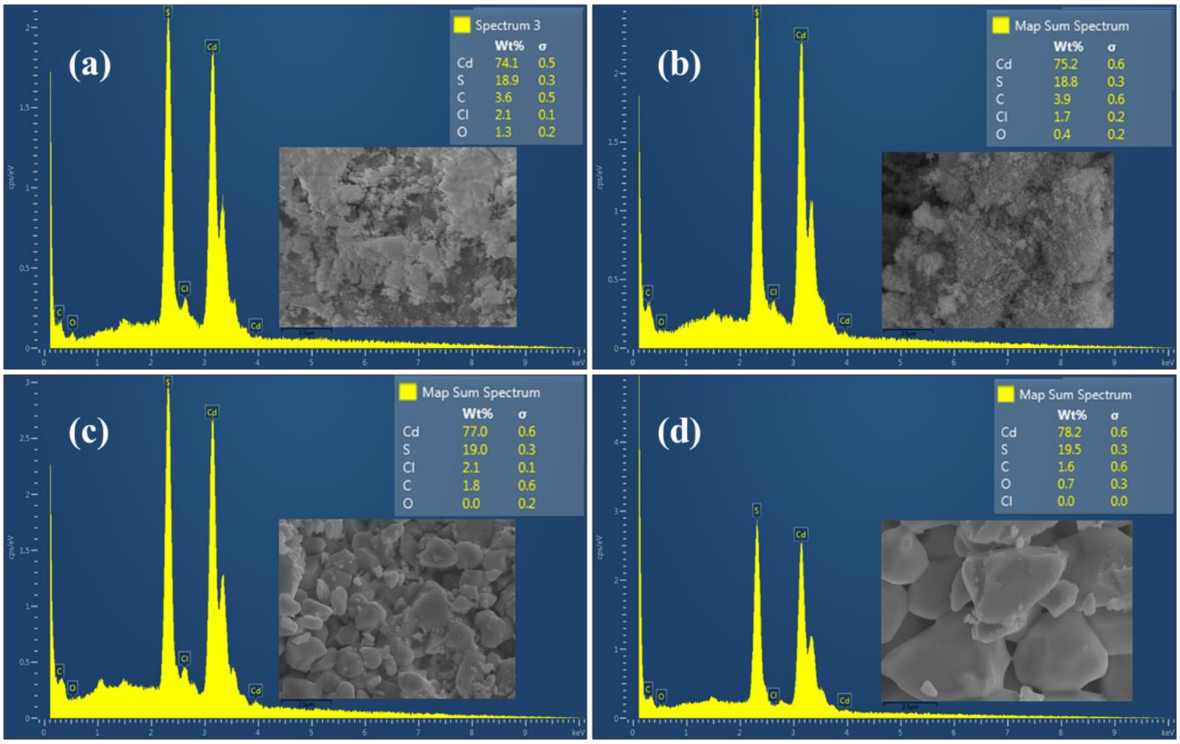

Spectrum 3

	Wt%	σ
Cd	74.1	0.5
S	18.9	0.3
C	3.6	0.5
Cl	2.1	0.1
O	1.3	0.2

Map Sum Spectrum

	Wt%	σ
Cd	75.2	0.6
S	18.8	0.3
C	3.9	0.6
Cl	1.7	0.2
O	0.4	0.2

Map Sum Spectrum

	Wt%	σ
Cd	77.0	0.6
S	19.0	0.3
Cl	2.1	0.1
C	1.8	0.6
O	0.0	0.2

Map Sum Spectrum

	Wt%	σ
Cd	78.2	0.6
S	19.5	0.3
C	1.6	0.6
O	0.7	0.3
Cl	0.0	0.0

Figure 5.7. EDS spectra of the annealed CdS samples at (a) A200, (b) A350 (c) A500 and (d) A700.

5.3.4 TEM

The agglomerates sizes are reduced as the capping agent concentration increases (Figures 5.8(a) to 5.8(e)) resulting in an improved NP size distribution. Figure 5.9 shows the particle distribution function of the NPs with average particle sizes of S0, S1, S2, S3, and S5 listed in table 5.1.

Figure 5.10 shows TEM images of the S3 sample annealed at different temperatures. At low temperatures, the NPs are still agglomerated with boundaries that are not well defined. An increase in particle size is observed for the sample annealed at temperatures higher than 350°C compared to when annealed at lower temperatures (Figure 5.10(c)).

At the transformation phase, the particles sinter into spherically shaped particles with well-defined boundaries. Increasing the annealing temperature not only changes the morphology but also the size distribution of the NPs. Figure 5.11 shows the average particle size for the S3 sample varying with increasing annealing temperatures. It is clear that the sintered particles have grown in size.

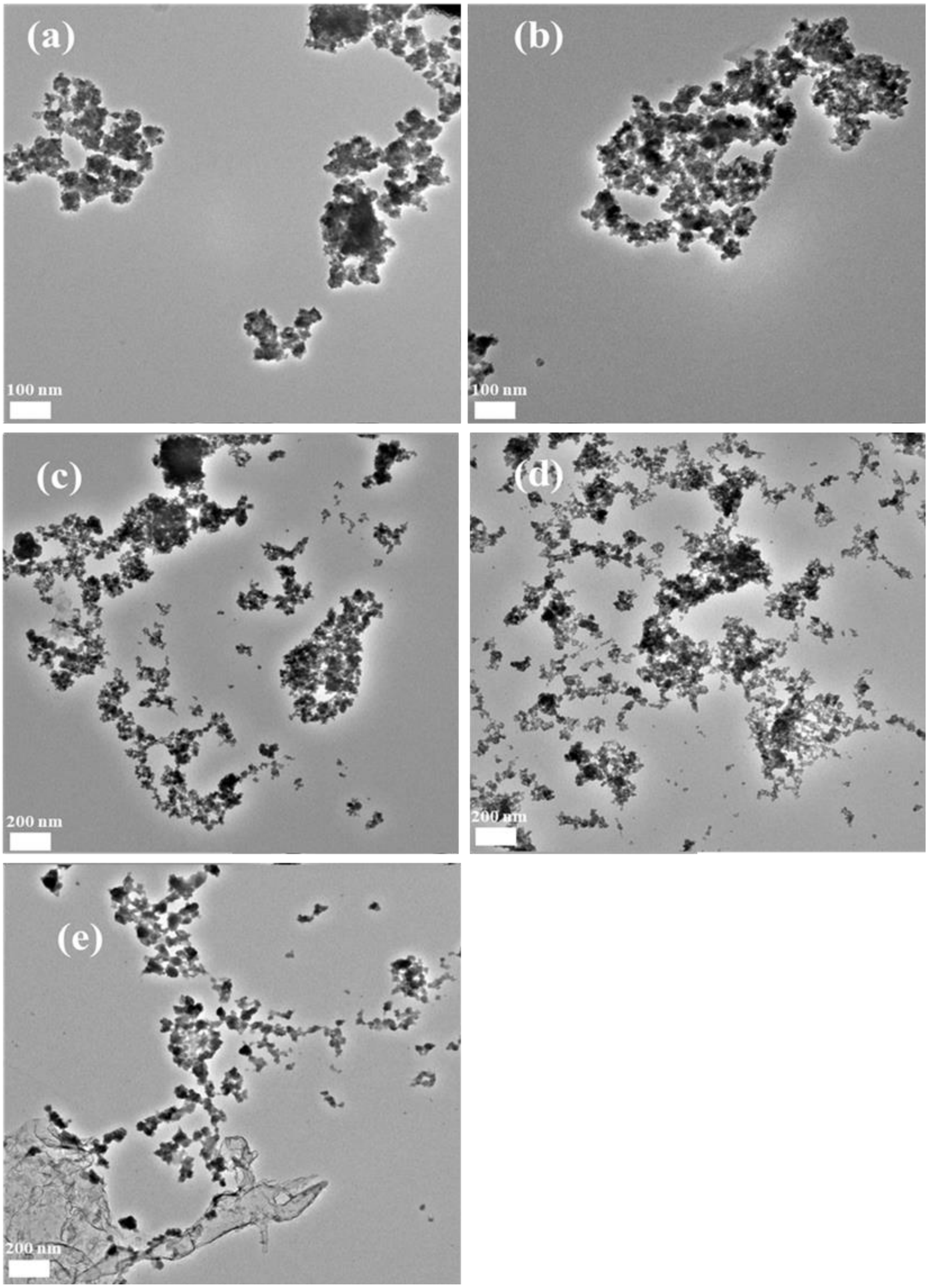

Figure 5.8. TEM images of CdS NPs with varying TG concentrations: (a) S0, (b) S1, (c) S2, (d) S3, and (e) S5.

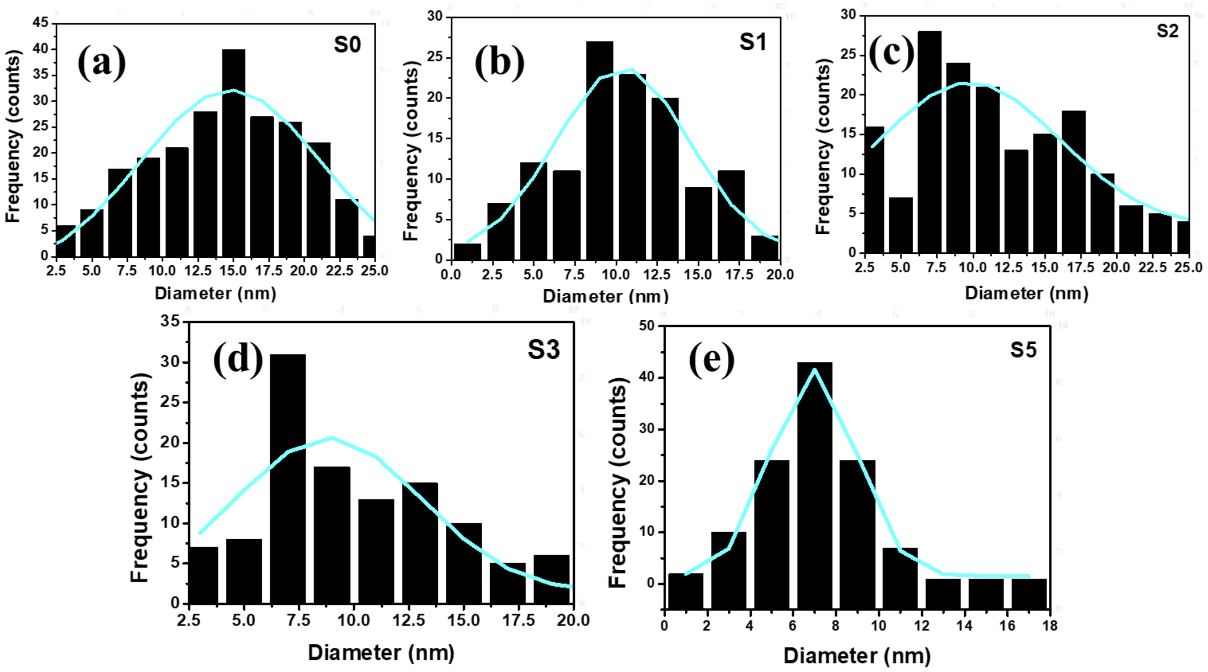

Figure 5.9. Particle distribution function with the corresponding Gaussian curve fitting for CdS samples varying in TG concentration; (a) S0, (b) S1, (c) S2, (d) S3, and (e) S5.

The average particle size for samples; A350, A500, and A700 are shown in table 5.1. The table shows a decreasing particle size from sample S0 to S5, this is due to increasing concentration of TG as previously discussed. Upon annealing the particle size of S3 first decreases at A350. This means the particles at this temperature and below become even finer with annealing. There is a relatively large increase in the particle size after the transformation phase (A350) which results from the decrease in the FWHM with increased crystallinity (Figure 5.3).

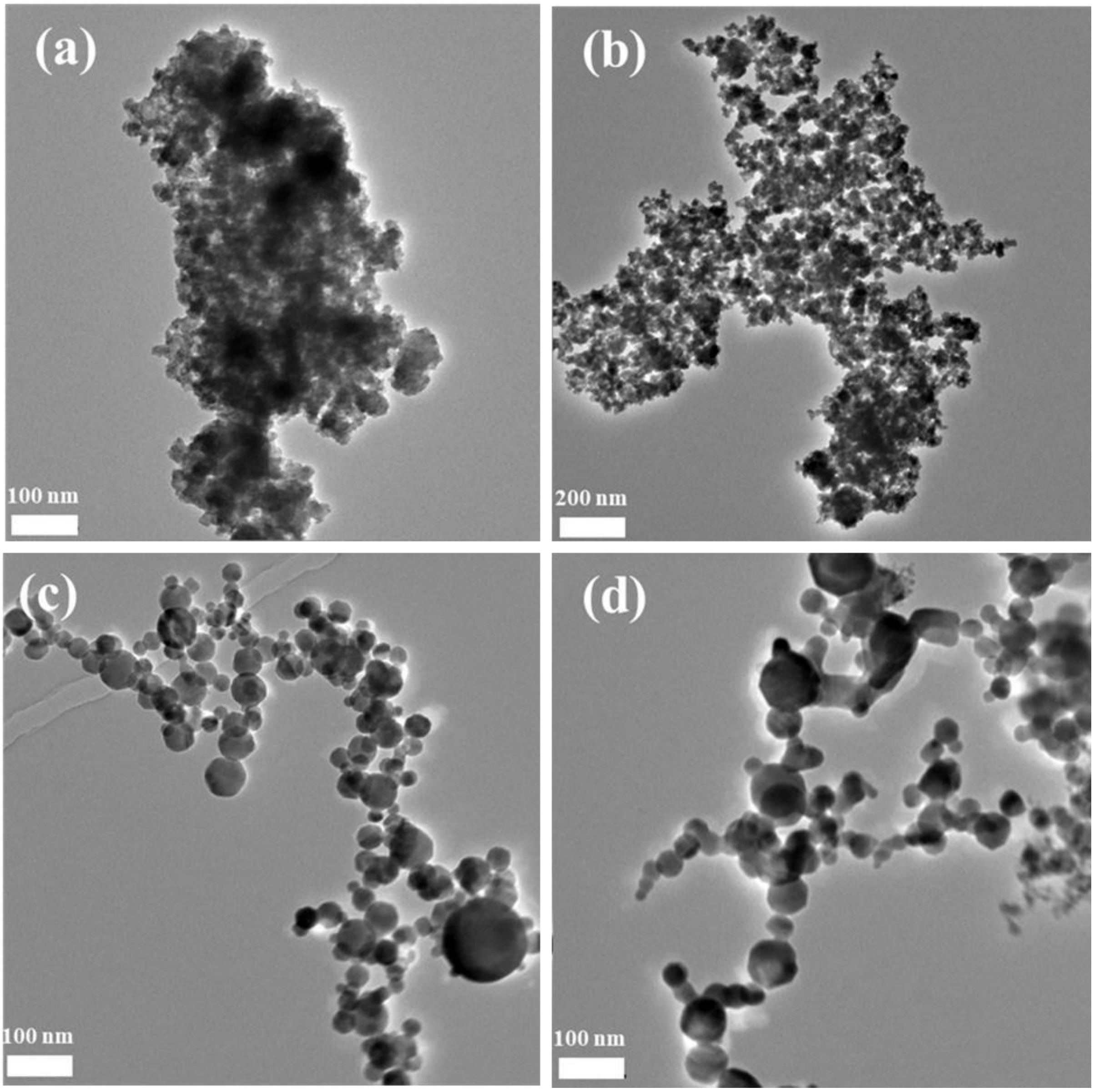

Figure 5.10. TEM images of S3 NPs after annealed at different temperatures (a) A200, (b) A350, (c) A500 and (d) A700.

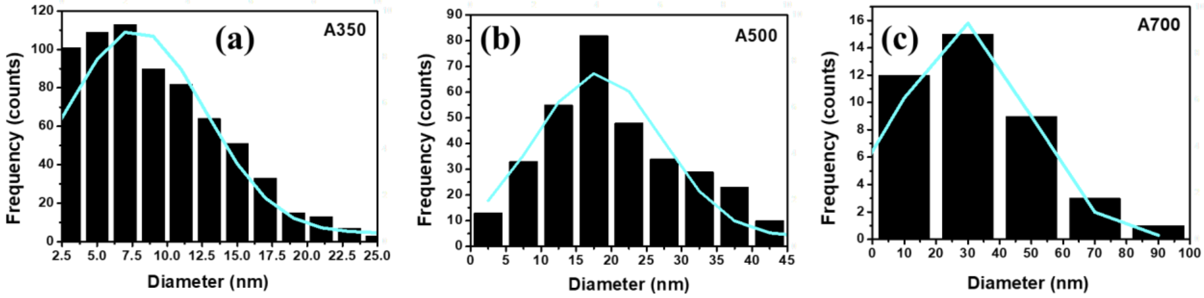

Figure 5.11. Particle distribution function with the corresponding Gaussian curve fitting for S3 sample annealed at (a) A350, (b) A500 and (c) A700.

Table 5.1. Structural and crystallite summaries of the five prepared samples with different TG concentrations (S1-S5) and no TG (S0).

Sample	Observed phase	Crystallite size (nm)	Particle size (nm)	Annealed samples	Particle size (nm)
S0	Mixed	–	14.8 ± 6.4	A200	-
S1	Mixed	–	10.4 ± 4.1	A350	7.8 ± 4.9
S2	Mixed	–	9.8 ± 6.3	A500	18.1 ± 9.0
S3	Hexagonal	3.0	8.8 ± 4.2	A700	28.6 ± 20
S5	Hexagonal	2.95	7.0 ± 2.0		

Optical analysis

5.3.5 UV-Vis

Figure 5.12 shows the UV-Vis spectra of CdS NPs obtained by absorption of electromagnetic radiation. The room temperature spectra were obtained by dispersing the NPs in dimethyl sulphoxide (DMSO) and measuring between 300 and 600 nm. The spectra have a distinct absorption edge. The absorption edge of S0 (without TG) is at about 480 nm (Figure 5.12). This is at lower wavelengths when compared to the reported value for bulk CdS (515 nm) [12]. The addition of 0.1 mL of TG (S1) shifts the absorption edge of the CdS NPs to 418 nm. S5 (0.8 mL TG) showed the biggest shift from bulk CdS absorption edge to 380 nm. This trend of a shift in absorption edge with an increasing capping agent concentration is persistent throughout and is known as the blue shift [28]. Blue shift is a contribution of the quantum confinement effect where a decrease in particle size, leads to an increase in the particle's observed band-gap energy.

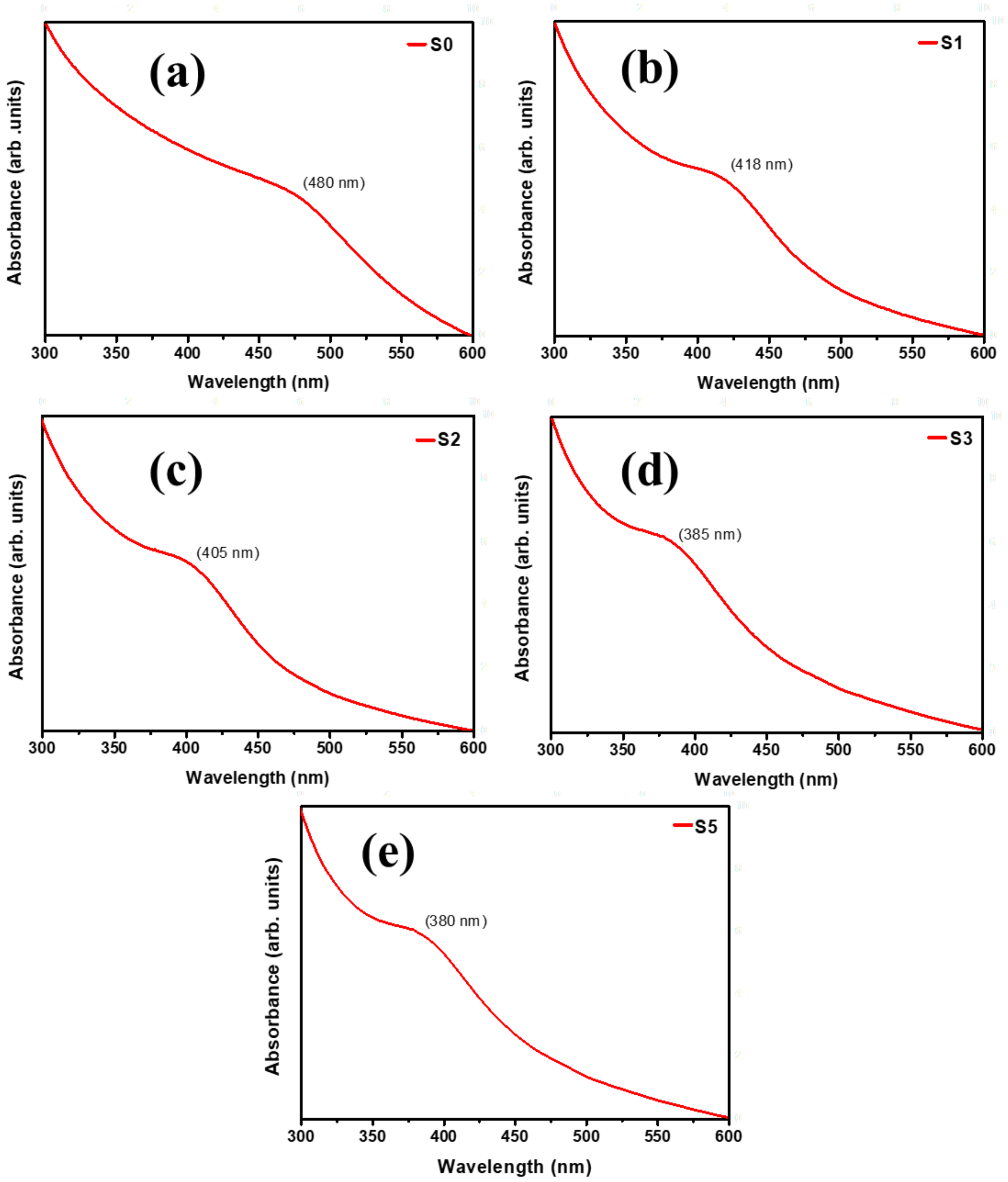

Figure 5.12. UV-Vis absorption spectra of CdS NPs; (a) S0, (b) S1, (c) S2, (d) S3, and (e) S5.

A distinct peak with a sharp edge on a UV-Vis absorption spectra is usually associated with a small size distribution [29]. This is observed in the obtained spectra, the absorption edge becomes sharper upon addition of TG (S1) when compared to S0.

5.3.6 PL

Figure 5.13 shows the photoluminescence spectra of as-prepared CdS NPs with increasing TG concentration. The spectra depicts defects present in the NPs and how they're affected by the capping agent. The EDS results in *section 5.3.3* showed that the increasing TG concentration (Figure 5.6) introduces more sulfur atoms to the NP surface while annealing (Figure 5.7) reduces the sulfur concentration. This shows that the defect concentration increases with capping agent concentration while it decreases with annealing temperature. The enhancement in defect concentration due to the presence of interstitial sulfur has been reported previously by Singh *et al.* [14] and Pedrotti *et al.* [30]. The present defects are discussed according to their origins and distinguished with the emission energy colour on the electromagnetic spectrum.

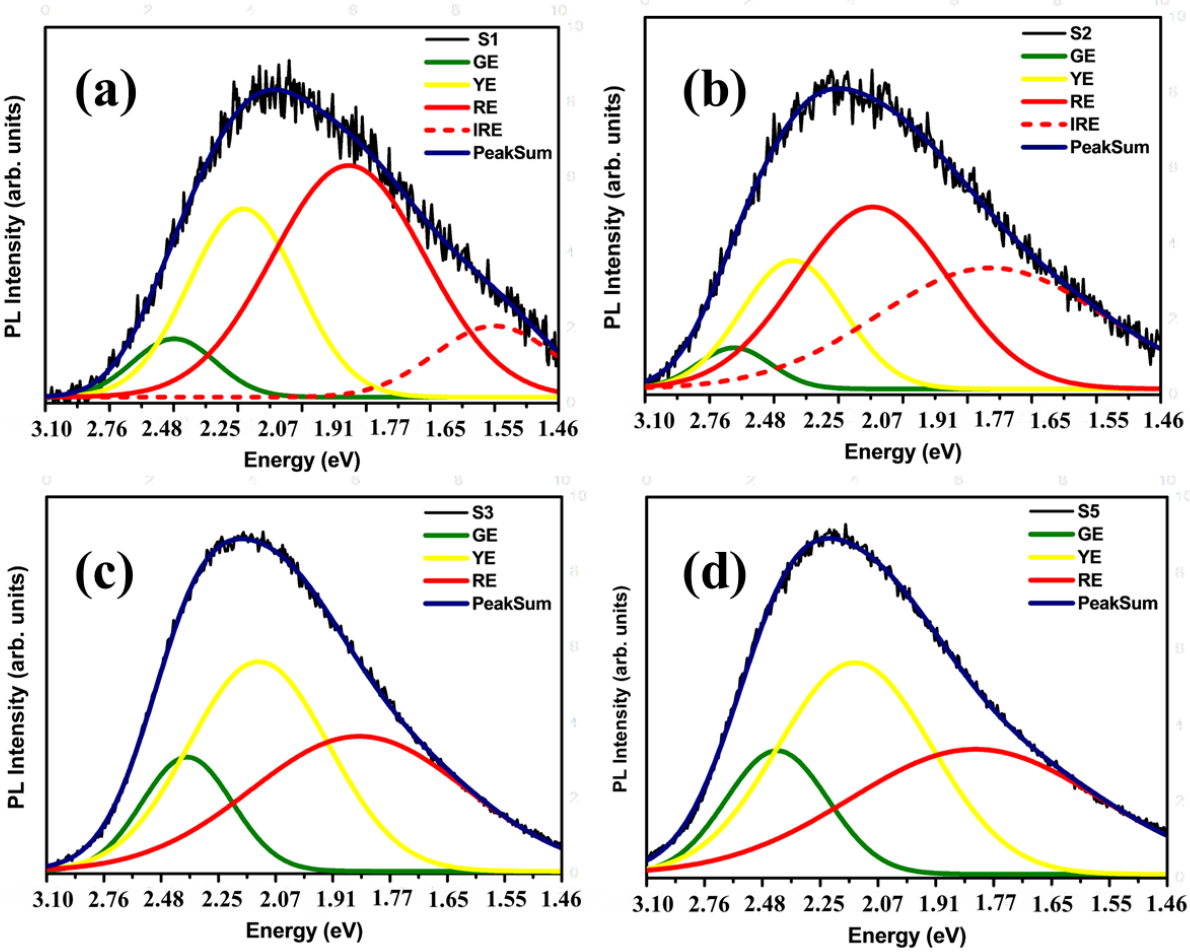

Figure 5.13. PL spectra of CdS NPs with different TG concentrations; (a) S1, (b) S2, (c) S3, and (d) S5.

Luminescence between 3.1-1.91 eV emission wavelengths is known as the green emission (GE) band in CdS NPs [11]. The origin of this band is said to be (1) the recombination of free electrons from the conduction band with holes captured on an acceptor level [31]; (2) recombination of electrons from the donor level with holes trapped on an acceptor level. The yellow emission (YE) is due to the recombination *via* surface localized states, the radiative transition from donor levels. These include Cd atoms located at interstitial sites (I_{Cd}) to the valence band [32][33], or a donor to acceptor level transition from interstitial Cd-Cd vacancy complex (I_{Cd}-V_{Cd}) [34]. In CdS NPs, Cd vacancies and interstitial atoms act as electron acceptors while S vacancies as well as interstitial atoms of cadmium act as donors [14]. After the annealing experiment, where sample S3 was annealed at various temperatures in an argon rich environment as discussed before, the PL properties (Figure 5.14) of CdS changed.

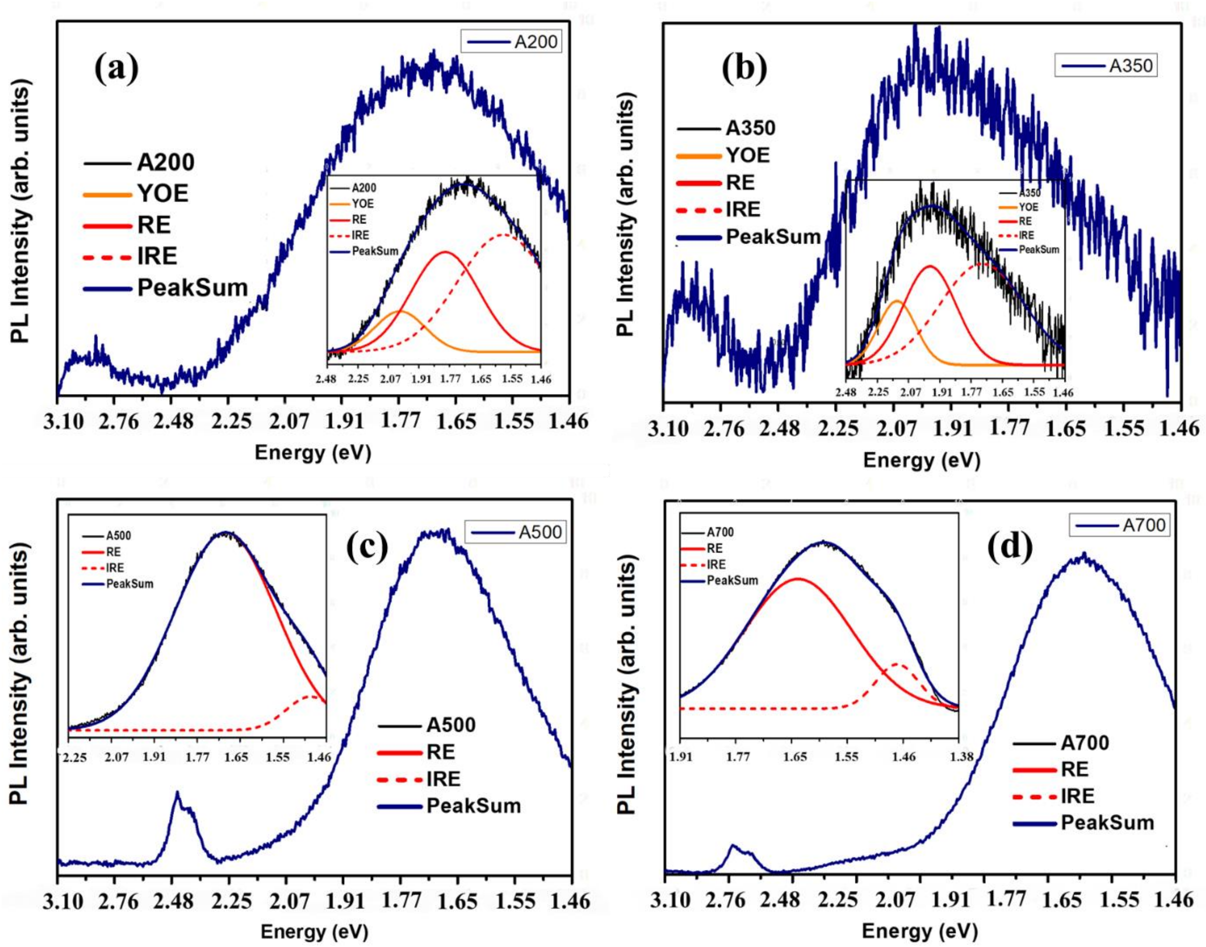

Figure 5.14. PL spectra of the S3 sample annealed at different temperatures; (a) A200, (b) A350, (c) A500, and (d) A700.

At temperatures in the range below the threshold temperature of 350 ℃ (where phase transformation occurred), the GE intensity decreased with increasing temperature. This attests to (as mentioned before) the S defect concentration decrease. This is accompanied by a shift of the peak to higher energies, caused by the decrease in particle size (i.e. the quantum confinement effect). However, above the phase transformation temperature, the second peak of very high intensity is observed between 2.07-1.55 eV. The red emission (RE) is assigned to sulfur vacancies [35]. The emission mechanism for this band is either by trapping of hole carriers or recombination with trapped holes [36]. The increase in the ratio of Cd to S leads to an apparent excess in Cd atoms due to the absence of S atoms in the form of S vacancies leads to an intrinsic n-type conductivity [37]. The defect concentration of this peak increases with increasing annealing temperature, with the peak moving to lower energies.

Samples A200 and A350 (Figure 5.14) have a yellow-orange emission (YOE) peak caused by structural impurities that are persistent at low temperatures. Above the phase transformation temperature, this peak disappears leaving the intransigent RE and infrared emission (IRE). Another important thing to note is the decrease in the intensity of the IRE relative to the RE above this transformation phase. This is due to increasing sulfur vacancies at high annealing temperatures which is consistent with the EDS results reported earlier.

Table 5.2. CdS PL emission band shifts that occur as a consequence of particle size variation and annealing temperature.

Samples	GE(eV)	YE (eV)	RE (eV)	IRE (eV)
S1	2.25	2.05	1.81	1.55
S2	2.39	2.20	1.98	1.73
S3	2.37	2.12	1.84	-
S5	2.42	2.14	1.81	-
A200	2.92	2.00	1.79	1.57
A350	2.95	2.13	1.96	1.73
A500	2.43	-	1.69	1.49
A700	2.43	-	1.64	1.47

The peak sum position moves to higher energies as the temperature approaches the transformation phase temperature and starts to shift to lower energies above the phase transformation. Below the transformation phase, there is a blue emission (~2.76 eV) peak, which is red-shifted to 2.43 eV (GE) above this temperature. However, the occurrence of the

GE peak above the transformation phase confirms the anti-blue shift that goes with the structural change of the as-prepared CdS NPs [38].

The temperature effects on PL emissions are summarized in table 5.2, the decreasing particle size results in a blue shift in the GE peaks and increasing the annealing temperature counters this effect. The results show that annealing the S3 sample introduces the IRE. Thus it can be concluded that the emission colour of CdS NP may be tuned by changing the NP size (either *via* the capping agent concentration or by giving the material a heat treatment) and thus changing the phase - structure of the NPs.

Surface analysis

5.3.7 FTIR

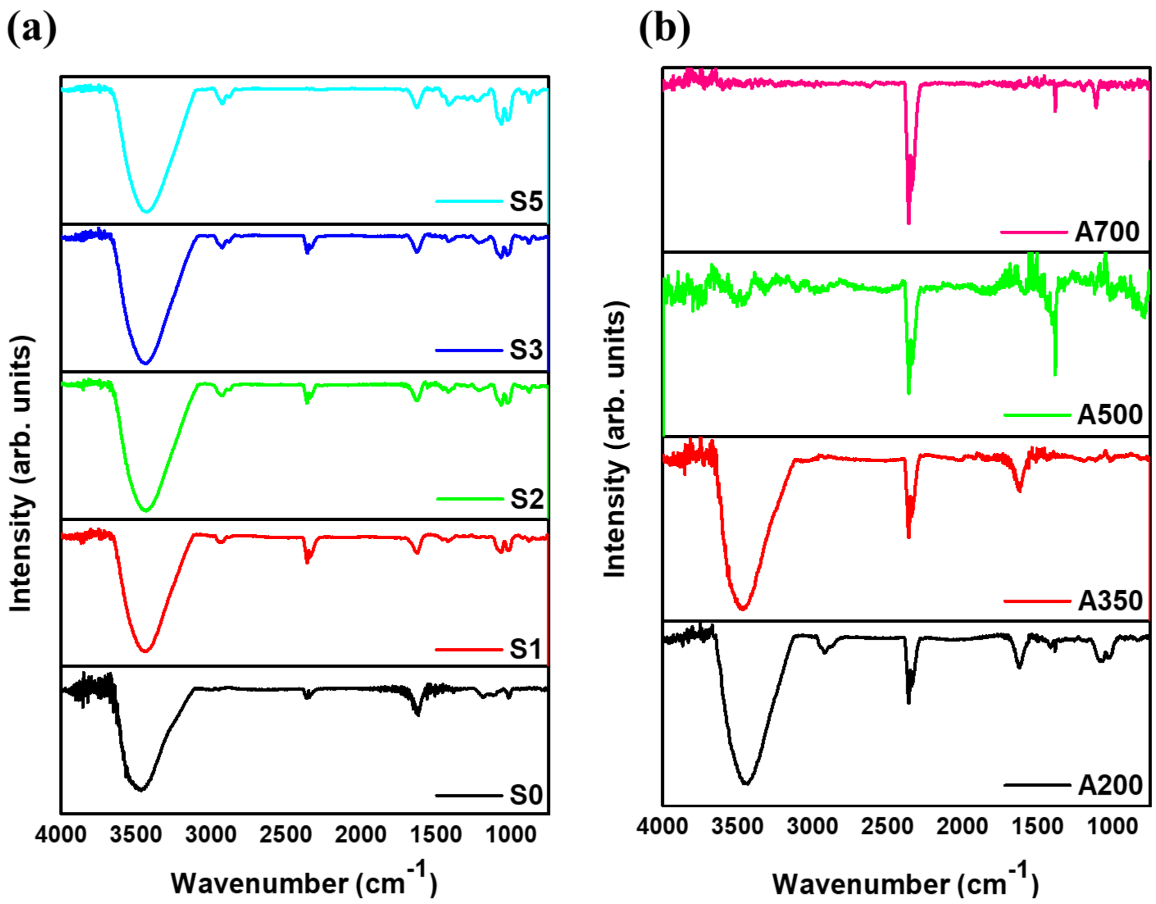

Figure 5.15. FTIR spectra of CdS NPs (a) with different capping agent concentrations; S1, S2, S3, and S5, (b) the effect of annealing temperature on S3; A200, A350, A500, and A700.

Dry CdS NP powder was mixed with KBr to improve transparency and characterized with FTIR. This technique was used to study the purity and composition of the synthesized products.

It determines the functional groups and types of bonds present in the system. FTIR spectra of Figure 5.15 shows both the (a) as-prepared and (b) the annealed CdS samples. At high wavenumbers (between 3800 cm^{-1} and 3000 cm^{-1}) an O-H stretching mode of water is observed at 3434 cm^{-1} [39]. The presence of lattice water is observed by the peak at 1629 cm^{-1}. The difference between these water may be explained in terms of orientation. The lower wavenumber water is related to the vibration of bonds preferentially elongated along the *c*-axis whereas the higher wavenumber water relates to the vibration of the bonds elongated along the *a*-axis [40]. Hydrogen-bonded stretching bands are observed at 2500 - 3200 cm^{-1}. These stretching modes are observed due to the presence of the intramolecular hydrogen bonds in the capping agent (TG) and at 3200 - 3600 cm^{-1} due to intermolecular hydrogen bonds [14][41].

The peak at 2962 cm^{-1} is a stretching vibration of CH_2. The S-H stretching mode should be observed at 2552 cm^{-1} for unreacted, pure TG.[42]. Therefore, the absence of this peak indicates that TG has successfully reacted and has bonded to the CdS NP through the sulfur head-group onto a surface Cd atom. Asymmetric stretching of CO_2 is also observed at 2361 and 2342 cm^{-1} respectively. The C-O stretching at 1067 cm^{-1} is evidence of the presence of the TG in the system as these elements are present in this organic molecule and the C–C stretching mode at 883 cm^{-1} further confirms this. Successful removal of the lattice water is achieved above the temperature of 350 °C. This is evident in Figure 5.15 (b), sample A500. In this spectrum, the O-H vibrational peak centred around 3434 cm^{-1} is no longer present, indicating that most (if not all) of the water molecules trapped inside the CdS NP crystals structure has successfully been removed with the heat treatment. However, as is evident from the change in the rest of the spectra (A700 and A500) the removal of the organics on the surface of the CdS NPs is also evident, leaving behind dangling bonds.

5.3.8 XPS

XPS analysis was used to further confirm the chemical state and surface composition of CdS NPs. Full XPS spectra are presented in Figure 5.16 for CdS NPs with different particle sizes. The spectra indicate the presence of cadmium, sulfur, oxygen, carbon, and chlorine.

The composition is similar to that obtained by EDS. Another important observation on the spectra is the apparent reduction in the background intensity as a function of particle size. This is even more apparent at the higher binding energy. This is yet another confirmation of the change in the size of the particles [29]. The surface contains C (285.75 eV) peak and O (533.25 eV) peaks. Figure 5.17 shows S (2p) spectra of the CdS NP samples with different sizes.

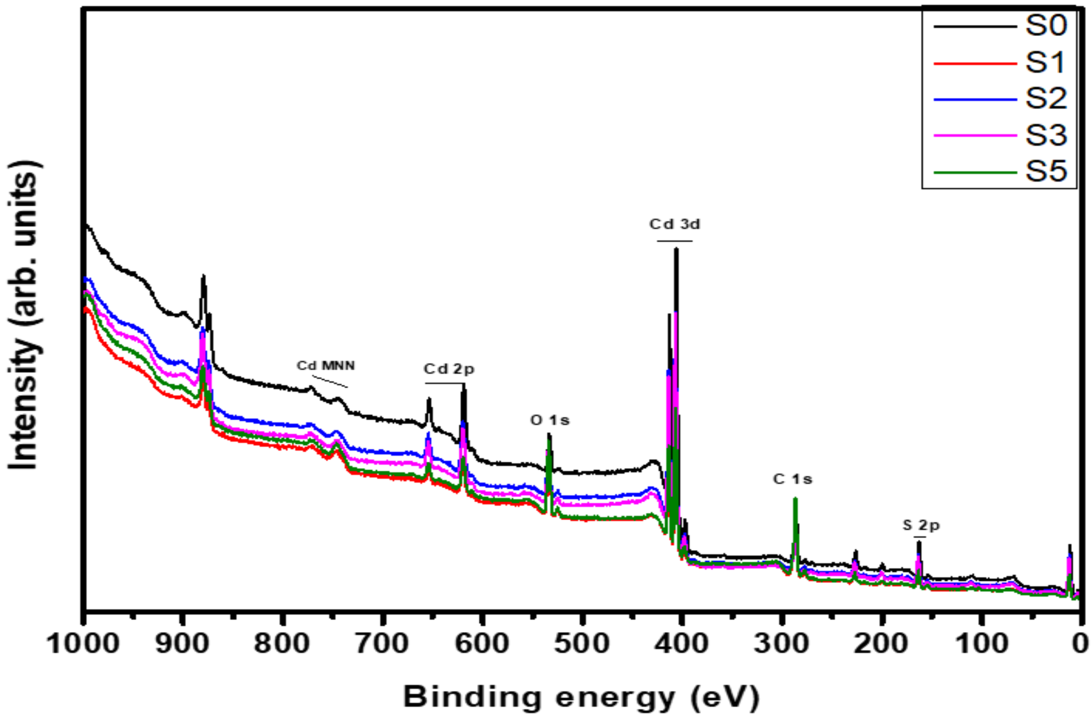

Figure 5.16. XPS spectra for CdS NPs showing a decrease in the background intensity with decreasing particle size (from S0 to S5).

The spectra exhibit spin-orbit splitting of the $2p_{1/2} – 2p_{3/2}$ doublet with a fixed peak area ratio of 1:2. The energy separation between the doublet is in agreement with what is found in the existing literature and is 1.2 eV [43]. The fitted doublet (Figure 5.17) shows weak S^{2-} and RS-H components with binding energies of 161.87 eV and 164. 22 eV respectively. The observed S^{2-} peak shows the successful formation of CdS and the RS-H peak further confirms the bond formed by TG on the CdS surface and goes on to show that the sulfur observed is distinctly from these two sources. The different species within these NPs in the binding energy range from 160 eV to 167 eV may be located quite differently and are quite sensitive to a small change in the particle size [29]. A shift in this peak position is observed in S5 with S^{2-} and RS-H located at 162.22 and 164.14 eV respectively. This observation is an indication of the quantum confinement effect as well as lattice strain influence the valence and the core electrons differently. This shift in binding energy of valence band with respect to Fermi level and narrowing of valence band spectra has been reported a number of times in recent years [44].

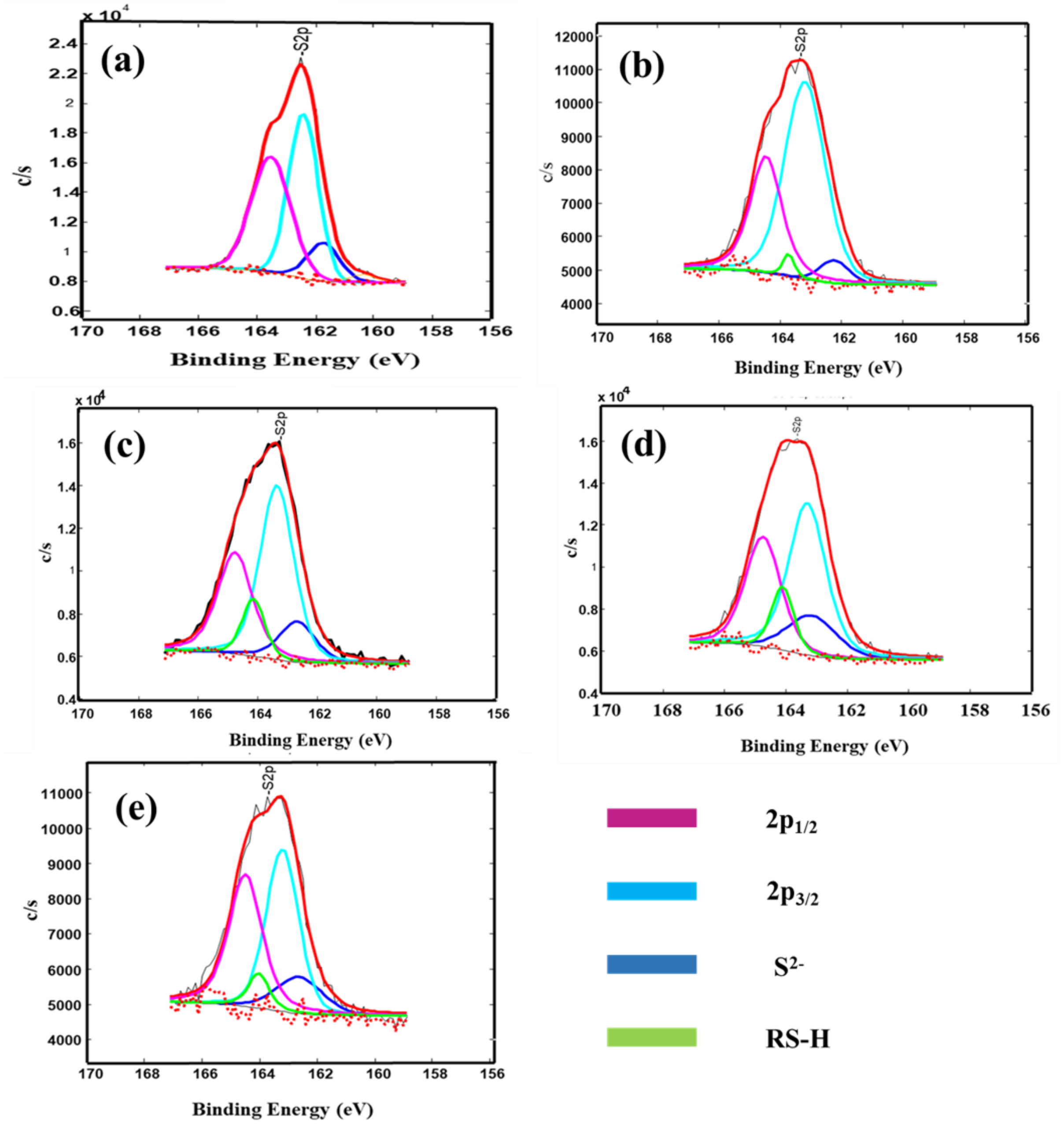

Figure 5.17. X-ray photoemission spectra of S 2p core levels in CdS of various TG concentrations. (a) S0, (b) S1, (c) S2, (d) S3, and (e) S5.

5.5 Conclusion

In this chapter CdS NPs have been successfully prepared using water as a solvent in a chemical precipitation method. Water solvent allowed fast dissolution of the starting material, which brought about a colour change during the particle growth process indicating a variation in size. The structure of the NPs was mainly dependent on size. Increasing the TG concentration reduced the particle size, while also increasing the density of the sulfur defects. This increase in the concentration of sulfur interstitials was responsible for the increase in the peak sum luminescence intensity of the CdS NPs, while annealing of these NPs introduced sulfur vacancies as the TG capping agent which is responsible for the increase in sulfur content, broke away from the NPs surface. Particle growth due to dangling bonds drove the sintering process to reduce surface area as one of its effects of annealing, together with phase transformation at temperatures above 350℃. Particles that resulted from sintering showed well-defined boundaries. The work showed that one can successfully tune the luminescence properties of CdS NPs by varying particle size to obtain the desired emission colour. Annealing of these NPs introduced infrared emissions with very high intensities.

References

[1] V. Singh, P. K. Sharma, and P. Chauhan, “Synthesis of CdS nanoparticles with enhanced optical properties,” *Mater. Charact.*, vol. 62, no. 1, pp. 43–52, 2011.

[2] A. B. Knudson, M.D.; Gupta, Y.M.; Kunz, “Picosecond Electronic Spectroscopy to Determine the Transformation Mechanism for the Pressure-Induced Phase Transition in Shocked CdS,” 1999.

[3] E. Roduner, “Size matters: why nanomaterials are different,” *Chem. Soc. Rev.*, vol. 35, no. 7, p. 583, 2006.

[4] Y. Gogotsi, *Nanomaterials Handbook*. LLC: United States of America: CRC Taylor & Francis Group, 2006.

[5] R. J. Bandaranayake, G. W. Wen, J. Y. Lin, H. X. Jiang, and C. M. Sorensen, “Structural phase behavior in II-VI semiconductor nanoparticles,” *Appl. Phys. Lett.*, vol. 67, no. 1995, p. 831, 1995.

[6] C. Ricolleau, L. Audinet, M. Gandais, and T. Gacoin, “Structural transformations in II-VI semiconductor nanocrystals,” *Eur. Phys. J. D-Atomic, Mol. Opt. Plasma Phys.*, vol. 9, no. 1, pp. 565–570, 1999.

[7] V. Singh, P. K. Sharma, and P. Chauhan, “Synthesis of CdS nanoparticles with enhanced optical properties,” *Mater. Charact.*, vol. 62, no. 1, pp. 43–52, 2011.

[8] N. Moloto, “Synthesis, properties and applications of Mn, Co, Ni and Cu chalcogenide nanoparticles,” pp. 1–206, 2009.

[9] N. Soltani, E. Gharibshahi, and E. Saion, “Band Gap of Cubic and Hexagonal Cds Quantum Dots - Experimental and Theoretical Studies,” *Chalcogenide Lett.*, vol. 9, no. 7, pp. 321–328, 2012.

[10] J. Nanda, B. A. Kuruvilla, and D. D. Sarma, “Photoelectron spectroscopic study of CdS nanocrystallites,” *Phys. Rev. B*, Mar-1999. [Online]. Available: https://link.aps.org/doi/10.1103/PhysRevB.59.7473.

[11] B. Rao, B. Kumar, V. Reddy, and T. Rao, “Preparation and characterization of CdS

nanoparticles by chemical co-precipitation technique," *Chalcogenide Lett.*, vol. 8, no. 3, pp. 177–185, 2011.

[12] V. Singh and P. Chauhan, "Synthesis and structural properties of wurtzite type cds nanoparticles," *Chalcogenide Lett.*, vol. 6, no. 9, pp. 421–426, 2009.

[13] O. Zelaya-Angel, J. J. Alvarado-Gil, R. Lozada-Morales, H. Vargas, and A. Ferreira Da Silva, "Band-gap shift in CdS semiconductor by photoacoustic spectroscopy: Evidence of a cubic to hexagonal lattice transition," *Appl. Phys. Lett.*, vol. 64, no. 3, pp. 291–293, 1994.

[14] V. Singh and P. Chauhan, "Structural and optical characterization of CdS nanoparticles prepared by chemical precipitation method," *J. Phys. Chem. Solids*, vol. 70, no. 7, pp. 1074–1079, 2009.

[15] A. Goswami, "Thin Film Fundamentals." p. 556, 1996.

[16] M. Liu, Y. Han, L. Tang, J.-F. Jia, Q.-K. Xue, and F. Liu, "Interplay between quantum size effect and strain effect on growth of nanoscale metal thin films," *Phys. Rev. B*, vol. 86, no. 12, pp. 1–5, 2012.

[17] C. M. Wei and M. Y. Chou, "Theory of quantum size effects in thin Pb(111) films," *Phys. Rev. B*, vol. 66, no. 23, p. 233408, Dec. 2002.

[18] S. Bhaumik, "What is the main reason that nano particles get agglomerated?," *SRM University*. [Online]. Available: https://www.researchgate.net/post/What_is_the_main_reason_that_nano_particles_get_agglomerated. [Accessed: 15-May-2018].

[19] S. Riaz, A. Butt, and S. Naseem, "Synthesis and Characterization of CdS and CdTe Inks for Solar Cells," no. Jamali 2007, pp. 654–665.

[20] K. Koc, A. Panác, R. Dvorsky, and P. Praus, "Journal of Colloid and Interface Science CdS nanoparticles deposited on montmorillonite : Preparation , characterization and application for photoreduction of carbon dioxide," vol. 360, pp. 574–579, 2011.

[21] Y. M. Mo, Y. Tang, F. Gao, J. Yang, and Y. M. Zhang, "Synthesis of fluorescent CdS quantum dots of tunable light emission with a new in situ produced capping agent,"

Ind. Eng. Chem. Res., vol. 51, no. 17, pp. 5995–6000, 2012.

[22] K. H. Müller *et al.*, "Biomaterials The effect of particle agglomeration on the formation of a surface- connected compartment induced by hydroxyapatite nanoparticles in human monocyte-derived macrophages," *Biomaterials*, vol. 35, no. 3, pp. 1074–1088, 2014.

[23] H. Poppa, "'The interaction of small particles and thin films of metals with gases.,'" *Thin Solid Films*, vol. 34(1), p. 94, 1976.

[24] J. J. Chen and E. Ruckenstein, "Sintering of palladium on alumina model catalyst in a hydrogen atmosphere," *J. Catal.*, vol. 69, no. 2, pp. 254–273, Jun. 1981.

[25] C. H. Bartholomew, "Sintering kinetics of supported metals: new perspectives from a unifying GPLE treatment," *Appl. Catal. A Gen.*, vol. 107, no. 1, pp. 1–57, Dec. 1993.

[26] P. Wynblatt and N. A. Gjostein, "Particle growth in model supported metal catalysts—I. Theory," *Acta Metall.*, vol. 24, no. 12, pp. 1165–1174, Dec. 1976.

[27] B. K. Min, A. K. Santra, and D. W. Goodman, "Understanding silica-supported metal catalysts: Pd/silica as a case study," *Catal. Today*, vol. 85, no. 2–4, pp. 113–124, 2003.

[28] R. Banerjee, R. Jayakrishnan, and P. Ayyub, "Effect of the size-induced structural transformation on the band gap in CdS nanoparticles . J Phys Cond Matt," *J. Phys. Condens. Matter*, vol. 12, no. September 2015, pp. 10647–10654, 2000.

[29] S. Joshi, "Preparation and characterization of CdS nanoparticles," *Inorg. Chem. Commun.*, no. c, pp. 1522–1523, 2004.

[30] L. S. Pedrotti and D. C. Reynolds, "Change in Structure of Blue and Green Fluorescence in Cadmium Sulfide at Low Temperatures," *Phys. Rev.*, vol. 119, no. 6, pp. 1897–1898, Sep. 1960.

[31] C. Mejía-García., A. Escamilla-Esquivel, G. Contreras-Puente, M. Tufiño-Velázquez, M. L. Albor-Aguilera, O. Vigil, and L. Vaillant, "Photoluminescence studies of CdS films grown by close-spaced vapor transport hot walls," *J. Appl. Phys.*, vol. 86, no. 6, pp. 3171–3174, 1999.

[32] S. Chandramohan, R. Sathyamoorthy, P. Sudhagar, D. Kanjilal, D. Kabiraj, K. Asokan, V. Ganesan, T. Shripathi, U.P. Deshpande, “High-energy heavy-ion induced physical and surface-chemical modifications in polycrystalline cadmium sulfide thin films,” *Appl. Phys. A Mater. Sci. Process.*, vol. 94, no. 3, pp. 703–714, 2009.

[33] P. Kumar, N. Saxena, R. Chandra, K. Gao, S. Zhou, A. Agarwal, F. Singh, V. Gupta, D. Kanjilal, “SHI induced enhancement in green emission from nanocrystalline CdS thin films for photonic applications,” *J. Lumin.*, vol. 147, pp. 184–189, 2014.

[34] O. Vigil, I. Riech, M. Garcia-Rocha, and O. Zelaya-Angel, “Characterization of defect levels in chemically deposited CdS films in the cubic-to-hexagonal phase transition,” *J. Vac. Sci. Technol. A Vacuum, Surfaces, Film.*, vol. 15, no. 4, pp. 2282–2286, 1997.

[35] G. C. Papavassiliou, “Luminescence spectra and Raman excitation profiles in small CdS particles,” *J. Mol. Struct.*, vol. 79, no. C, pp. 395–398, 1982.

[36] Y. Wang and N. Herron, “Quantum size effects on the exciton energy of CdS clusters,” *Phys. Rev. B*, vol. 42, no. 11, pp. 7253–7255, Oct. 1990.

[37] K. P. Acharya, “Photocurrent Spectroscopy of CdS/Plastic, CdS/Glass, and ZnTe/GaAs Hetero-pairs Formed with Pulsed-laser Deposition.” 2009.

[38] A. Mercy, R. Samuel Selvaraj, B. Milton Boaz, A. Anandhi, and R. Kanagadurai, “Synthesis, structural and optical characterisation of cadmium sulphide nanoparticles,” *Indian J. Pure Appl. Phys.*, vol. 51, no. 6, pp. 448–452, 2013.

[39] N. V. Duffy, “Interpretation of infrared spectra,” *J. Chem. Educ.*, vol. 49, no. 9, p. 652, 1972.

[40] B. Kolesov, “Raman investigation of H2O molecule and hydroxyl groups in the channels of hemimorphite,” *Am. Mineral.*, vol. 91, no. 8–9, pp. 1355–1362, 2006.

[41] L. D. S. Yadav, “Organic Spectroscopy,” New Delhi: Anamaya publishers, 2004.

[42] N. Ben Brahim, M. Poggi, N.B.H. Mohamed, R.B. Chaâbane, M. Haouari, M. Negrerie, H.B. Ouada, “Synthesis, characterization and spectral temperature-dependence of thioglycerol-CdSe nanocrystals,” *J. Lumin.*, vol. 177, pp. 402–408, 2016.

[43] L. Zhang, L. Ji, P. A. Glans, Y. Zhang, J. Zhu, and J. Guo, “Electronic structure and chemical bonding of a graphene oxide-sulfur nanocomposite for use in superior performance lithium-sulfur cells,” *Phys. Chem. Chem. Phys.*, vol. 14, no. 39, pp. 13670–13675, 2012.

[44] I. Aruna, B. R. Mehta, L. K. Malhotra, and S. M. Shivaprasad, “Size dependence of core and valence binding energies in Pd nanoparticles: Interplay of quantum confinement and coordination reduction,” *J. Appl. Phys.*, vol. 104, no. 6, pp. 2–6, 2008.

CHAPTER 6

Effect of ethanol solvent on structural and optical properties of CdS preparation.

6.1 Introduction

In this chapter, we report on the synthesis of CdS NPs with the chemical precipitation method using ethanol as a solvent. The change in solvent is to study the effect of solvent in crystal structure, morphology, and luminescence of the CdS NPs. The starting materials in synthesis ($CdCl_2$, Na_2S, and TG) proved difficult to dissolve in ethanol compared to water (as discussed in chapter 5). During the preparation of the NPs, electrons are confined in three dimensions. The reduction of particle size to less than 10 nanometres are referred to as quantum dots (QD) since this is (usually) the size range where quantum confinement effects become prominent [1]. The ability to vary the particle size in NPs allows for tuning of their fundamental electronic and optical properties which are different relative to the bulk [2] [3]. Related work has shown that the optical properties of CdS depend on their preparation methods and conditions [4]. Electrical transport properties are also a function of the NP size as it requires a large variation in energy to remove or add charge in nanocrystals. Another influential characteristic is the influence of the surface characteristics on the optical properties of the quantum dot.

6.2 Experimental

CdS NPs of different sizes were synthesized using the chemical precipitation method and TG ($C_3H_8O_2S$) was used as the capping agent to control the particle size. All the reactions were carried out at room temperature and pressure. Cadmium chloride ($CdCl_2$) and sodium sulfide (Na_2S) were used as sources of Cd and S ions respectively. Ethanol was used as the solvent with varying TG concentrations to control the growth of NPs. Initially, 0.1 M of $CdCl_2$ and Na_2S were added in different pyrex glass beakers and mixed with 50 mL of ethanol separately [5]. The solutions were stirred vigorously with magnetic stirrers at room temperature. Different concentrations of TG (0.0, 0.1, 0.2, 0.3, 0.8 mL) were added to the Na_2S solution while stirring. The solutions were stirred for an hour to completely dissolve the starting material. The Na_2S-TG solution was then added dropwise to the $CdCl_2$ while constantly stirring using a magnetic stirrer. Particle growth started with the formation of precipitation, the colour of the solution changed from colourless to orange for 0.0 mL TG (S0), yellow for 0.1 mL TG (S1), 0.2 mL TG (S2), 0.3 mL TG (S3), and 0.8 mL TG (S5). All five CdS precipitates were washed with ethanol several times to remove impurities and unreacted reactants in a centrifuge for 15 minutes at 6000 rpm and then dried in an air oven for 10 hrs at 50 ℃.

Characterization

Structural properties of the CdS NPs were recorded and analysed using a Bruker D8 Advanced X-ray diffractometer (XRD) over the range of $20° < 2\theta < 60°$ equipped with monochromatic $CuK\alpha$ radiation of $\lambda = 1.54056$ Å (40 kV, 40 mA). To study the morphology, a JEOL JSM-7800F field emission scanning electron microscope (FE-SEM) fitted with Oxford Aztec 350 X-Max80 energy dispersive X-ray spectroscopy (EDS) were employed. While the photoluminescence (PL) spectra were measured using a PL laser system equipped with a 325 nm HeCd gas laser to excite the material at room temperature, with a spectrometer, a photomultiplier tube (PMT) detector, and a lock-in amplifier. For UV-Vis absorption, the dried powders were dispersed in dimethyl sulphoxide before collection of data with Lambda 950 UV-Vis spectrometer in the wavelength range of 250-700 nm.

6.3 Results and discussion

6.3.1 XRD

6.3.1.1 Crystal Phases

Figure 6.1 shows the XRD diffraction patterns of the as-prepared CdS NPs with different TG concentrations. The observed diffraction angles (2θ) values for S0 indicate six prominent peaks at 24.9°, 26.6°, 28.2°, 36.7°, 47.9°, and 51.9° assigned to the (100), (002), (101), (102), (103), and (112) diffraction planes, respectively according to the database of Inorganic Crystal Structure Data [ICSD#: 067789]. This indicates the existence of a single wurtzite hexagonal phase. However, the presence of the seventh peak at *43.8*° corresponding to the (110) diffraction plane indicates the presence of the cubic zinc blende phase [ICSD#: 031074]. With the introduction of TG, CdS XRD diffraction peaks found at 2θ values of *27.4*°, *43.8*°, and *51.8*° matched the diffraction pattern from (111), (220), and (311) planes respectively. This corresponds to the cubical zinc blend crystal structure. However, the low intensity shoulder observed at *47.9*° of the (103) diffraction plane indicates the presence of the hexagonal phase.

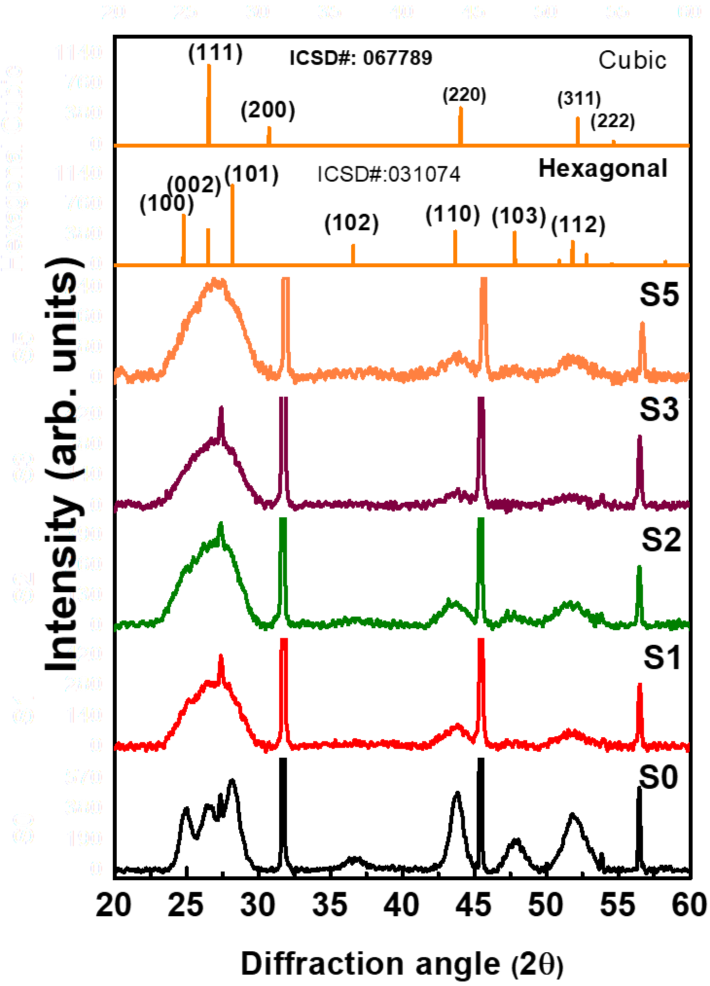

Figure 6.1. The XRD pattern of the as-prepared CdS QDs of different sizes for S0, S1, S2, S3, and S5.

Consequently, the as-prepared CdS samples exhibit a mixture of cubical and hexagonal phases which constitutes a very low percentage of the hexagonal phase. It is therefore evident that the use of ethanol as a solvent in the preparation of CdS NPs has resulted in a well-defined crystal structure compared to the samples prepared with water as a solvent which produces a XRD pattern with two very broad peaks indicative of NPs with highly mixed phases. In Figure 6.1 there are intense diffraction peaks observed at 31.8°, 45.5°, and 56.6° which are due to the presence of a $Cd(OH)_2$ phase [6], this indicates an incomplete reaction of the starting material. There is also an unknown sharp peak observed at 27°, which is accompanied by a broad low intensity peak at 47°. At the moment it is not clear where these peaks are from, the sharp peak disappears in sample S5. The broadening of the XRD peaks indicates a very small size regime.

6.3.1.2 Crystallite size

Table 6.1. CdS NPs crystallite size as a function of different TG concentration.

Samples	**S0**	**S1**	**S2**	**S3**	**S5**
FWHM (rad)	0.0209	0.0460	0.0463	0.0488	0.0539
Crystalline size (nm)	6.6	3.0	3.0	2.8	2.6

The broadening of the FWHM with increasing TG concentration in Figure 6.1 provides information about crystallite size. The Scherrer broadening observed indicates a decrease in particle size from S0 to S5 (Table 6.1). The decreasing particle size with increasing TG concentration attests to the capping molecule’s ability to control the size of the NPs during synthesis. The resultant particle size was calculated using (eq. 5.1) the (002) and (111) peaks in hexagonal and cubic structure respectively. There is, however, a very small diffraction angle difference between the two peaks [7]. The crystallite size of the NPs (in table 6.1) indicates size induced hexagonal to cubic phase transformation that occurs in sizes between 6 nm and 3 nm. Banerjee *et al.* [8] reported that this transformation occurs at approximately 4 nm for CdS. This is also in the size range in which quantum confinement is anticipated for CdS NPs [9].

6.3.2 UV-Vis

UV-Visible absorption spectroscopy is a good technique to monitor the optical properties of the NPs. The UV-Vis spectra of CdS NPs is shown in Figure 6.2. The spectra demonstrate a blue shift (in all five samples) with respect to bulk CdS. Bulk CdS has a well-known absorption edge at 515 nm [10][11] while for the as-prepared NPs, the absorption edge shifted to higher energies indicating widening in the band gap. The introduction of the capping agent clearly improves the stoichiometry of the NPs as S1, S2, S3, and S5 have a distinctive absorption edge peak relative to S0. The absorption edge shift is systematic with TG concentration (shown in table 6.2). It is evident that the shift to shorter wavelengths is due to increased TG concentration. The S5 sample shows the largest blue shift which is associated with the strong quantum confinement effects. As the crystal size becomes very small compared to the Bohr exciton radius, the energy levels within the electronic structure of the CdS become quantized and result in the blue-shift of the band-gap.

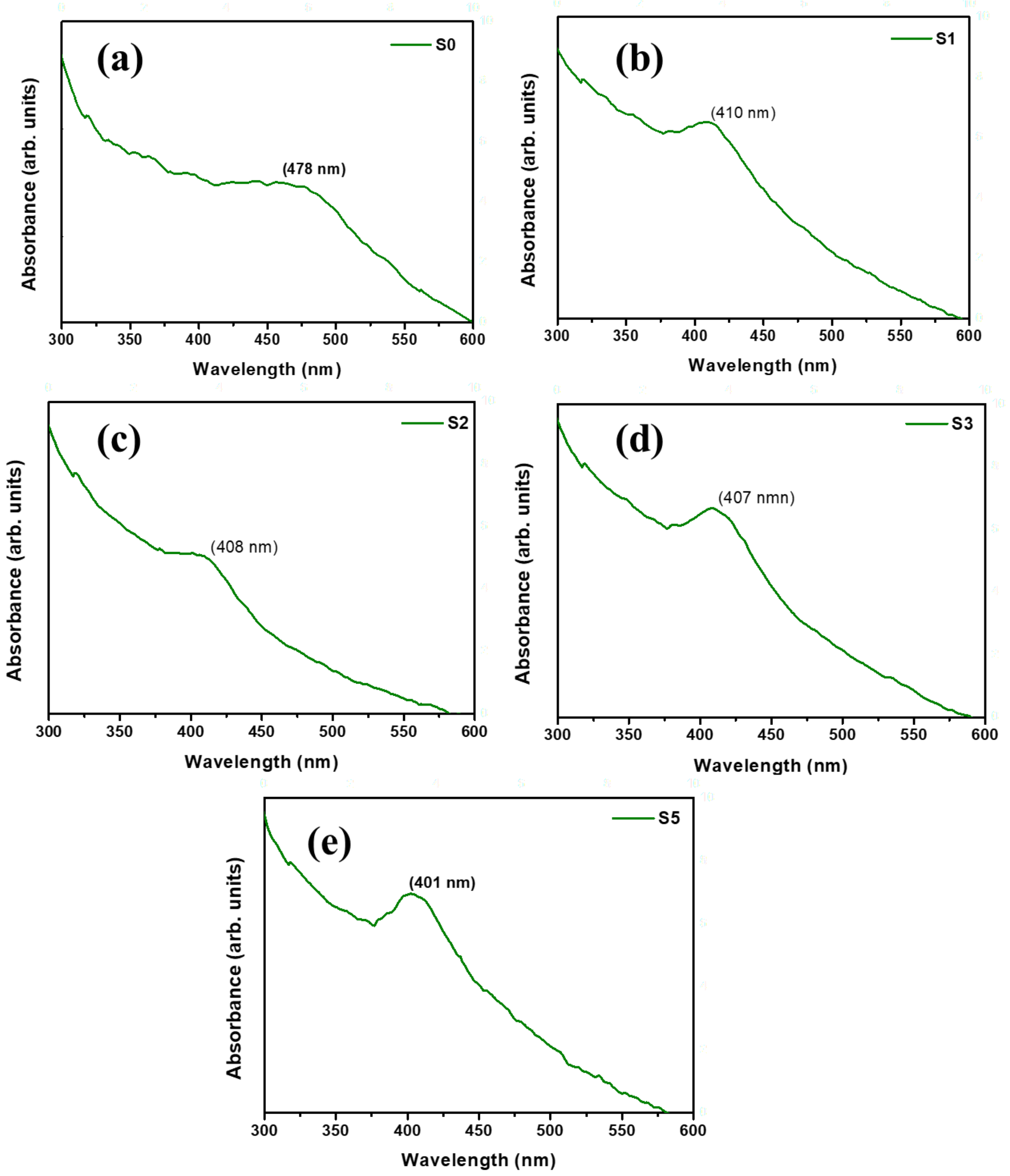

Figure 6.2. UV-Vis absorption spectra of CdS NPs. (a) S0, (b) S1, (c) S2, (d) S3, and (e) S5.

Table 6.2. Absorption edge of different CdS NPs differing according to the concentration of TG.

Samples	**S0**	**S1**	**S2**	**S3**	**S5**
Absorption edge (nm)	478	410	408	407	400

6.3.3 PL

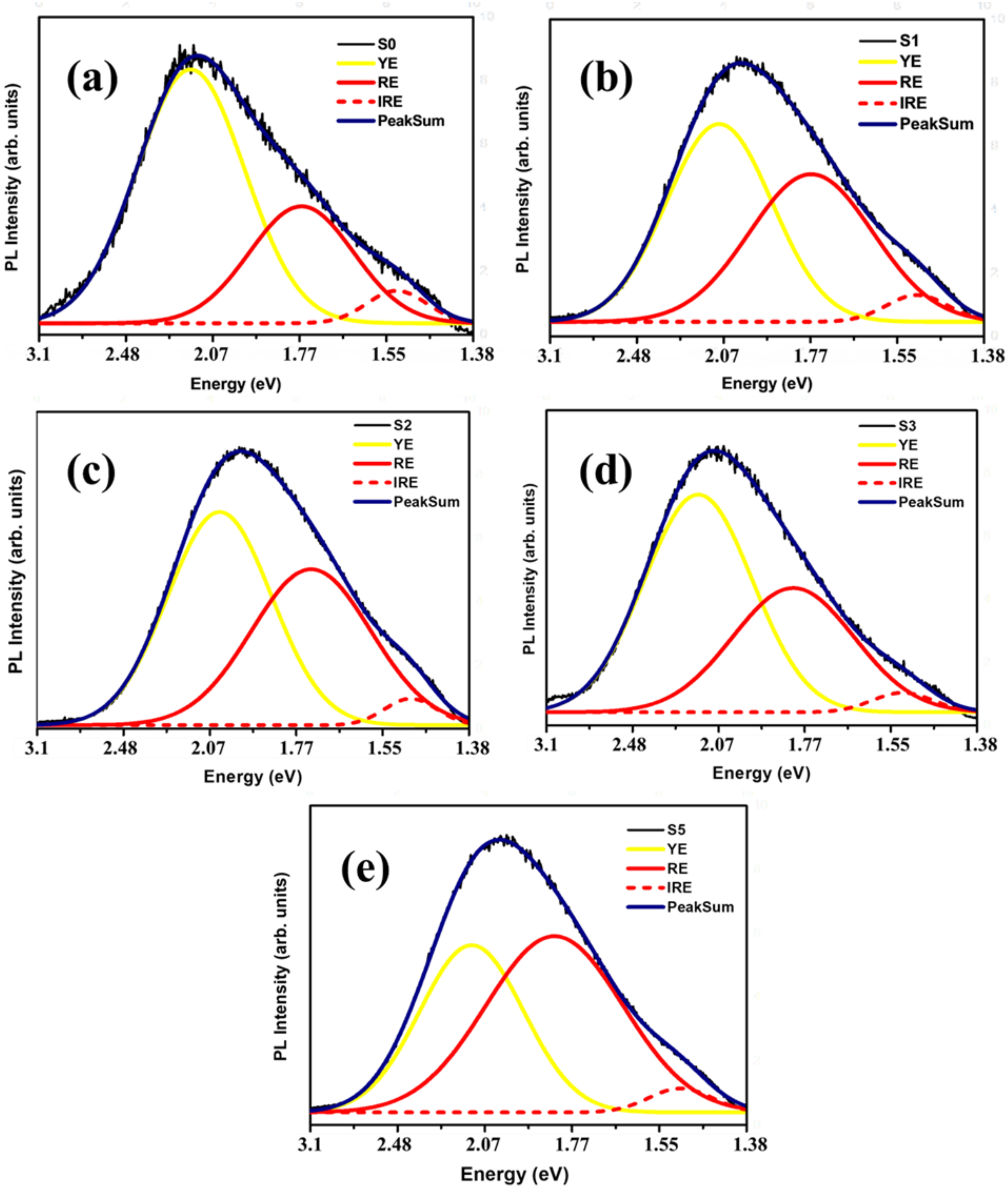

Figure 6.3. PL spectra of CdS NP with different TG concentrations: S0, S1, S2, S3, and S5.

The photoluminescence spectra of CdS NPs varying in size are depicted in Figure 6.3. The luminescence spectra show a very broad peak between 3.1-1.38 eV. S0, S1, S2, S3, and S5 are centred at 2.14, 1.99, 1.94, 2.07, and 1.97 eV respectively. There is an observed shoulder in the infrared region of the spectra. A red-shift is observed with increasing TG concentrations.

Deconvolution of the broad peak gave various emission bands; a YE, the RE, and the IRE are all attributed to defects. The YE is attributed to recombination *via* surface localized states, the radiative transition from donor levels. These include Cd atoms located at interstitial sites (I_{Cd}) to the valence band [12][13], or a donor to acceptor level transition from interstitial Cd-Cd vacancy complex (I_{Cd}-V_{Cd}) [14]. Misawa *et al*. [15] described the origin of the RE by a site-substitution model based on the creation of trap states by substituting the sulfur atoms responsible for GE with different counter-ions. The model involves a Cd vacancy pairing with a substitutional Cl on an adjacent S site producing a multifaceted centre $V_{Cd.Cl}$. The state of the band is dependent on particle size. In the S0 (no TG present) sample the red PL is at 1.77 eV, as a consequence of a deeper trap which functions as an accepting vacancy PL centre [16]. Holes are trapped into this centre through a nonradiative process and combine with electrons in the excited electronic level. With decreasing particle size in the S5 (TG present) sample, the $V_{Cd.Cl}$ complex centre acts as a shallow trap located near the conduction band. Electrons from this state combine with holes in the valence band to give low energy RE at 1.71 eV. The unreacted Cd species observed in XRD results are consistent with the proposed model by Misawa *et al*. A small infrared emission peak occurs at high wavelengths (1.55-1.49 eV) causing a shoulder in the overall peak. Luminescence around this region has been reported by Rao *et al* to occur as a consequence of shallow surface state [17].

6.3.4 SEM

SEM taken at similar magnifications were used to study the particle morphology of CdS NPs synthesized in an ethanol solvent. Figure 6.4 shows dispersed NPs with size varied as a function of TG concentration. The medium of suspension in CdS synthesis has been reported to play a crucial role in reducing the agglomeration of prepared samples [18][18]. CdS NPs prepared with ethanol as solvent showed improved dispersity compared to NPs prepared by water as a solvent (Chapter 5). An increase in TG concentration (from (a) to (e)) leads to more spherical morphology.

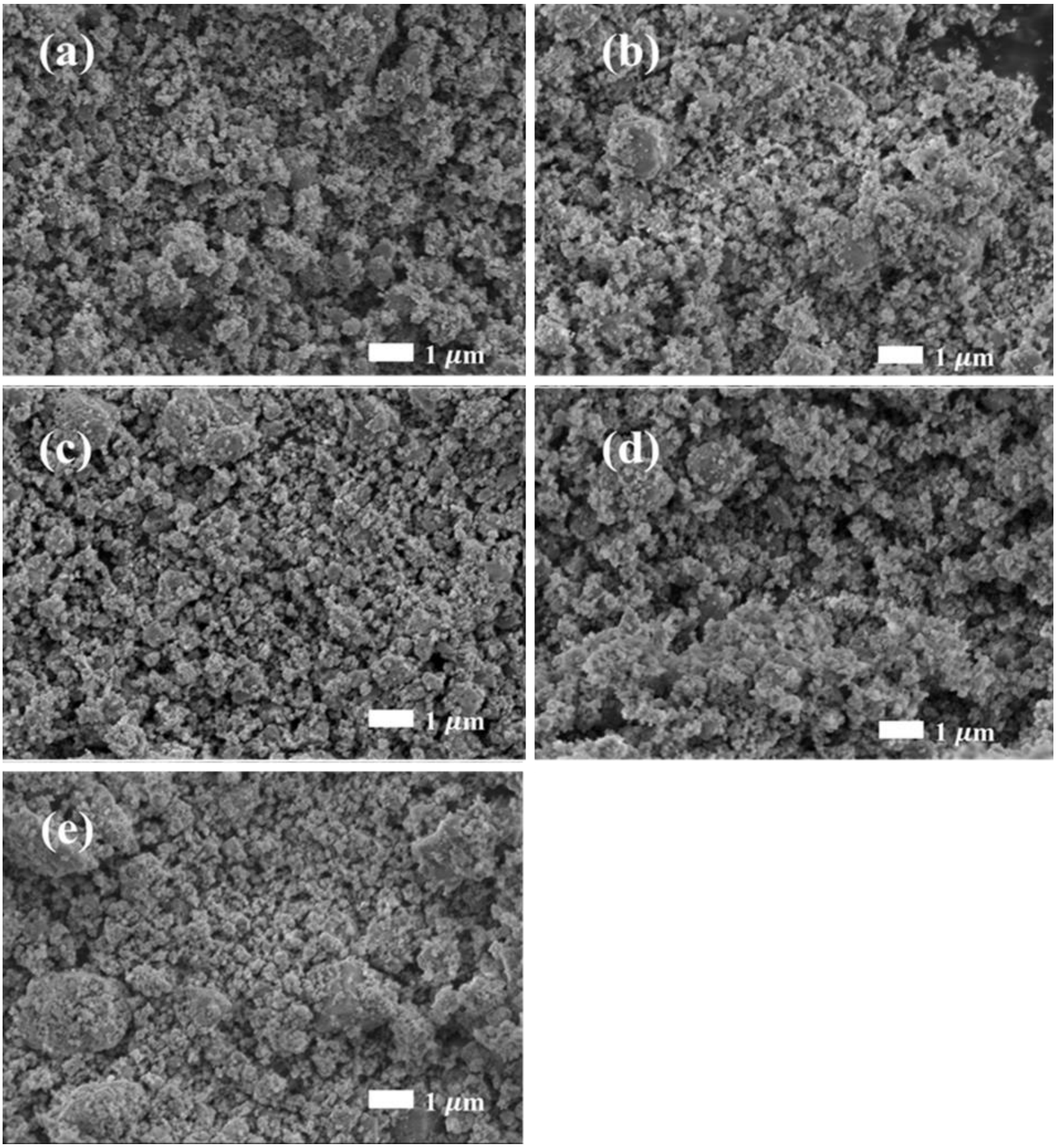

Figure 6.4. SEM images of the as-prepared CdS NPs with ethanol solvent (a) S0, (b) S1, (c) S2, (d) S3, and (e) S5.

6.3.5 EDS

EDS has been performed for compositional (%) analysis of CdS atoms together with related foreign atoms (Figure 6.5). Present elements are cadmium (Cd), sodium (Na), chloride (Cl), sulfur (S), carbon (C), and oxygen (O). The presence of Na and Cl indicates that the starting material did not completely dissolve, this attests to the observed XRD results showing a sharp $Cd(OH)_2$ peak.

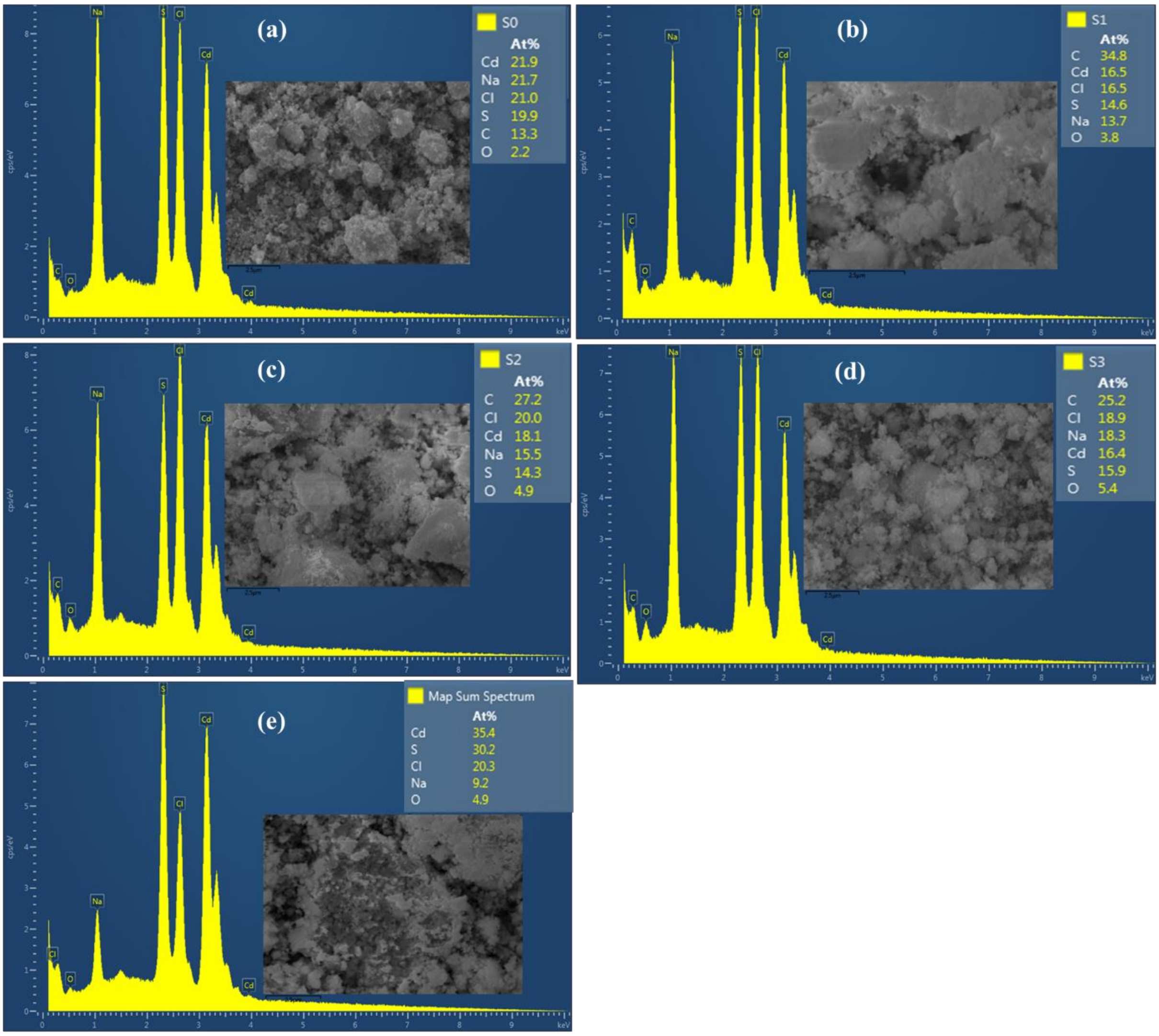

Figure 6.5. EDS of as-prepared CdS NP varying according to capping agent concentration (a) S0, (b) S1, (c) S2, S3, and S5.

The Cd and S peaks confirm the formation of CdS. The atomic ratio percentage for S to Cd in the above samples were; 0.91, 0.88, 0.79, 0.97, and 0.85 for S0, S1, S2, S3, and S5 respectively. From the EDS results, it is clear that the concentration of sulfur depends on the amount of Na_2S dissolved in the solvent. The dissolution concentrations of the starting material are also important in the intensity of the red luminescence.

6.4 Conclusion

In this chapter CdS NPs have been successfully prepared with an ethanol solvent. The starting material (powder), however, took an hour to dissolve (solution turn colourless) in the solvent. XRD results showed some $Cd(OH)_2$ peaks indicating incomplete dissolution. This led to the creation of shallow traps in the PL spectrum. As a consequence, in this chapter the IRE was successfully observed without the need for annealing, as was observed in CdS NPs prepared with the water solvent. Anticipated with the decreasing NP size there was a blue shift observed in the absorption edge of the CdS, which manifests the quantum confinement effect. This work also showed the role of the solvent in reducing surface energy that was brought about by the decreasing NP size. Thus, it can be concluded that the ethanol solvent results in more dispersed NPs relative to the water solvent.

References

[1] L. Prepared, C. R. King, and T. Ece, “Density of States : 2D, 1D and 0D,” *Slides*, 2005.

[2] B. Liu, G. Q. Xu, L. M. Gan, C. H. Chew, W. S. Li, and Z. X. Shen, “Photoluminescence and structural characteristics of CdS nanoclusters synthesized by hydrothermal microemulsion,” *J. Appl. Phys.*, vol. 89, no. 2, pp. 1059–1063, 2001.

[3] A. P. Alivisatos, “Semiconductor Clusters, Nanocrystals, and Quantum Dots,” vol. 271, pp. 933–936, 1996.

[4] T. Vossmeyer, L. Katsikas, M. Giersig, I. G. Popovic, K. Diesner, A. Chemseddine, A. EychmiUler, and H. Weller “CdS nanoclusters: Synthesis, characterization, size dependent oscillator strength, temperature shift of the excitonic transition energy, and reversible absorbance shift,” *J. Phys. Chem.*, vol. 98, no. 31, pp. 7665–7673, 1994.

[5] V. Singh, P. K. Sharma, and P. Chauhan, “Synthesis of CdS nanoparticles with enhanced optical properties,” *Mater. Charact.*, vol. 62, no. 1, pp. 43–52, 2011.

[6] P. Chawla, G. Sharma, S. P. Lochab, and N. Singh, “Effect of solvent-induced structural modifications on optical properties of CdS nanoparticles,” *Bull. Mater. Sci*, vol. 33, no. 5, pp. 535–541, 2010.

[7] O. Zelaya-Angel, J. J. Alvarado-Gil, R. Lozada-Morales, H. Vargas, and A. Ferreira Da Silva, “Band-gap shift in CdS semiconductor by photoacoustic spectroscopy: Evidence of a cubic to hexagonal lattice transition,” *Appl. Phys. Lett.*, vol. 64, no. 3, pp. 291–293, 1994.

[8] R. Banerjee, R. Jayakrishnan, and P. Ayyub, “Effect of the size-induced structural transformation on the band gap in CdS nanoparticles . J Phys Cond Matt,” *J. Phys. Condens. Matter*, vol. 12, no. September 2015, pp. 10647–10654, 2000.

[9] N. Moloto, “Synthesis, properties and applications of Mn, Co, Ni and Cu chalcogenide nanoparticles,” pp. 1–206, 2009.

[10] W. T. Yao, S. H. Yu, S. J. Liu, J. P. Chen, X. M. Liu, and F. Q. Li, “Architectural control syntheses of CdS and CdSe nanoflowers, branched nanowires, and nanotrees

via a solvothermal approach in a mixed solution and their photocatalytic property," *J. Phys. Chem. B*, vol. 110, no. 24, pp. 11704–11710, 2006.

[11] V. Singh and P. Chauhan, "Synthesis and structural properties of wurtzite type cds nanoparticles," *Chalcogenide Lett.*, vol. 6, no. 9, pp. 421–426, 2009.

[12] S. Chandramohan, R. Sathyamoorthy, P. Sudhagar, D. Kanjilal, D. Kabiraj, K. Asokan, V. Ganesan, T. Shripathi, and U.P. Deshpande, "High-energy heavy-ion induced physical and surface-chemical modifications in polycrystalline cadmium sulfide thin films," *Appl. Phys. A Mater. Sci. Process.*, vol. 94, no. 3, pp. 703–714, 2009.

[13] P. Kumar, N. Saxena, R. Chandra, K. Gao, S. Zhou, A. Agarwal, F. Singh, V. Gupta, D. Kanjilal, "SHI induced enhancement in green emission from nanocrystalline CdS thin films for photonic applications," *J. Lumin.*, vol. 147, pp. 184–189, 2014.

[14] O. Vigil, I. Riech, M. Garcia-Rocha, and O. Zelaya-Angel, "Characterization of defect levels in chemically deposited CdS films in the cubic-to-hexagonal phase transition," *J. Vac. Sci. Technol. A Vacuum, Surfaces, Film.*, vol. 15, no. 4, pp. 2282–2286, 1997.

[15] K. Misawa, S. Nomura, and T. Kobayashi, *Optics of Semiconductor Nanostructures, eds. F. Hennenberger*. Akademic, Berlin: F. Hennenberger, S. Schmitt-Rink and E. Göbel., 1993.

[16] Y. Wang, G. Meng, L. Zhang, C. Liang, and J. Zhang, "Catalytic growth of large-scale single-crystal CdS nanowires by physical evaporation and their photoluminescence," *Chem. Mater.*, vol. 14, no. 4, pp. 1773–1777, 2002.

[17] B. Rao, B. Kumar, V. Reddy, and T. Rao, "Preparation and characterization of CdS nanoparticles by chemical co-precipitation technique," *Chalcogenide Lett.*, vol. 8, no. 3, pp. 177–185, 2011.

[18] K. H. Müller, M. Motskin, A.J. Philpott, A.F. Routh, C.M. Shanahan, M.J. Duer, J.N. Skepper "Biomaterials The effect of particle agglomeration on the formation of a surface- connected compartment induced by hydroxyapatite nanoparticles in human monocyte-derived macrophages," *Biomaterials*, vol. 35, no. 3, pp. 1074–1088, 2014.

CHAPTER 7

Optical sensitivity of CdS-Au NCs prepared by physical techniques.

7.1 Introduction

The combined and often synergetic properties of nanocomposites have inspired research in the fields of nanoscience and nanotechnology. The optical sensitivity of semiconductor material is enhanced by combining them with metal components [1]. The new material performs much better than the individual components. Light-induced charge separation at the semiconductor/metal junction has been extensively studied in the field of photocatalysis. This synergetic effect has also been used in the development of highly sensitive, selective, fast and affordable materials for applications in the fields of photoelectrochemical (PEC) sensors [2], photocatalysis [3][4], biosensors [5], solar cells [6] and nanotechnology. One of the significant role players in the preparation of the nanocomposites is the light absorption ability of the semiconductor component. A large number of semiconductor structures have been used in the ultraviolet absorption region which makes up only 4% of the incoming solar light, limiting their use in the light-induced growth of the metal component. The recent advancement in the understanding of quantum confinement effects in semiconductor nanostructures has amended the absorption properties of these materials. Tailoring of these structures using the confinement effect allows the absorption in the visible region.

In this work, the deposition of gold (Au) component on the cadmium sulfide (CdS) surface was done using two physical techniques. This has been done to better control the size and shape of the metal components while observing the optical sensitivity of these structures to the changes. A number of growth mechanisms have been developed to prepare these nanocomposites, addressing the challenge of growing two different nanostructures into one nanocomposite in a controlled manner. The parameters that are taken into account during this preparation are; lattice constant mismatch and different crystal structure, the interfacial energy among the materials, the presence of surface defects, the presence of polar facets, the material miscibility, and the surface accessibility/reactivity [7]. The famous facet selective growth mechanism is known to grow the metal component on preferential nucleation and growth sites exploiting the well-defined semiconductor crystal structure [8][9]. Furthermore, Au QD have been previously reported to be responsible for fluorescence quenching of dyes over a broad range of wavelengths [10][11][12]. This is due to the creation of a Schottky contact allowing the light-induced charge transfer of electrons from the semiconductor component. Thus, the metal prevents electron-hole recombination at the CdS surface which is crucial in the enhancement of the photocatalytic activity of semiconductors [13]. This also allows a relatively large increase in photocurrent over the semiconductor NPs which is important in making photosensitive detectors [14].

7.2 Experimental

7.2.1 Preparation of CdS pellet

The CdS NPs prepared in chapter 6 were used to make a CdS pellet. The pellet was prepared using a 30-ton hydraulic press L-30 (Ser. No. 0365R). 200 g of the dried CdS powder was transferred into a bore and leveled with a smooth cover to prepare a smooth pellet. A pressure of 9 ton was then gradually applied with the hydraulic press for a period of 5 mins. Upon reaching the 9 tons, the hydraulic was allowed to press the powder for an additional 10 mins to prepare a dense pellet.

7.2.2 Preparation of CdS-Au *via* pulsed laser deposition (PLD)

Deposition of Au nanoclusters on the CdS surface was done by PLD. A laser beam with a power of 31.7 mJ was located outside the vacuum chamber (pumped to a vacuum pressure of about 4.5×10^{-6} mbar) and focused through a quartz glass onto the surface of the Au target at an angle of 45°. The laser beam was focused on the Au target for a period of 90 seconds inside the high vacuum. The laser-to-target incident angle was chosen as such to avoid further interaction of the laser with the generated, outgoing plume. The distance between the Au sample stage and the CdS target was kept at 4.5 cm with the rotating CdS stage kept at room temperature. The pellet was rotated with depositing Au to ensure a uniform distribution of the Au nanoclusters throughout the CdS sample. After this deposition, the CdS pellet was crushed into powder and thoroughly mixed (with a mortar and pestle). Thereafter the powder sample with Au nanoclusters uniformly mixed throughout, was again pressed into a pellet (as before) and more Au nanoclusters were again deposited *via* PLD (with the same parameters as before). This entire procedure was repeated three (3) times to ensure not only a sufficient amount of Au nanoclusters deposited on the CdS NPs but also to ensure their uniformity throughout the powder sample. After every deposition process, the pellet was thoroughly crushed to make CdS-Au nanocomposites (NCs).

7.2.3 Preparation of CdS-Au via sputter coating (SPC)

In this approach, Au nanoclusters were deposited by SPC. This technique is often used in SEM sample coating to avoid sample charging. After evacuating the sputter coater vacuum chamber to a base pressure of 6×10^{-2} mbar, inert argon gas was introduced into the chamber. A high voltage (1.3 kV) applied to an Au target, ionized nearby argon molecules. Once ionized, the Ar^{+} ions accelerated toward the Au target and sputtered Au atoms. Ejected Au atoms (by the ionized argon gas) were then deposited on the CdS surface placed in the path of the resulting plume in a process that lasted for 90 seconds. To ensure uniformity, a tray with the powder was taken out after the 90 seconds and the powder thoroughly mixed. The process was (like before) repeated 3 times.

Characterization techniques

Identification of atomic or molecular ionic species and the distribution of the Au nanoclusters on the CdS NPs surface were studied using ToF-SIMS in negative ion polarity (-SIMS) in both the spectroscopic and imaging mode. ToF-SIMS images were taken of an area of 100×100 μm^2 with an average of 50 scans taken at a rate of 26.21 sec/scan. The structural, absorption, and luminescent properties of CdS-Au NCs were studied using the following characterization techniques: X-ray diffraction (XRD), ultraviolet-visible (UV-Vis), photoluminescence (PL) and Time of flight secondary ion mass spectroscopy (ToF-SIMS). The XRD data were collected over the range of $20° < 2\theta < 60°$ with a *Bruker D8 Advanced* XRD equipped with monochromatic $CuK\alpha$ radiation of $\lambda = 1.54056$ Å. For UV-Vis absorption, the dried powders were dispersed in dimethyl sulphoxide (for a homogeneous solution) before collection of data with *Lambda* 950 UV-Vis spectrometer in the range of 250-700 nm. PL data was collected using a PL system equipped with a 325 nm HeCd laser at room temperature.

7.3 Results and discussion

7.3.1 ToF-SIMS

ToF-SIMS is used to detect the presence of the Au metal on the CdS NP surface and study the stoichiometry. It employs a pulsed ion beam (Bi^{3+}) to remove molecules from the sample surface. The removed molecules are from atomic monolayers on the surface (secondary ions), enabling ToF-SIMS to produce the mass spectrum of elemental and molecular secondary ions present [15]. The mass spectra of CdS-Au NCs was performed in negative mode (using negatively charged primary ions) to collect negative secondary ion spectra. Two operational modes were used in this work, surface spectroscopy and surface imaging of the negative atomic and molecular ions present in the samples.

Surface spectroscopy (negative polarity)

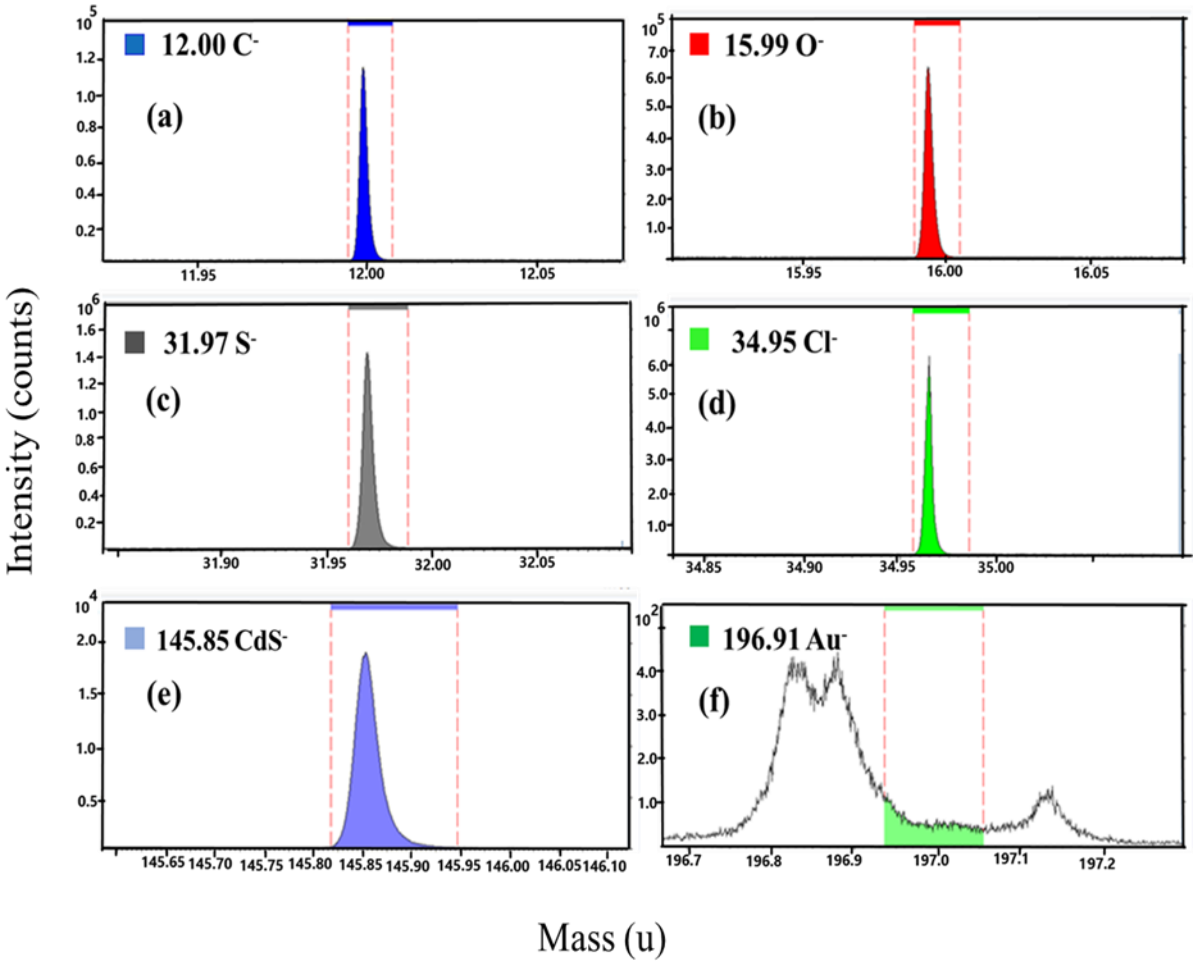

Figure 7.1. The ToF-SIMS negative mode spectra showing the spectrum of (a) C^-, (b) O^-, (c) S^-, (d) Cl^-, (e) CdS^-, (f) Au^- in CdS-Au NCs prepared by PLD technique.

Figures 7.1 and 7.2 (a-f) show the ToF-SIMS negative mode surface spectra for ions and molecules present in the CdS-Au NCs. The negative secondary ions present are C^-, O^-, S^-, Cl^-, CdS^-, and Au^- with atomic mass units of 12.00, 15.99, 31.97, 34.95, 145.85, and 196.91 amu respectively. All the observed species were anticipated from the prepared material.

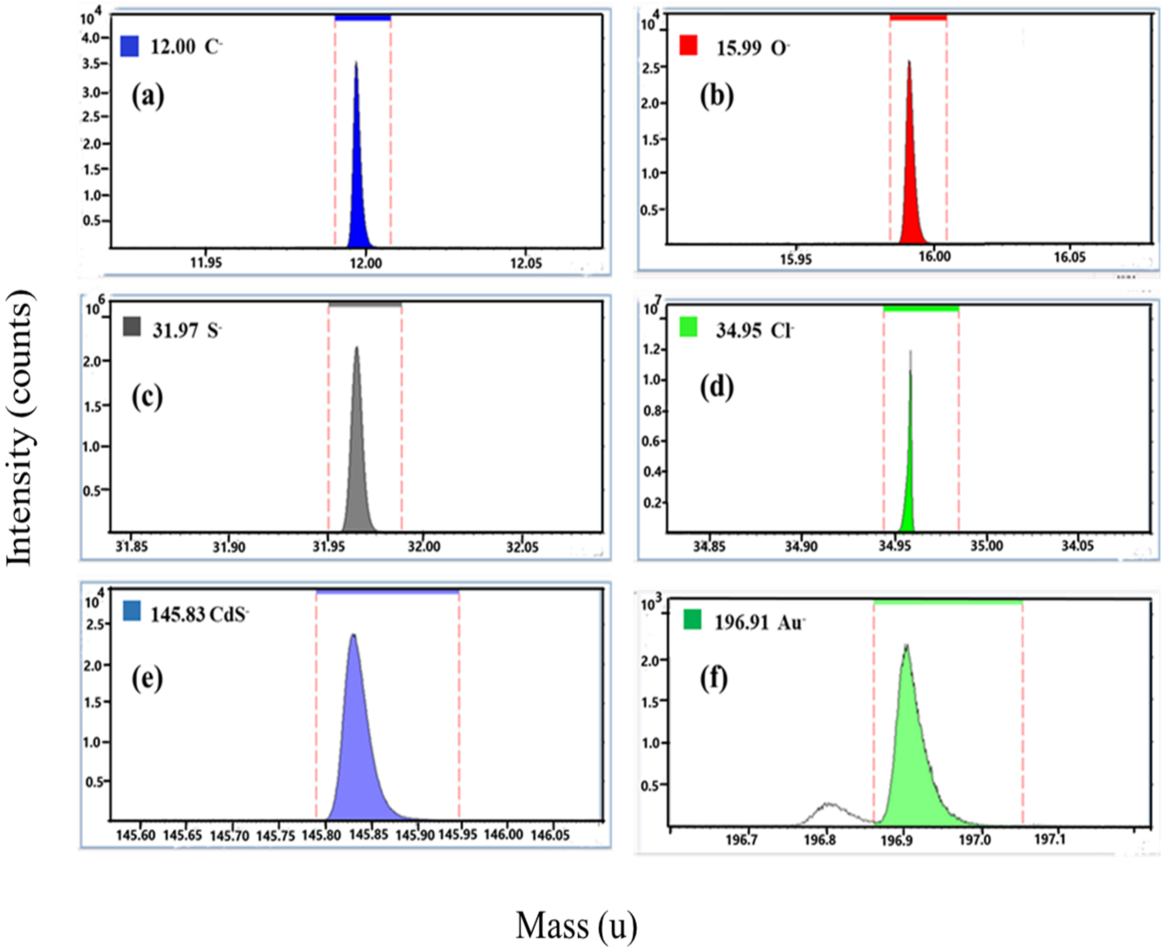

Figure 7.2. The ToF-SIMS negative mode spectra showing the spectrum of (a) C^-, (b) O^-, (c) S^-, (d) Cl^-, (e) CdS^-, (f) Au^- in CdS-Au NCs prepared by SPC technique.

The C^-, O^-, S^- (a-c) originate from TG. However, S^{2-} could be coming from two sources: (i) Na_2S that is used to prepare CdS NPs, and/or (ii) another confirmation of the formation of CdS. The high concentrations of the Cl^- ions (d) is anticipated to be due to the incomplete reaction of the starting material. Figure 7.1 confirms the presence of Au^- in CdS-Au NCs prepared by the PLD technique, however, there is a very low concentration of the metal relative to other species present in the NCs. The SPC NCs prepared over the same amount of time (90 s) of sputtering does however show more concentration of Au metal. Figures 7.1 (f) and 7.2 (f) have different scale bars, indicating that the concentration of Au nanoclusters in SPC is almost 10 times more than in PLD, as such the peak at 196.79-196.90 overshadows the gold peak in PLD making it appear as background noise.

Surface imaging (negative polarity)

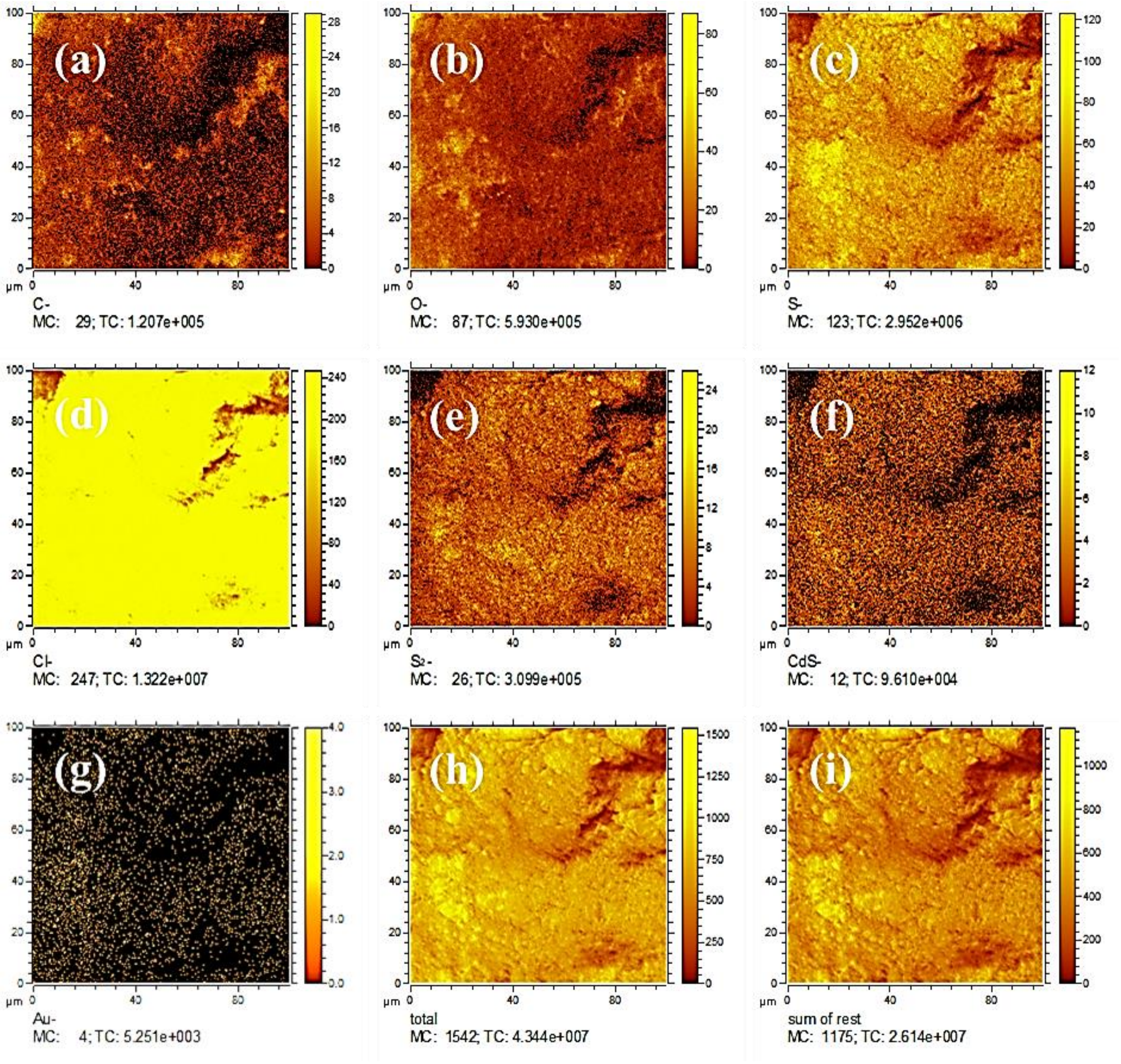

Figure 7.3. The negative TOF-SIMS images of (a) C^-, (b) O^-, (c) S^-, (d) Cl^-, (e) S^{2-}, (f) CdS^-, (g) Au^-, (h) total, and (i) sum of rest for a 100×100 μm^2 area of CdS-Au NCs prepared by PLD technique.

To study how the Au atoms are distributed over the CdS powder, surface maps were generated. Secondary ions surface imaging mode generated maps of the sample by scanning the primary beam over 100×100 μm^2 area and collecting negative secondary ions at each point within the area. Figure 7.3 (a-i) shows negative ToF-SIMS maps of CdS-Au prepared with PLD and Figure 7.4 (a-i) shows images of CdS-Au NCs prepared with SPC. Along the images is a vertical scale bar that represents the signal intensities of each ion. Regions of high ionic concentrations are indicated by high intensities (yellow) while regions with low ionic concentrations of the

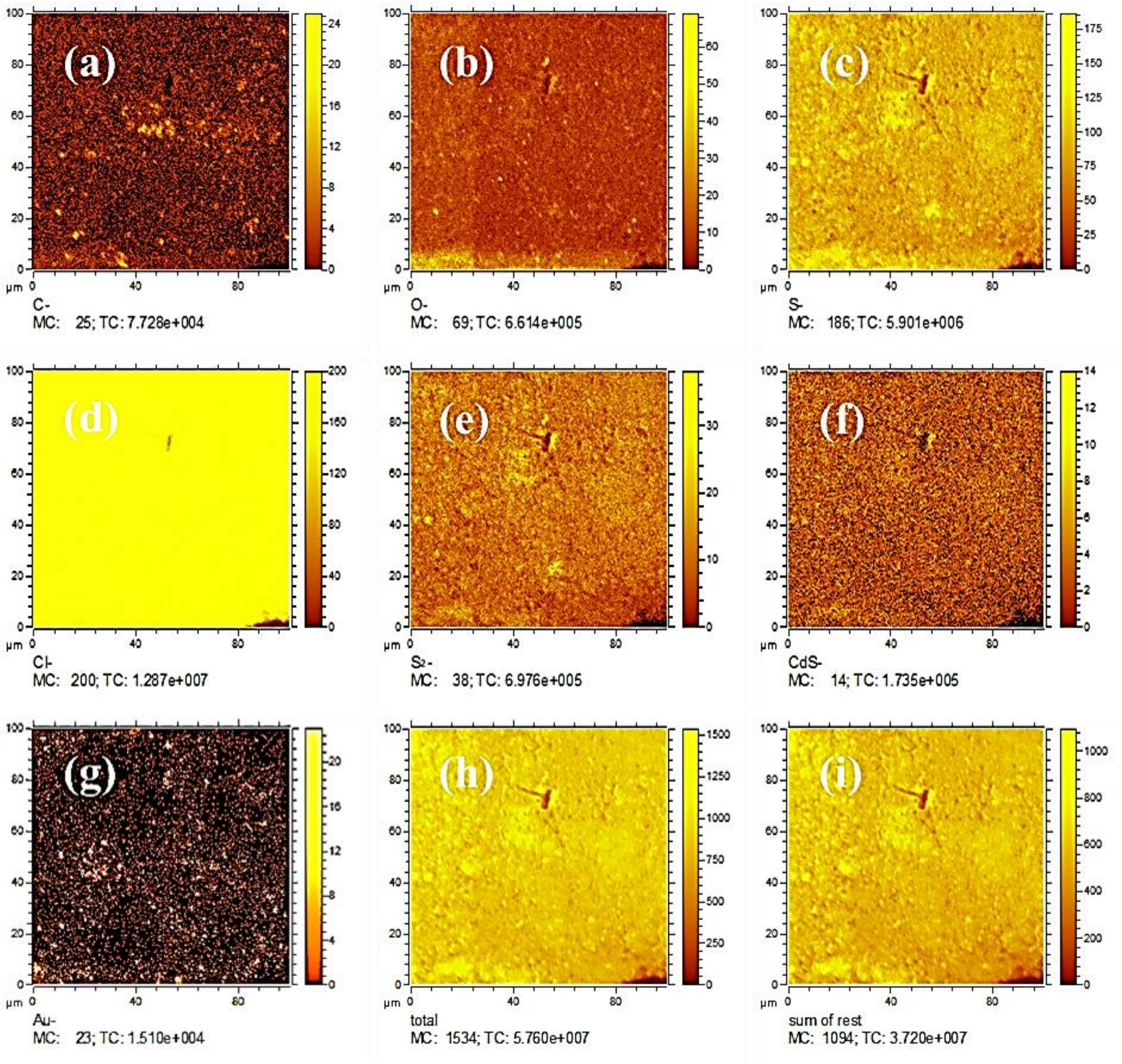

Figure 7.4. The negative ToF-SIMS images of (a) C^-, (b) O^-, (c) S^-, (d) Cl^-, (e) S^{2-}, (f) CdS^-, (g) Au^-, (h) total, and (i) sum of rest for a 100×100 μm^2 area of CdS-Au NCs prepared by SPC technique.

present elements have low intensities (brown). Figure 7.3 (f) and (g) show the ionic concentrations of CdS^- and Au^- respectively. There is a lower concentration of Au in the CdS-Au NCs prepared with PLD with a ratio of Au^-: CdS^- of 1:3. This serves as a confirmation of the presence of Au peak in Figure 7.1 (f). There is a sharp increase in the concentration of Au^- [Figure 7.4 (g)], specifically when compared to CdS^- [Figure 7.4 (f)] in SPC. The ionic concentration ratio of Au^-: CdS^- in SPC goes to 10:7. Again in these maps Cl^- ions have a very high concentration, these are from the Cd^{2+} ($CdCl_2$) source. This is followed by S^- which originates from the capping agent, TG ($C_3H_8O_2S$). S^{2-} has a very low concentration relative to S^-.

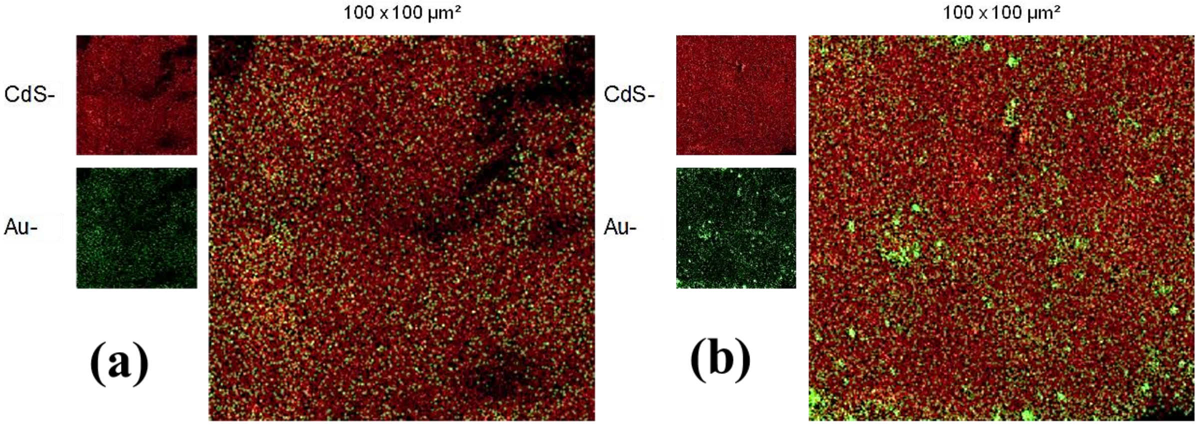

Figure 7.5. The negative overlayer image of CdS^- and Au^- ions showing the distribution of Au in the CdS-Au NCs prepared using (a) PLD, and (b) SPC.

It is therefore evident that the Au metal has been successfully deposited on the CdS semiconductor surface with the two deposition techniques. However, the above ToF-SIMS results show that the quantity of Au metal deposited varies depending on the technique used. SPC produces a high Au concentration while PLD produces a lower concentration. To further investigate the distribution and shape, overlayer images were studied.

Figure 7.5 shows the overlaid images of CdS^- (red) and Au^- (green) for PLD (a) and SPC (b). The images show the distribution of Au on the CdS surface in the negative mode over an area of 100×100 μm^2. Very small evenly distributed Au atoms are observed on the PLD prepared NCs while the SPC sample appears to have agglomerated atoms of Au that appear to be evenly distributed across the area of the sample. Thus, the nucleation and growth processes involved in the two deposition techniques are different. This could be explained in three ways: firstly, for the PLD technique, the powder sample is compressed into a pellet and in the SPC technique Au is deposited on a powder sample. Secondly, SPC has a higher deposition rate between these techniques. In PLD, the forces between the Au atoms and CdS substrate are much stronger than the intermolecular forces of attraction between the Au atoms on the CdS surface. This allows for an even distribution of Au across the CdS NP surface. Furthermore, for SPC there is a high flux of Au atoms arriving in a smaller particle surface the Au atoms are deposited too close and some of them on top of each other. This leads to the migration of atoms to form larger agglomerates with less surface energy. The third factor is the grinding process involved in PLD.

Grinding the pellet could reduce the size of both the CdS NPs and that of the Au metal. Thus, SPC has larger Au agglomerates, while in PLD they are smaller and perfectly circular in shape. The large agglomerates are not all equal size since they are formed by a coalition of smaller Au atoms that were too close to each other. The distance between the Au atoms is likely to also be shorter in SPC.

7.3.2 XRD

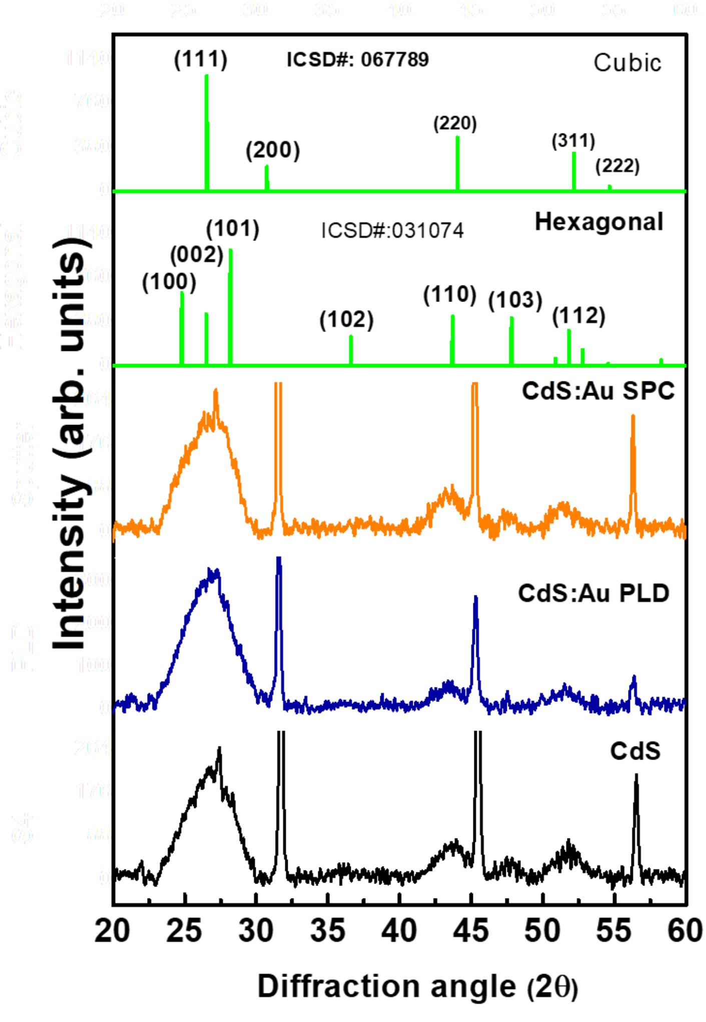

Figure 7.6. The XRD patterns of as-prepared CdS NPs and Au coated NPs with PLD and SPC techniques.

X-ray diffraction was used to study any change in crystal structure of CdS as a consequence of deposition of the Au metal. The diffraction pattern of CdS (Figure 7.6) shows six diffraction peaks at 26.7°, 31.8°, 43.8°, 45.5°, 51.8°, and 56.6° respectively. Three diffraction peaks from these (the most intense); 31.8°,45.5°, and 56.6° are due to the presence of a $Cd(OH)_2$ phase [16], thus indicating an incomplete reaction of the starting material. According to the database of Inorganic Crystal Structure Data [ICSD#: 031074], the CdS NPs have a cubic zinc blend structure from diffraction planes (111), (220), and (311) attributed to 2θ values of 27.4°, 43.8°, and 51.8° respectively. Au QDs have been reported to have diffraction peaks at 36.5°, and 43.9° assigned to diffraction peak indexes from (111), (200) respectively [2]. These peaks are absent in both the PLD and SPC prepared samples.

Table 7.1. Particle size calculation for CdS NPs and CdS-Au NCs prepared with PLD and SPC.

Samples	**Diffraction angle 2θ** (°)	**FWHM** (°)	**D (nm)**
CdS	26.79	3.4877	2.3
CdS-Au (PLD)	26.69	3.8709	2.1
CdS-Au (SPC)	26.70	3.4944	2.3

There is also an unknown sharp peak observed at 27°, which is accompanied by a broad peak at 47° for the as-prepared CdS and SPC samples. Both these peaks are not clearly visible in the PLD sample. Along with this, the intensity of the $Cd(OH)_2$ peaks is decreased which shows the role the technique has played in the crystal structure of the NC. The calculations of crystallite size for the CdS NPs and the CdS-Au NCs were calculated with equation 5.1 and compared in table 7.1.

The table indicates that the CdS crystallite size is not significantly influenced by the deposition of Au metal on the surface. This could mean that the deposited Au metal is very small in size. Therefore, the XRD signal of Au is lost in the background noise. The Au particles are therefore rather nanoclusters consisting of only a few atoms. The crystals of the PLD nanocomposites were slightly reduced in size, and this is likely to be due to the repeated pressing and crushing in the technique. The fact that the structure or size of the semiconductor is not changed indicates that any change that occurs in the nanocomposite properties is not a consequence of the CdS nanoclusters, but rather a result of the combination of both the CdS and Au nanoclusters.

7.3.3 Models of the two deposition technique used to make CdS-Au NCs

Figure 7.7 shows the attachment of Au nanoclusters on the CdS semiconductor surface. PLD has smaller and perfectly spherical nanoclusters that are uniformly distributed across the semiconductor surface. This technique shows a stable thermodynamic configuration, which is important in charge transfer and electronic properties of these NCs. On the other hand, the SPC technique resulted in coalesced nanoclusters. This is a common challenge in the preparation of semiconductor/metal structures.

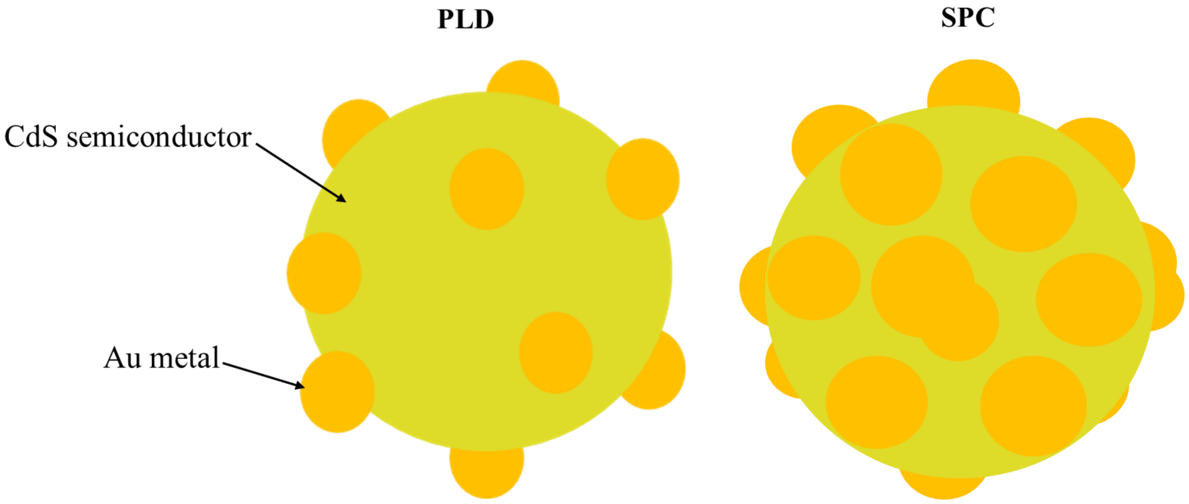

Figure 7.7. Models showing the difference in the CdS-Au NCs prepared using the PLD and SPC techniques.

An electrochemical Ostwald ripening combines multiple metal clusters into a single bigger one and thus taking away the uniformity in these structures [17]. Selective deposition of the Au nanoclusters is also influenced by the crystal morphology and surface capping which provides different chemical reactivities for different facets of the NPs. This can lead to specific growth of the Au nanoclusters on the more reactive part of the CdS material. Habas *et al* [18] reported the selective growth of metal islands on a highly reactive sulfur-rich facet of CdS.

7.3.4 UV-Vis

UV-Vis absorption spectra of the as-prepared CdS NPs, as well as the Au nanoclusters, decorated CdS are shown in Figure 7.8. The NC spectra show combined and synergetic effects of these structures. The absorption ability of the NCs is enhanced depending on the technique used. Coating with the SPC technique shows the highest absorption ability relative to the PLD technique. This relates to the size and shape of the Au nanoclusters. Both these techniques enhanced the absorption abilities of the as-prepared CdS NPs. The absorption intensity enhancement with the presence of the Au nanoclusters has been reported to be as a result of increased scattering from the metal. This allows CdS to absorb more light while injecting more electrons into the semiconductor conduction band [14][19]. Coherent and incoherent interactions on the Schottky junction result in a shift of the exciton transition and therefore a blue shift is observed. The CdS NPs have an absorption edge located at 411 nm, while the PLD and SPC coated CdS-Au nanoclusters have absorption edges at 409 nm and 406 nm respectively.

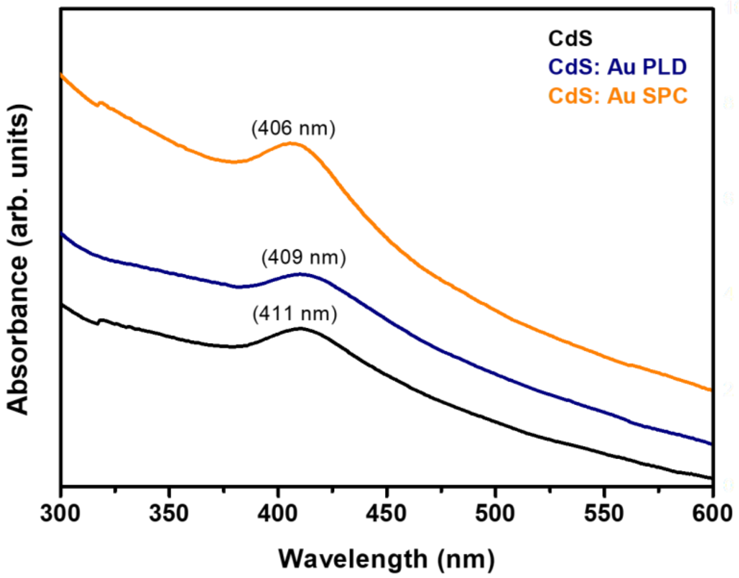

Figure 7.8. UV-Vis absorption spectra of CdS NPs and CdS-Au NCs prepared using PLD and SPC.

Banin *et al.* [7] suggested that the change in optical properties of the NCs could be as a consequence of the formation of new electronic states in the semiconductor-metal interface. These states facilitate the creation of active reaction sites (trapping sites) for photogenerated charges thus promoting charge separation. This is known to play a significant role in increasing the quantum efficiency of semiconductor NPs for water splitting photocatalysts [1].

7.3.5 PL

In Figure 7.9 the PL spectra of pure CdS NPs is compared to the NCs of CdS-Au prepared with the two different techniques. The PL spectrum of the as-prepared CdS NPs has an emission peak at 1.98 eV with a shoulder in the infrared region (from 1.46 eV). CdS-Au PL spectra show a shift of this peak position to higher energies: 2.03 eV and 1.99 eV for PLD and SPC respectively. Luminescence quenching is persistent in this spectra. This is a consequence of the creation of trapping sites created by the Schottky junction between the CdS semiconductor and the Au nanoclusters. The Au nanoclusters serve as electron sinks because of the large work function of Au metal relative to that of CdS NPs [20]. A Schottky junction facilitates the charge transfer from the semiconductor to the noble metal [21][22]. At a lower Fermi level, the Au nanoclusters readily capture the photogenerated electrons from CdS conduction band reducing radiative recombination with holes at the valence band. Ibraham *et al*.[2], reported that CdS-Au has decreased charge recombination with more effective charge separation.

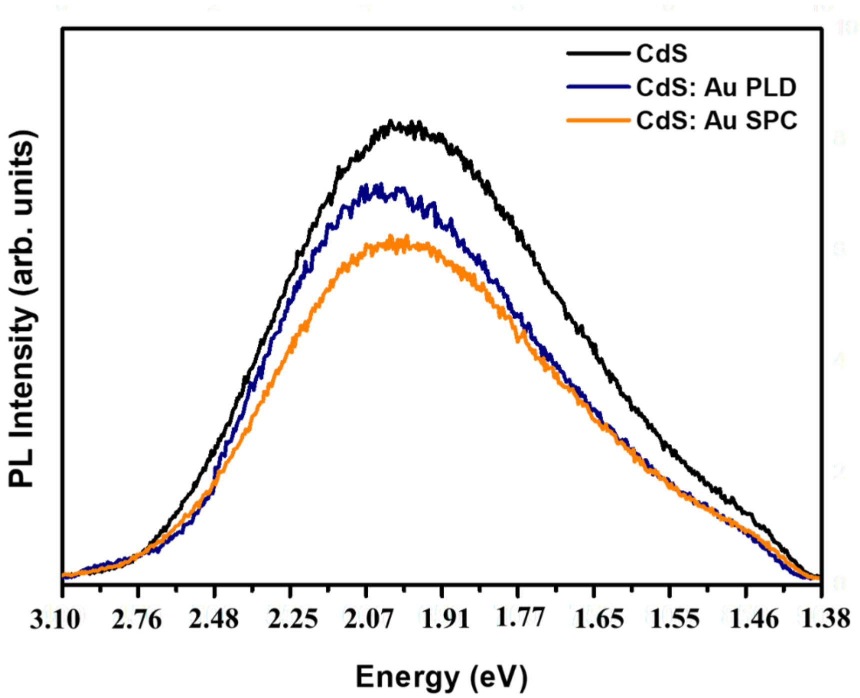

Figure 7.9. The PL spectra of pure CdS NPs are compared to NCs of the CdS-Au prepared with two different physical techniques, PLD and SPC.

The emission in CdS NPs also excites surface plasmons to cause surface plasmon resonance (SPR) of the surface electrons of the Au nanoclusters, which in turn create local electric fields that can modulate the exciton states in the CdS NPs by enhancing the radiative decay rate. Together with the SPR effect occurring in CdS NPs, the Au nanoclusters introduce additional non-radiative electron-hole recombination routes with exciton energy transfer (EET) to the Au nanoclusters from CdS NPs [23]. Consequently, the competition between SPR and EET results in luminescence quenching by hindering recombination of electrons and holes in the semiconductor CdS NPs [24].

The high concentration of Au on the CdS NPs prepared with the SPC technique thus allows for more electrons to be transferred from the semiconductor conduction band to the metal valence band as shown in Figure 7.10. This large transfer of electron is evident in the highly quenched PL for SPC while in PLD there is less quenching. Zhao *et al*.[14], reported that such high efficiency in charge separation results in a fast rise of photocurrent. The design and fabrication of the junction between the light harvesting CdS semiconductor and noble metals are therefore critical in improving photocatalytic activity [4].

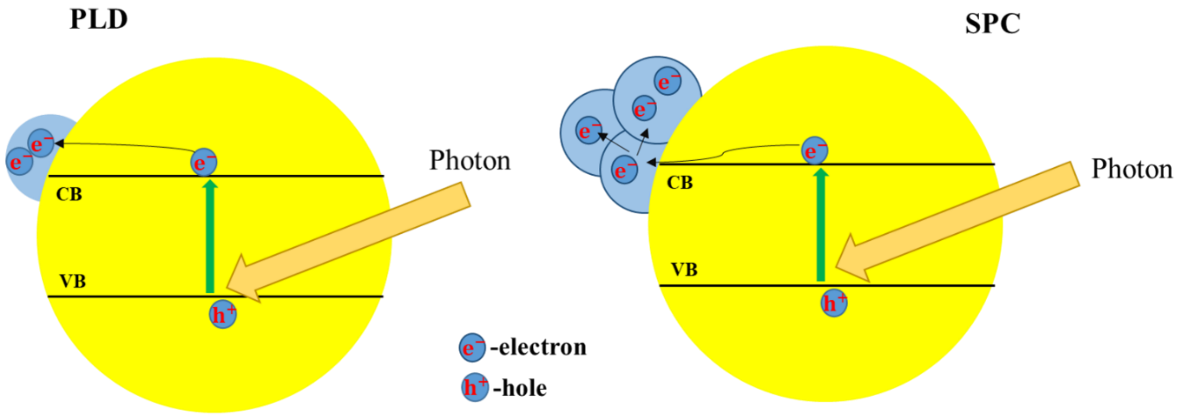

Figure 7.10. Electron transfer diagram of the process that possibly occurs for samples prepared by the two techniques: PLD and SPC.

7.4 Conclusion

In this work, we have presented the influence of two physical techniques in depositing an Au metal on a CdS semiconductor surface. The shape and size of the resultant Au nanoclusters affected the optical, and thus electrical sensitivity of the CdS-Au NC. PLD resulted in very small Au nanoclusters that were uniformly distributed when compared to the SPC technique which has larger nanoclusters. This difference in the nanocluster size and shape enhanced light-induced charge transfer from the CdS conduction band to Au valence band. This electron transfer was due to the successful creation of a Schottky junction. Interactions in this junction were responsible for the blue shift in the absorption edge of these new semiconductor-metal structures. The NCs clearly have new optical properties that were not just the combination of CdS and Au. The deposition method, together with shape and size influenced the optical sensitivity of these nanocomposites.

References

[1] J. Yang, D. Wang, H. Han, and C. Li, “Roles of Cocatalysts in Photocatalysis and Photoelectrocatalysis,” *Acc. Chem. Res.*, vol. 46, no. 8, pp. 1900–1909, 2012.

[2] I. Ibrahim, H. N. Lim, O. K. Abou-Zied, N. M. Huang, P. Estrela, and A. Pandikumar, “Cadmium sulfide nanoparticles decorated with Au quantum dots as ultrasensitive photoelectrochemical sensor for selective detection of copper(II) ions,” *J. Phys. Chem. C*, vol. 120, no. 39, pp. 22202–22214, 2016.

[3] X. Gao, X. Liu1, Z. Zhu, Y. Gao, Q. Wang, F. Zhu, and Z. Xie, “Enhanced visible light photocatalytic performance of CdS sensitized TiO2 nanorod arrays decorated with Au nanoparticles as electron sinks,” *Sci. Rep.*, vol. 7, no. 1, p. 973, 2017.

[4] X. Zong, H. Yan, G. Wu, G. Ma, F. Wen, L. Wang, and C. Li, “Enhancement of photocatalytic H2 evolution on CdS by loading MoS2 as cocatalyst under visible light irradiation,” *J. Am. Chem. Soc.*, vol. 130, no. 23, pp. 7176–7177, 2008.

[5] T. Pons, I.L. Medintz, K.E. Sapsford, S. Higashiya, A.F. Grimes, D.S. English, and H. Mattoussi, “On the quenching of semiconductor quantum dot photoluminescence by proximal gold nanoparticles,” *Nano Lett.*, vol. 7, no. 10, pp. 3157–3164, 2007.

[6] C. S. Transactions, P. R. Reddy, B. Prasanna, and N. Gopikrishna, “Synthesis and Characterization of Nanocrystalline CdS and its Application to Reduction of Nitroarenes,” *Chem. Sci. Trans.*, vol. 5, no. 4, pp. 955–961, 2016.

[7] U. Banin, Y.Ben-Shahar, and K.Vinokurov, “Review pubs.acs.org/cm Hybrid Semiconductor−Metal Nanoparticles: From Architecture to Function,” *Chem. Mater.*, vol. 26, pp. 97–110, 2013.

[8] T. Mokari, E. Rothenberg, I. Popov, R. Costi, and U. Banin, “Selective growth of metal tips onto Semiconductor Quantum Rods and Tetrapods,” vol. 304, no. June, pp. 1787–1791, 2004.

[9] C. O. Sullivan, S. Ahmed, and K. M. Ryan, “Gold tip formation on perpendicularly aligned semiconductor nanorod assemblies,” pp. 5218–5222, 2008.

[10] M. Daniel and D. Astruc, “Sci-Hub | Gold Nanoparticles: Assembly, Supramolecular Chemistry, Quantum-Size-Related Properties, and Applications toward Biology, Catalysis, and Nanotechnology | 10.1021/cr030698+,” 2004.

[11] C. Burda, X. Chen, R. Narayanan, and M. A. El-Sayed, *Chemistry and properties of nanocrystals of different shapes*, vol. 105, no. 4. 2005.

[12] B. Dubertret, M. Calame, and A. J. Libchaber, “Single-mismatch detection using gold-quenched fluorescent oligonucleotid,” *Nat. Biotechnol.*, vol. 19, no. 4, pp. 365–370, 2001.

[13] A. Kudo and Y. Miseki, “Heterogeneous photocatalyst materials for water splitting,” *Chem. Soc. Rev.*, vol. 38, no. 1, pp. 253–278, 2009.

[14] W. W. Zhao, J. Wang, J. J. Xu, and H. Y. Chen, “Energy transfer between CdS quantum dots and Au nanoparticles in photoelectrochemical detection,” *Chem. Commun.*, vol. 47, no. 39, pp. 10990–10992, 2011.

[15] D. W. Mogk, “Time-of-Flight Secondary Ion Mass Spectrometry (ToF-SIMS) Time-of-Flight Secondary Ion Mass Spectrometry (ToF-SIMS) Instrumentation - How,” pp. 1–4, 2017.

[16] P. Chawla, G. Sharma, S. P. Lochab, and N. Singh, “Effect of solvent-induced structural modifications on optical properties of CdS nanoparticles,” *Bull. Mater. Sci*, vol. 33, no. 5, pp. 535–541, 2010.

[17] T. Mokari, C. G. Sztrum, A. Salant, E. Rabani, and U. Banin, “Formation of asymmetric one-sided metal-tipped semiconductor nanocrystal dots and rods,” *Nat. Mater.*, vol. 4, no. 11, pp. 855–863, 2005.

[18] S. E. Habas, P. Yang, and T. Mokari, “Selective Growth of Metal and Binary Metal Tips on CdS Nanorods,” pp. 3294–3295, 2008.

[19] O. Khaselev, O. Khaselev, and J. A. Turner, “A Monolithic Photovoltaic-Photoelectrochemical Device for Hydrogen Production via Water Splitting R EPORTS A Monolithic Photovoltaic-Photoelectrochemical Device for Hydrogen Production via Water Splitting,” vol. 425, no. 1998, pp. 10–13, 2011.

[20] J.C. Revier, "Work Function: Measurements and Results, in *Solid State Surface Science*," vol. 1, M.Green, Editor, New York, 1969.

[21] J. Soc, “Analysis of Work Functions of Noble Metals in Ambient Atmosphere in Commemoration of Journal Award,” vol. 78, no. 1, pp. 16–22, 2015.

[22] S. Gupta, D. Patidar, N. S. Saxena, and K. Sharma, “Electrical study of thin film Al/n-CdS schottky junction,” *Chalcogenide Lett.*, vol. 6, no. 12, pp. 705–713, 2009.

[23] Y. Shan, J. J. Xu, and H. Y. Chen, “Distance-dependent quenching and enhancing of electrochemiluminescence from a CdS:Mn nanocrystal film by Au nanoparticles for highly sensitive detection of DNA,” *Chem. Commun.*, no. 8, pp. 905–907, 2009.

[24] K. Matsuda, Y. Ito, and Y. Kanemitsu, “Photoluminescence enhancement and quenching of single CdSeZnS nanocrystals on metal surfaces dominated by plasmon resonant energy transfer,” *Appl. Phys. Lett.*, vol. 92, no. 21, 2008.

CHAPTER 8

Summary, conclusion, and future work.

8.1 Summary

In *chapter 5* the synthesis of CdS NPs using a chemical precipitation method was discussed and the consequences of using water as a solvent were studied. Quantum confinement effects on the five samples prepared with this method was first observed by the colour change of the powder samples after preparation. In the absence of TG, the powder was orange in colour and turned yellow upon introduction of TG. While increasing its concentration, the yellow colour became weak until it turned whitish-yellow upon adding the highest concentration of TG. This change in colour resulted in a widening of the FWHM in the XRD spectra of the prepared NPs, and it was observed that the particles have a mixed phase of both cubic and hexagonal. It has also been previously reported that these two phases are difficult to separate as their main XRD peaks coincide within 1%. In the same chapter, we also discussed the observed agglomeration of the CdS NPs due to their high surface energies. It was shown that the increase in capping agent concentration led to NP size reduction and this altered the optical properties of the material since the TG molecules acted as a second source of S ions with the ratio of S-to-Cd increasing with increasing TG. Thus the capping agent successfully controlled the size of the NPs, reducing their size into the quantum dot regime. Annealing of one of the samples showed that a phase transformation occurs at about 350 °C. This resulted in sintering of the NPs, which led to an overall increase in the average particle size. These annealed particles also displayed luminescence in the infrared region of the electromagnetic spectrum.

In *chapter 6* we reported on the preparation of the CdS NPs with an ethanol solvent. The influence of the medium was studied to compare with the work done in *chapter 5* where water was used as a solvent. However, in the preparation of these NPs, the starting material was difficult to dissolve in ethanol as was confirmed by X-ray diffraction results. Some starting material still showed peaks with high intensities suggesting only a small concentration of CdS

NPs formed, relative to the starting material. The capping agent (TG) controlled the size of the NPs and again a variation with increasing TG concentration was observed with the NPs crystallizing in the cubic zinc blende phase. A blue shift in the absorption properties was observed and was also indicative of a decrease in particle size. For the CdS NPs prepared in ethanol, luminescence in the infrared region was observed. This luminescence peak was also observed when water was used as solvent, but after annealing.

In *chapter 7* the deposition of the Au nanoclusters on the CdS NP surface, prepared using ethanol as solvent (and where the Au nanoclusters will act as co-catalyst) was discussed. This was done using two different physical techniques: PLD and SPC. The influence of these two techniques on the optical properties of these nanocomposite systems was investigated. It was expected that the presence of the Au metal on the semiconductor, CdS NPs, would lead to the creation of a Schottky junction. The presence of the Schottky junction and its resulting effect was observed in the absorbance and PL spectra. The samples prepared *via* sputter coating showed the highest absorbance indicating a higher rate of transfer of electrons from the CdS surface upon excitation, exists relative to the samples prepared *via* PLD. This resulted in PL quenching as the Au nanoclusters and the resulting Schottky junction prevents recombination of the electrons transferred to the metal with the holes left in the semiconductor. ToF SIMS showed that sputter coating of Au nanoclusters onto the CdS NPs results in more agglomerated Au nanoclusters on the CdS NP surface, while PLD produces uniformly distributed nanoclusters that also have a smaller average particle size.

8.2 Conclusion

In this work, we successfully prepared CdS NPs of varying particle sizes using two different solvents: water and ethanol. The solvent's ability to reduce the surface energy of the NPs allowed crystallization of more stable NPs and these were compared in terms of their agglomeration. The solvent also influenced the dissolution of the starting material thus leading to different optical responses of the two batches of the CdS NPs. Infrared luminescence from the water solvent prepared CdS NPs was achieved by annealing the samples, whereas using ethanol solvent led to the creation of shallow surface defects that were responsible for this luminescence peak.

This work showed the quantum size phenomenon, allowing the ability to tune the semiconductor structural, and optical properties by varying the particle size. CdS NPs showed a change of crystal phase from mixed to cubic zinc blende with size reduction and upon phase transformation temperature the particle size increased resulting in a hexagonal structure. Thus, the variation of particles size showed a blue shift in the absorption spectra with decreasing particle size. The effect of using ethanol as a solvent thus showed the single crystalline phase of cubic zinc blende structure and resulting infrared emission. The ethanol-based NPs were used to deposit Au metal nanoclusters as co-catalyst and a Schottky junction was successfully formed between the CdS and Au using two physical techniques. The junction resulted in electron transfer from CdS to the Au nanoclusters upon excitation, which enhanced the absorption ability of the semiconductor. Electron transfer was accompanied by PL quenching, which occurred as a consequence of reducing electron-hole recombination. The PLD prepared nanocomposites displayed evenly distributed Au nanoclusters on the CdS surface whereas SPC resulted in agglomerated Au nanoclusters, which appeared to give it its superiority in its optical enhancement.

8.3 Future work

In future we hope to answer a question of the role played by the shape and size of co-catalyst nanoclusters on the semiconductor surface. The preparation of nanocomposites is of high importance in science and engineering. These are usually prepared with chemical methods and we would like to eliminate the solvent by using a physical technique like PLD, which is famous for not altering the stoichiometry of materials. We hope to learn to control the size and shape of the metal nanoclusters on the semiconductor surface and study the effect on the optical and electrical properties of the structures.

8.4 Conference presentations

- The 63rd Annual Conference of the South African Institute of Physics, Bloemfontein, 25-29 June 2018. Poster

  Poster title: Quantum confinement effect on structural, morphological and optical studies with temperature effects on TG capped CdS NPs.
- The 1st NANOSMAT-AFRICA CONFERENCE, Cape Town, 19-23 November 2018, Oral presentation

  Presentation topic: Optical sensitivity of CdS-Au nanocomposites prepared by physical techniques: pulsed laser deposition and sputter coating.